Aerodynamic Impact of Leading Edge Surface Treatments on Wind Turbine Blades

Nathan A. Kidder

April 2015

Defense Committee:

Dr. James Gregory, Advisor

Dr. Datta Gaitonde

Department of Mechanical & Aerospace Engineering

Presented in Partial Fulfillment of the Requirements for Graduation with Honors Research Distinction in Aeronautical and Astronautical Engineering at The Ohio State University

Abstract

Wind is becoming an increasingly popular source of energy around the world. More wind turbines are being built, and at larger sizes and higher operating speeds than ever before. The presence of abrasive material in the atmosphere leads to erosion of wind turbine blades which can be detrimental to aerodynamic performance and by extension, power production. The leading edge of turbine blades are especially susceptible to this phenomena. It is therefore desired to be able to apply a protective coating to the leading edge of wind turbine blades to guard against erosion. This project investigated the aerodynamic impact of applying a commercial protective leading edge tape to wind turbine blades. A scaled down 2D airfoil and a full scale commercial turbine tip were used as test articles in this study. Experimental investigation was conducted in the Battelle Subsonic Wind Tunnel at The Ohio State University. Measurements were taken via six-axis load cells, surface pressure taps, and wake surveys. It was determined that at low angles of attack, the detrimental lift and drag impact of the treatment would have a significant aerodynamic performance impact, measuring up to 20% drag increase with as much as a 25% loss of lift. However, that impact subsided at higher angles of attack and in some cases became beneficial to performance in the post stall regime, measuring lift improvements of up to 8% in deep stall. The results indicate that the application of leading edge tape may not have a significant detrimental performance impact in typical operating conditions and may help preserve power production in certain adverse scenarios.

Acknowledgements

I owe a great deal of thanks to Dr. Jim Gregory who provided the opportunity and ongoing guidance to me in completing this work. It was quite a journey and a great experience. I learned more things than I could count in the practice of experimental aerodynamics.

To Mr. Matthew McCrink I have a debt of gratitude. He has served as a critical mentor to my endeavors over the past several years, and there is very little that I could have accomplished without his time and expertise.

I would also like to thank Dr. Robert Siston. His assistance in preparing this thesis has been critical and the professional development gained from his instruction is invaluable.

Thanks to Mr. Matthew Metka who aided me in the setup of load cells and assisted in trouble shooting data acquisition problems.

Finally, and very significantly, I would like to thank Dr. Nathan Webb for helping with the execution of all of these experiments as well as with the setup and data processing for acoustics.

Table of Contents

List of Figures

List of Tables

Nomenclature

Symbols:

b	Span
C_L	Lift Coefficient
C_D	Drag Coefficient
C_M	Moment Coefficient
C_P	Pressure Coefficient
ρ	Density
V	Velocity
R	Specific Gas Constant
P	Pressure
T	Temperature
S	Area
c	Chord
q	Dynamic Pressure

Subscripts

0	Total
s	Static
∞	Freestream

1. Introduction

The use of wind power has been expanding rapidly both in the United States and worldwide. The wind industry in the US has seen an average annual growth of over twenty-five percent for each of the last ten years. [1] The United States has a wind energy capacity of 65.9 gigawatts, now making up over four percent of the approximately 1.2 terawatt capacity of the US power infrastructure. [2] Worldwide, wind energy has a total power capacity of 336 gigawatts making up about four percent of the world's energy production. [3]

Eighty percent of new wind turbines that entered operation in the US in 2014 had a rotor diameter of over one hundred meters. There are now over 48 thousand wind turbines operating in the United States. [1]

Larger sizes and correspondingly higher operating speeds leads to more wear on turbine blades in operation. The high velocity impacts of atmospheric particulate leads to erosion of the blade surfaces, degrading aerodynamic performance of the blades and decreasing power production of the turbines.

In order to fully take advantage of wind energy, protective coatings are needed to protect turbine blades from wear in real world environments. With many protective coatings for wind turbine blades being integrated with the blade itself, it is desirable to have a field serviceable protection that can be easy replaced in the event of wear and damage.

The leading edge of wind turbine blades are especially susceptible to wear. Protective leading edges tapes have been proposed as a solution by several commercial manufacturers as a utility to shield turbine blades. Ideally, use of such protective tapes would allow quick replacements after the device is worn such that the out of operation time for the turbine is minimized.

For any such protective system, it is desired to have minimal aerodynamic impact and noise generation. This research investigated these parameters on two turbine blades; a two-dimensional S809 airfoil, and a commercial full-scale blade's tip section. Each blade was tested for aerodynamic and acoustic impact of a protective tape applied to the leading edge of the blade.

2. Background

2.1 Erosion and Contamination

Erosion throughout the operational lifespan of a wind turbine blade is a prevalent problem. The phenomenon is caused by the collision of airborne environmental particles with the blades, particularly near the leading edge. This results in roughness and pitting on the leading edge as shown in Figure 1.

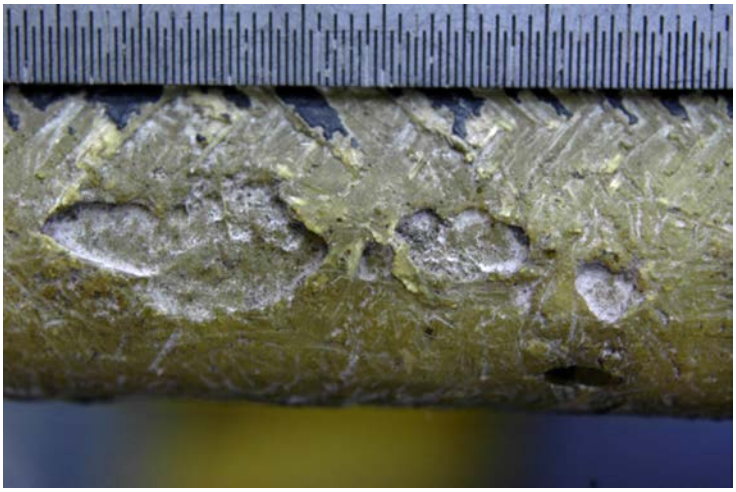

Figure 1: Erosion of Wind Turbine Leading Edge [4]

Eroded blades can have a severe impact on wind turbine performance. For instance, the S809 airfoil was designed to be insensitive to roughness due to its intended application on wind turbine blades. It was additionally intended to maintain the same lift under laminar and turbulent conditions. [5] Despite the S809 being designed for low sensitivity to roughness, numerical studies performed by Gharali and Johnson [4] indicated loss of lift on the order of twenty-five percent for an eroded S809 airfoil under oscillatory freestream conditions.

Studies have shown that leading edge erosion of turbine blades can become a substantial operating issue after only two to three years of operation. [6] [7] This requires that in-service maintenance be performed on the blade throughout the life cycle if turbine blades are to meet their design life which is typically around fifteen years of operation. [8] As turbine rotor diameters increase and tip velocities increase, the impact of airborne particles becomes a

continually more significant problem. Tip speeds exceeding eighty meters per second are common in large wind turbines, as illustrated in Figure 2.

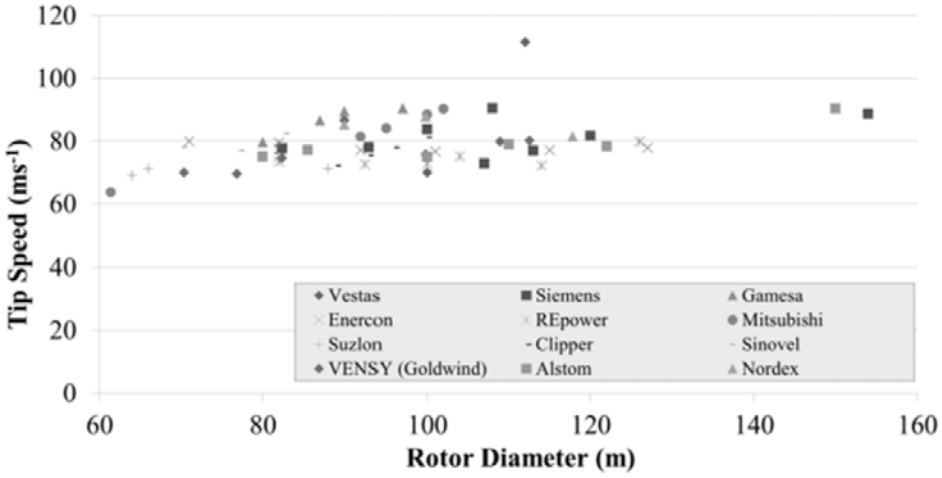

Figure 2: In-Service Blade Tip Speeds [9]

Modern wind turbine blades are typically constructed from composite materials. The ability to design the implementation of such materials for very specific loading conditions provides a strong advantage for their use. However, they also perform poorly under transverse impacts and are sensitive to environmental factors such as heat and moisture. [9] As such, much effort has been invested in creating effective protective coatings. The objective of the coatings is either to protect the material properties of the blade from static environmental conditions or to protect the structure from impact. [9]

Erosion on blades can be caused by particle or moisture droplet carrying winds. The primary causes of leading edge erosion are rain, hail, sea spray, dust, sand, and wildlife. [9] Even in regions with relatively dry climates, erosion caused by moisture has still been found to be a substantial issue. [10]

Sareen et al [11] conducted an experimental investigation on the aerodynamic performance impact of leading edge erosion. The results showed a drag increase of 6 to 500 percent due to varying levels of erosion at Reynolds numbers from 1 to 1.85 million. The analysis predicted that an eighty percent increase in drag would lead to a five percent loss in power production for the wind turbine. The eighty percent drag increase was the result of relatively low erosion. More

substantial drag increases from moderate to heavy erosion could lead to energy production losses on the order of twenty-five percent.

In addition to concern for the aerodynamic impact of erosion, structural impact to the blade is also of significant concern. Through-thickness erosion of the leading edge would lead to ingestion of particulate, including water, to the internal blade structure which could have a detrimental impact to the turbine over extended periods of time. [9]

Gaudern [12] compared the effects of erosion to those of a boundary trip at five percent chord using a zig-zag turbulator. Tripping the flow at the leading edge of a blade resulted in similar aerodynamic performance impacts to low erosion effects. Moderate to severe erosion decreased performance further than the leading edge trip.

In addition to erosion, aerodynamic performance of turbine blades can also be damaged by the accumulation of surface contaminants. Most commonly, ice and insect matter colliding with the blade may build up and increase the roughness of the blade.

It well known that roughness on a surface of an airfoil generally leads to an increase in drag. Kim et al [13] determined that roughness at the leading edge produced a higher momentum deficit than roughness at other locations, establishing the criticality of a clean leading edge.

Power production of wind turbines operating in high winds has been known to drop without apparent reason. Investigations by Corten and Veldkamp [14] have suggested these occurrences are due to insect contamination.

Low levels of insect contamination can decrease turbine power by eight percent while high levels of contamination may decrease power production by over fifty percent. [15] The simplest solution to insect contamination is by application of non-stick coatings near the leading edge that provide a smooth, low-friction surface which deters adhesion. [15]

2.2 Protective Coatings

Leading edge tapes that can be replaced when worn have been proposed as a solution to the erosion problem. [15] Highly elastic materials, such as polyurethane, have been shown to effectively absorb the energy of particle impacts in both wind turbine [16] and helicopter rotor [17] applications.

The application of a leading edge tape changes the early development of the boundary layer due to the backward facing step at the end of the tape. This step results in a small region of separation which causes an increase in momentum thickness which contributes additional drag. Leading edge tape often causes transition to occur earlier if the flow was initially laminar. [18]

Chinmay [19] performed a study on the impact of leading edge tapes which predicted a five to fifteen percent drag increase on turbine blades. Chinmay declared that this would not result in a measurable difference in overall energy production, although he noted that the increased drag may manifest problems in other areas of operation.

3M conducted a study [20] of erosion effects on power output for cases of a turbine protected by a 3M protective tape product, unprotected with moderate erosion, and unprotected with severe erosion. The study was based upon the experimentally measured aerodynamic impact of erosion and extrapolated to a 1.5 megawatt rated turbine with a capacity factor of thirty percent. The study predicted marginally higher energy production by the unprotected turbine in the first year. However, following the first year the unprotected power production begins to wave due to erosion. In the fourth and fifth years of operation, the unprotected turbine was suspected to have pits and gouges on the leading edge resulting in a five percent loss in annual energy production. In a worst case scenario of gouging and delamination, a relative energy loss on the order of fifteen percent was predicted. The results of the study were summarized below in Figure 3.

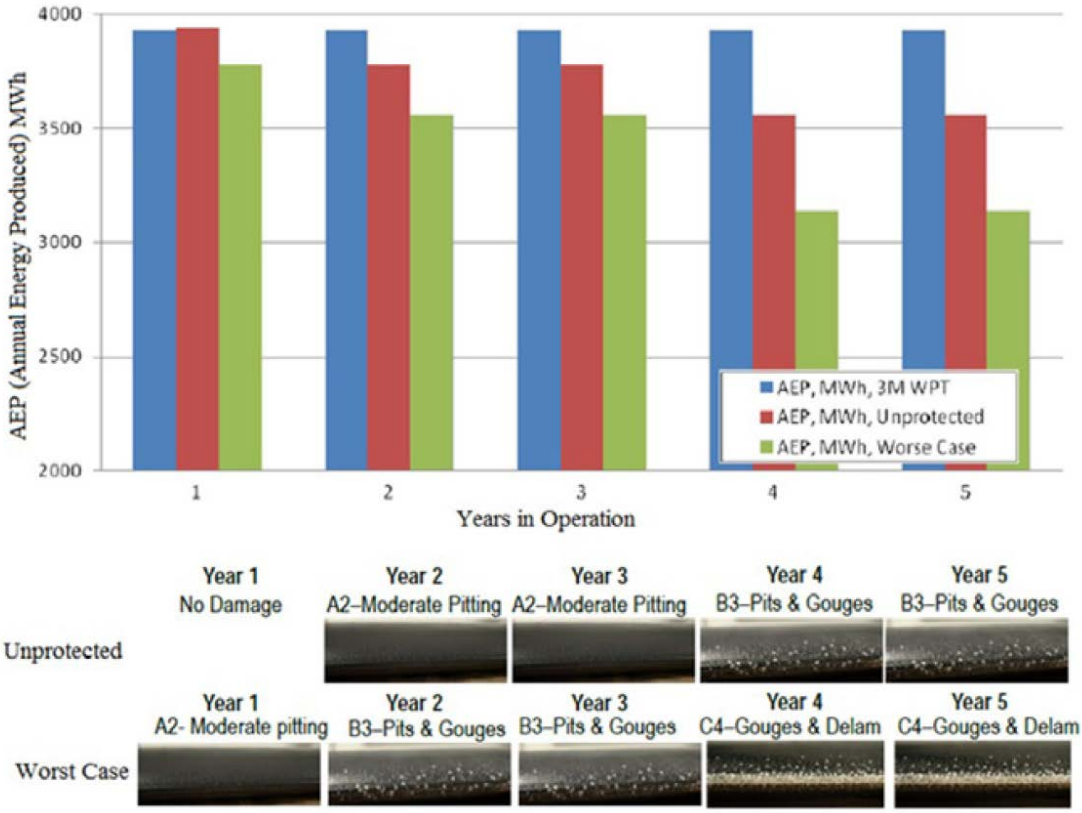

Figure 3: Erosion Effect on Energy Production [20]

Giguere [18] tested the aerodynamic impact of leading edge tape on five different wind turbine airfoils. It was determined that extending the tape beyond five percent chord and staggering the tape in multiple layers was most beneficial for minimizing loss of aerodynamic performance.

Leading edge tape also provides a slick surface which reduces the accumulation of insect debris and other contaminants, further preserving aerodynamic performance of the blades. [18]

3. Experimental Setup

3.1 Test Articles and Treatments

Testing of the effect of protective tape application on wind turbine blade leading edges was performed using two blade models. The first component of the study was performed on a full scale commercial wind turbine tip section with a thickness of 17%. The root chord of the section was 38.5 inches which tapered to a tip chord of six inches. The length of the section was 35 inches. The approximate geometry of the tip planform is included below in Figure 4 for reference. The geometry is approximate for visualization purposes only as the exact model dimensions are proprietary. A steel mounting rod extended from the quarter-chord position of the root chord.

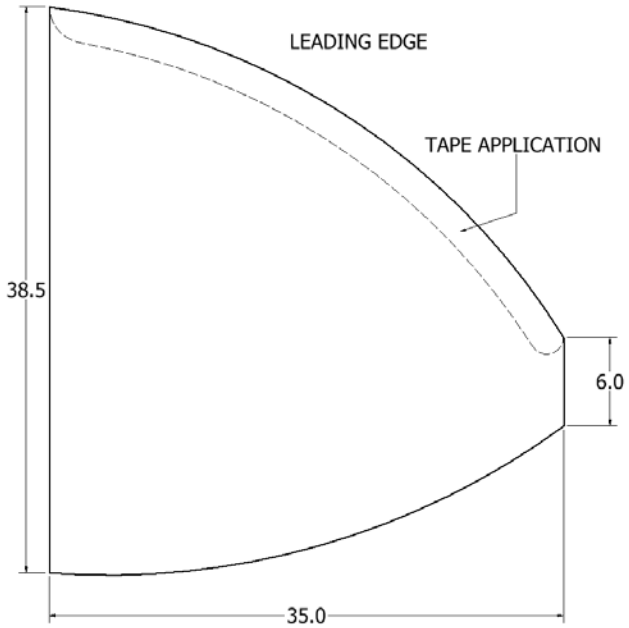

Figure 4: Tip Section Geometry

An experimental protective tape product, provided by a commercial supplier, was applied to the leading edge of the tip and tested to determine the aerodynamic performance impact.

In addition to the full scale tip, testing was also performed on an S809 airfoil. The chord of the airfoil was eighteen inches. The profile of the S809 airfoil is shown below as Figure 5.

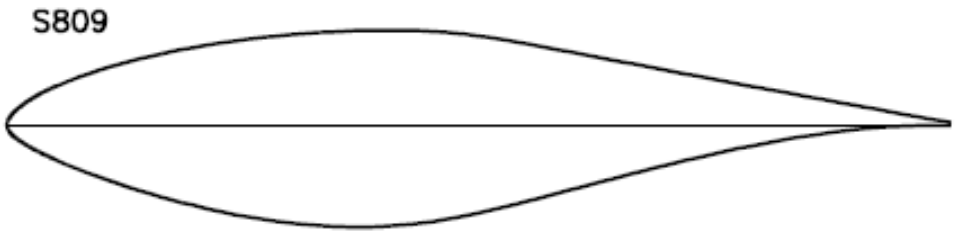

Figure 5: S809 Airfoil Section [21]

The S809 airfoil was built by a composite fiberglass skin placed over a series of ribs. A steel tube ran through the vertical center of the airfoil at the quarter-station. The airfoil included sixty surface pressure taps.

The S809 airfoil was approximately quarter scale compared to the size of the tip section. The commercial treatment product would have been significantly disproportional to this airfoil. The product was therefore simulated in application to the S809 by constructing a scale model from blue painter's tape. Painter's tape was chosen for its smooth texture, and relative comparability in roughness to the commercial product.

3.2 Wind Tunnel Facility

Testing was conducted at The Ohio State University's Aerospace Research Center in the Battelle Subsonic Wind Tunnel. The wind tunnel is an open return tunnel that circulates air from outside the building. The test section is 39 inches tall, 55 inches wide and 96 inches long. The tunnel is powered by an 8 foot diameter six-bladed fan belt driven by a 125 horsepower 3-phase AC motor connected to a variable frequency motor controller. The maximum speed is 45 meters per seconds which gives a maximum Reynolds number of 920,000 per foot.

The turbulence intensity was measured as 0.55 percent at the center of the test section with quiescent conditions at the inlet. Additional low frequency turbulence is expected due to the presence of environmental wind at the tunnel inlet and outlet.

The airspeed is determined by a total pressure measurement through a static pressure ring in the plenum prior to the contraction section of the tunnel and static pressure measurement through a static pressure ring immediately prior to the test section.

Since air is ingested from the external environment, the air properties are determined by data from Ohio State's Don Scott Airport which is located immediately adjacent to the test facility.

3.3 Load Cell Measurements

ATI Theta US-600-3600 six-axis load cells were used for direct measurement of the lift, drag, and pitching moment on the test articles. Verification of the load cell readings were performed prior to each test series by placing a precisely known weight on the test article and checking for a matching reading in force and moment from each load cell. An illustration of the load cell is shown in Figure 6.

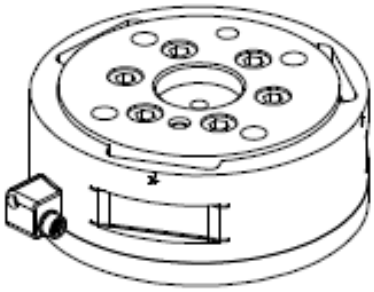

Figure 6: ATI Load Cell [22]

For the tip section, a single load cell was mounted to one outside tunnel wall. The steel support rod of the tip was attached to the load cell, mounting the section horizontally in the tunnel. The horizontal dimension of the tunnel is 55 inches. This orientation was intended to provide sufficient room for the development of the tip vortex without interfering with the tunnel walls.

A one inch gap was left between the base of the tip and tunnel wall. Since the rod undertook substantial deflection when testing at high speeds, the gap prevented contamination of the force measurements from binding between the test article and the tunnel wall. The mounting setup of the load cell required that the lifting direction of the article be down.

The S809 airfoil was arranged vertically in the wind tunnel. The steel support rod was fastened to a load cell at both the top and bottom of the tunnel. A half inch gap was left both above and below the airfoil in order to prevent binding to the tunnel walls. The wind tunnel is suction driven, resulting in lower internal static pressure than in the laboratory. The pressure difference

results in finite contraction of the walls, such that the clearance was less than half an inch in actual operation.

3.4 Surface Pressure Measurements

The S809 airfoil included sixty surface pressure taps. Measurements were taken from 33 of these taps due to transducer capacity limitations in the test facility. The layout of the pressure taps are illustrated below in Figure 7.

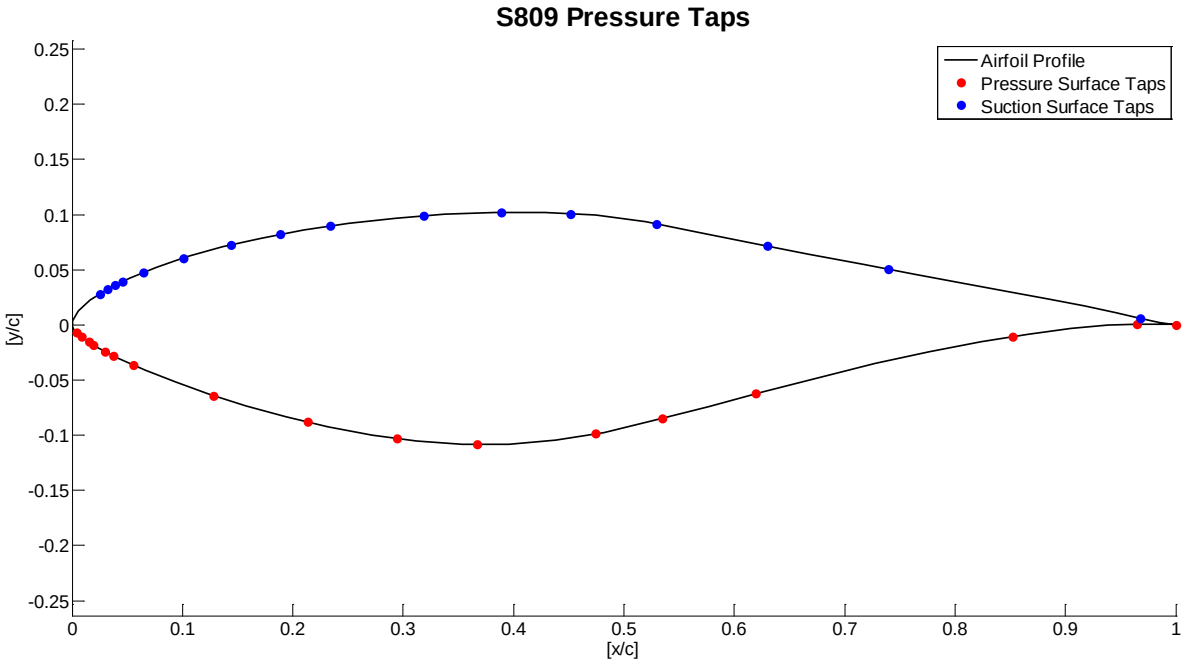

Figure 7: Pressure Tap Layout

The locations of the pressure tabs were tabulated below in Table 1. Channels 1-16 were on the pressure surface of the airfoil and channels 17-33 were on the suction surface.

Table 1: Static Pressure Tap Locations

Channel	Location [x/c]	Location [y/c]
1	1.0000	0.0000
2	0.9652	0.0007
3	0.8522	-0.0105
4	0.6196	-0.0624
5	0.5346	-0.0848
6	0.4743	-0.0986
7	0.3672	-0.1081
8	0.2945	-0.1030
9	0.2136	-0.0882
10	0.1284	-0.0644
11	0.0556	-0.0362
12	0.0375	-0.0278
13	0.0302	-0.0240
14	0.0154	-0.0154
15	0.0087	-0.0109
16	0.0045	-0.0072
17	0.0195	-0.0180
18	0.0252	0.0279
19	0.0318	0.0322
20	0.0389	0.0358
21	0.0455	0.0392
22	0.0646	0.0476
23	0.1011	0.0606
24	0.1437	0.0723
25	0.1889	0.0820
26	0.2342	0.0895
27	0.3189	0.0987
28	0.3886	0.1018
29	0.4516	0.1006
30	0.5294	0.0914
31	0.6301	0.0717
32	0.7398	0.0504
33	0.9675	0.0060

It should be noted that there were not static pressure ports used in the immediate vicinity of the leading edge of the airfoil due to the presence of the protective tape in the application testing. However, the impact of this data loss was anticipated to be minor due to the small magnitude of the suction peak on the S809 airfoil. [5] This is further discussed in Section 4.2.

The tip section test article was not tapped for surface pressure measurements.

3.5 Pressure Wake Measurements

The total pressure in the wake of the S809 airfoil was measured by a pitot probe mounted 12.5 inches, or a nondimensional distance of 0.69 by chord length, behind the trailing edge of the airfoil. A single axis traverse moved the probe across the horizontal centerline of the tunnel for the measurements. Wake profiles were not obtained for the tip section since its size required it to be mounted horizontally in the tunnel.

The traverse moved the pitot probe through the wake at a constant velocity of 0.119 inches per second while samples were collected from the transducer at a rate of one hertz. This corresponds to 151 samples per chord length of distance.

3.6 Acoustic Measurements

Acoustic measurements were collected via microphones at four locations for each test article. For the S809 airfoil, each microphone was pointed directly at the airfoil. The airfoil was mounted via a steel rod which ran through the quarter chord. Two microphones were located at 58% chord and the other two were placed 2.17 chord lengths downstream of the leading edge. One microphone at each streamwise location was positioned one chord length above the location of the support rod and one microphone was one chord length below. The microphone layout was illustrated in Figure 8.

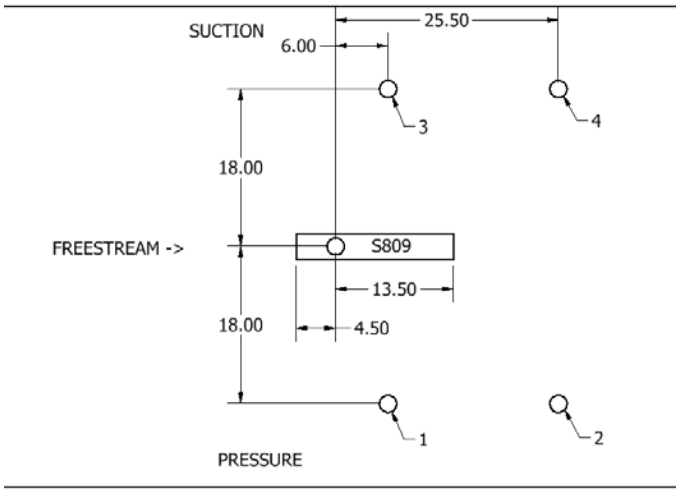

Figure 8: S809 Microphone Layout

The general layout of the microphones for the tip section was similar. Relative to the tip section, two microphones were located inline streamwise with the quarter-chord mount point and two were located 29 inches downstream. At each streamwise station one microphone was located 12.5 inches above the pivot point and one 12.5 inches below. The microphone layout for the tip section was illustrated below in Figure 9.

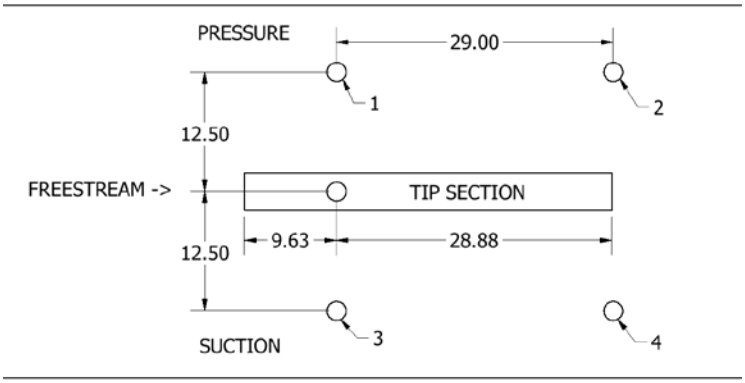

Figure 9: Tip Section Microphone Layout

In both configurations, the microphones were assigned identifiers one through four, defined per location relative to each test article. The numbering scheme for the microphones is shown in Table 2.

Table 2: Microphone Identifiers

Mic	Description
1	Upstream Pressure Side
2	Downstream Pressure Side
3	Upstream Suction Side
4	Downstream Suction Side

3.7 Data Acquisition

The force measurements acquired by the ATI-Theta load cells were read as a series of analog voltage signals. These signals were digitally acquired by a National Instruments USB-6343 which converted the voltages to sixteen bit digital encoding. The values were read into a LabVIEW virtual instrument. The signals for each axis of the load cells were coupled, requiring that the measurements be converted via a manufacturer's calibration matrix in order to extract

useful force values. The load cell measurements were sampled at a rate of 20 hertz and filtered through a running average of four samples. During each test, load cell data was collected continuously for thirty seconds.

The wind tunnel total and static pressures were also acquired in the virtual instrument. These readings were used in order to calculate the dynamic pressure, and by extension the wind tunnel velocity, shown in the equation below for incompressible flow.

$$V = \sqrt{\frac{2(P_0 - P_s)}{\rho}} \tag{1}$$

The density was determined by an automated fetching routine which obtained the outside air pressure and temperature from the weather station located adjacent to the laboratory. The density was then calculated by application of the ideal gas law.

$$\rho = \frac{P}{RT} \tag{2}$$

Pressure readings were taken by Scanivalve DSA-3017 16-channel pressure transducers. The transducers digitally report absolute pressure readings via a TCP/IP network interface. The transducers were connected to the data acquisition PC by a local area network supported by a Cisco SLM2005 network switch. The pressure readings were obtained and recorded by a MATLAB interface.

4. Results

4.1 Data Reduction and Processing

For each test, four runs were performed during which load cell data was collected. Data was taken continuously for approximately thirty seconds during each run. The data from each run was analyzed and averaged in order to obtain a reduced set of key parameters for the run.

The lift coefficient was utilized as a nondimensional measure of the test article's lifting capability. The lift coefficient is defined by the quotient of lift force and the product of dynamic pressure and a reference area, as shown in the equation below.

$$C_L = \frac{L}{\frac{1}{2}\rho V_\infty^2 S} \tag{3}$$

The measured drag force was similarly nondimensionalized to drag coefficients. The coefficients were determined by calculation with the instantaneously measured force and instantaneously measured freestream velocity. The density and reference area were considered constants.

$$C_D = \frac{D}{\frac{1}{2}\rho V_\infty^2 S} \tag{4}$$

The pitching moment, measured from the quarter-chord location, was also converted to coefficient form. In this case, the addition of a length scale with the area was required in order to fully nondimensionalize the value, shown below.

$$C_M = \frac{M}{\frac{1}{2}\rho V_\infty^2 S c} \tag{5}$$

The assigned reference area was the planform area of each test article and the reference length was the mean chord. For the S809 airfoils these corresponded to values of 4.875 square feet and 18 inches respectively. Due to the proprietary nature of the tip section, the reference area and length were left undefined and forces were reported as the product of the force coefficient and the reference area, therefore having units of area. Similarly, for the tip section, the moment was report as the product of the moment coefficient, reference area, and reference length, therefore

having units of length cubed. The focus of investigation was on relative change between treated and untreated cases, under which the remaining units drop out.

For each conducted test, the load cell data was processed as visualized in plots of individual sample points. This allowed for visual identification of abnormalities in the data sets. In addition to the physical force measurements, the nondimensional coefficients were also plotted along with the measured tunnel velocity. The physical measurements were expected to respond strongly to fluctuation of the freestream velocity due to the square velocity dependence of dynamic pressure. However, the coefficients were expected to stay approximately constant due to the relatively weaker dependence of the coefficients on Reynolds numbers. These expectations were assessed and met by the data visualization methods. A sample visualized data set for the S809 airfoil is included below as Figure 10.

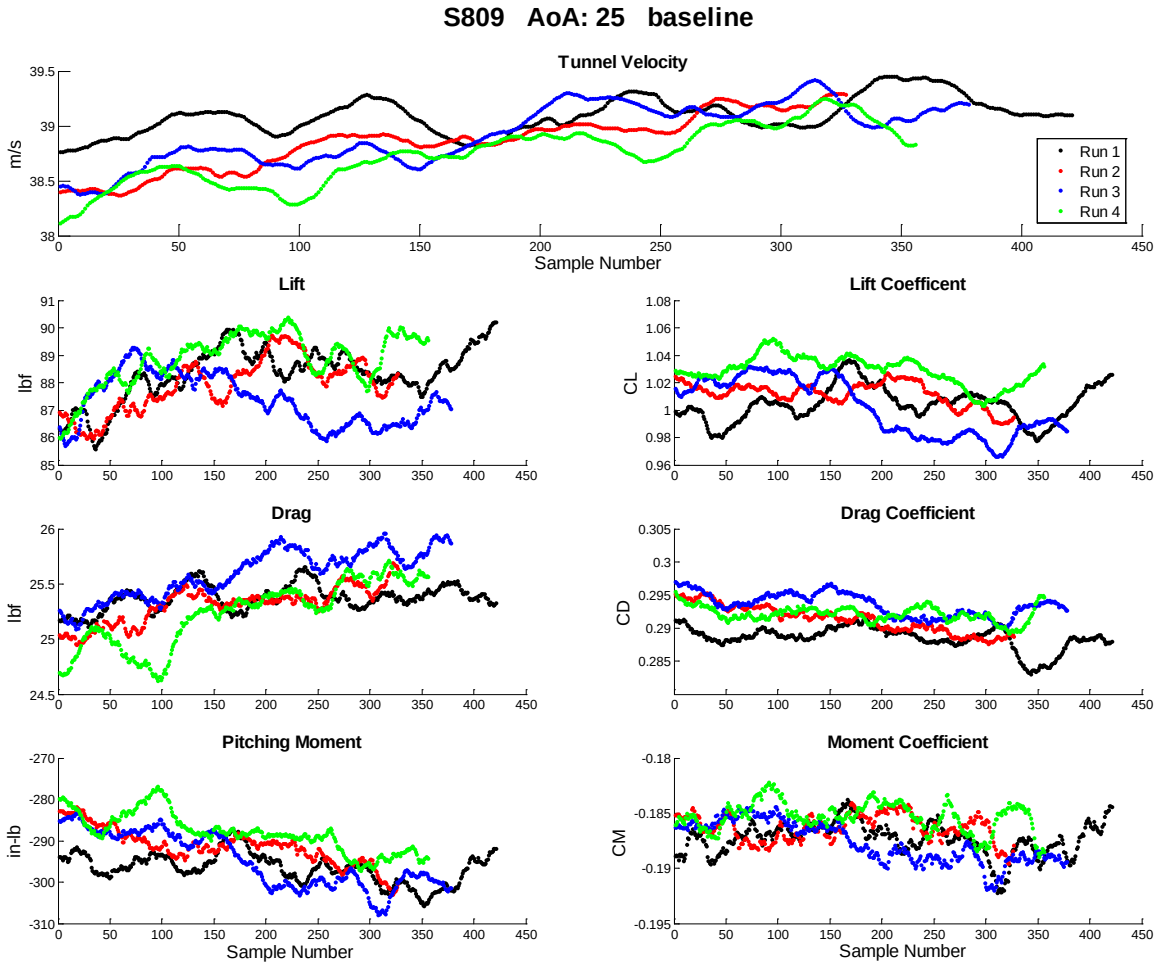

Figure 10: Raw Data Sample

In each of the four test runs visualized above, the tunnel speed had a slight increase during the test. Per the discussion above, the physical force measurements increased in magnitude as expected. Additionally, the coefficients maintained near constant value throughout the velocity fluctuation, validating the use of instantaneous force measurements in conjunction with the instantaneous velocity sampling. The data samples from each test conducted in this study were included in Appendix B.

For each run, the measured force coefficients were averaged across the samples in order to obtain a single value. Since each test included four runs, four data points were determined from each test condition. After each run, the wind tunnel was fully shutdown and the instrumentation was re-zeroed prior to the start of the next.

At each test condition, static pressure data was collected for three runs. The measured surface pressures were nondimensionalized into pressure coefficients, the quotient of pressure difference from freestream at the tap and freestream dynamic pressure, by the equation below.

$$C_P = \frac{P - P_\infty}{\frac{1}{2}\rho V_\infty^2} \tag{6}$$

The pressure transducers acquired gauge pressure readings, calibrated to the atmospheric pressure at the time of the experiment. Therefore, the atmospheric pressure was added to the measured values prior to subtracting the freestream pressure in order to calculate the pressure coefficients.

The lift on a surface can be obtained by integrating the pressure distribution around the object. Over an airfoil, the pressure distribution is assumed to be constant along the span, resulting in the equation below.

$$L = \oiint_S P\, dA = b \oint_\xi P\, d\xi \tag{7}$$

Where xi is representative of the contour defined by the profile of the airfoil.
Nondimensionalizing, discretizing into series for upper and lower sets of pressure taps, and accounting for conversion for the airfoil frame to the lab frame results in the final equation below for determining the lift coefficient from static pressure distribution.

$$C_L = \int_0^1 \left(C_{P_{upper}} - C_{P_{lower}}\right) d(^x/_c)\ \cos\alpha \tag{8}$$

Prior to determination of the lift coefficients, the static pressure data was post processed using an interpolation routine. A cubic spline technique was used to interpolate values such that one thousand discrete data points where defined for both the top and bottom surfaces of the airfoil. The integration was then performed using a trapezoidal summation technique.

Total pressure was measured in the wake behind the airfoil. By the Bernouli principle, the total pressure can be expressed as the sum of the static and dynamic pressures, shown in the equation below.

$$P_0 = P_s + q = P_s + \frac{1}{2}\rho V^2 \tag{9}$$

Rearranging allows the velocity to be determined from the total pressure reading as shown below.

$$V = \sqrt{\frac{2(P_0 - P_s)}{\rho}} \tag{10}$$

It should be again noted that the pressure transducers used in the experiments read gauge pressure, referenced to ambient atmospheric conditions, therefore the atmospheric pressure was added to the measured reading in order to obtain absolute total pressure. The static pressure in the tunnel was obtained also by the Bernoulli principle, using the known total pressure and tunnel velocity.

The wake measurement then allows for the determination of drag force based upon the momentum deficit of the wake. Under the assumptions of steady-state incompressible flow with constant spanwise properties, the drag can be expressed easily from conversation of momentum applied to a control volume surrounding the airfoil. This is mathematically represented by the equation below.

$$D = \rho h \int_1^2 V(V_\infty - V)\, dx \tag{11}$$

Where ‘h’ is the length measurement of the out of plane dimension, corresponding to the span of the airfoil under the given test conditions. Using the definition of the drag coefficient from

Equation (4), the drag coefficient can be determined directly from the momentum deficit by the equation below.

$$C_D = \frac{2h}{V_\infty^2 S}\int_1^2 (V \cdot V_\infty - V^2)\, dx \tag{12}$$

In order to reduce the noise in the data sets obtained by the wake traverse, the data was post processed using an averaging method where new data points where defined by a five point average, where the current data point was averaged with the two points ahead and behind it.

In order to obtain drag coefficients, the post processed data set was numerically integrated using a trapezoidal summation method.

4.2 Baseline and Verification

Testing of the S809 was conducted at a tunnel velocity of forty meters per second, corresponding to a Reynolds number of approximately 1.2 million. Four angles of attack were tested. Zero degrees, twelve degrees for near stall conditions, fifteen degrees for stall, and twenty-five degrees for deep stall conditions. Force measurements were taken via load cells and pressure measurements were obtained via the surface taps and wake traverse. Surface tap data was processed to obtain lift values and wake traverse data was processed to obtain drag values. The load cells and pressure transducers were zeroed prior to each run. Load cell data was taken for four runs, acoustic measurements were taken on the first, static pressure measurements on the first three, and wake measurements on the fourth. The aerodynamic coefficients determined from the post processed data were summarized in Table 3. The determined values for each individual run were placed in Appendix B: Additional Tables.

Table 3: S809 Baseline Results

AoA	C_L (Load)	C_L (Pressure)	C_D (Load)	C_D (Pressure)	C_M (Load)
0°	0.103	0.328	0.019	0.019	-0.034
12°	1.204	1.211	0.091	0.056	-0.068
15°	1.261	1.228	0.048	0.147	-0.079
25°	1.012	1.186	0.291	N/A	-0.187

The S809 airfoil was designed to have a limited suction peak at the leading edge of the airfoil as a deterrent to transition. [5] The measured pressure results exhibited this in the nearly constant pressure distribution near the leading edge of the suction surface. These results are illustrated below in Figure 11 with the results from all three runs overlaid.

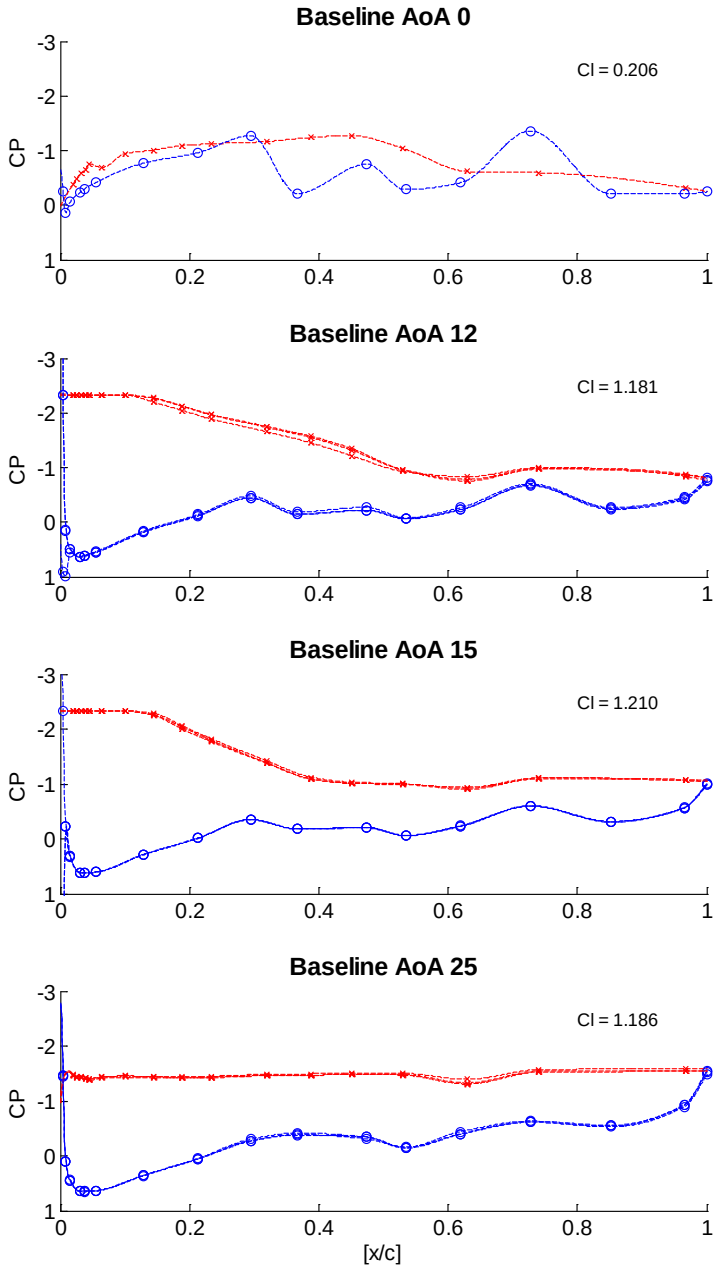

Figure 11: S809 Surface Pressure Distributions

The integrated values of lift coefficients determined from the pressure distribution followed the same trend as those determined from the load cell measurements. In the stall condition at twenty-five degrees angle of attack, the suction surface pressure distribution is constant, as would be expected from the occurrence of separation at the leading edge.

The measured pressure distributions were qualitatively similar to those obtained by Somers [5] and Ramsay [21]. Ramsay measured pressure distributions at a Reynolds number of 1.0 million and Somers at a Reynolds number of 2.0 million. The Reynolds number tested in this study was 1.2 million. The surface pressure distributions were illustrated below in Figure 12.

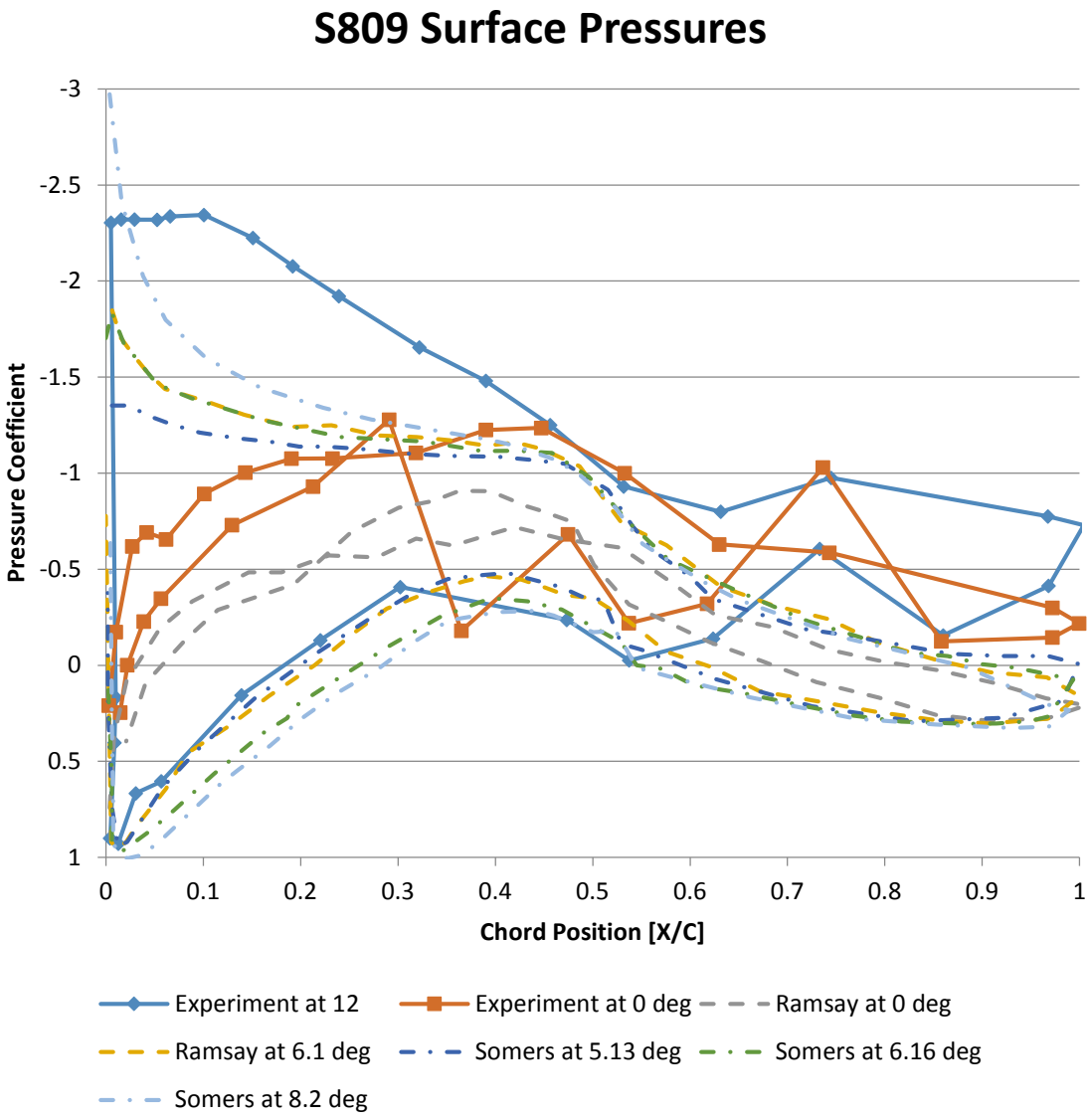

Figure 12: S809 Pressure Distributions [5] [21]

The trend of near constant pressure on the suction surface across the first thirty percent of the chord was observed in all cases for finite angles of attack. The pressure results in the present experiment were from a higher angle of attack and correspondingly lower pressure were observed on the suction surface in comparison to the historic data. The results on the pressure surface of the airfoil were directly in line with those from the other studies until the trailing edge, where the present experiment had very low tap fidelity and failed to capture the nonlinearities.

It was noted that the small suction peaks detected at the leading edge in the historic data was not resolved in the present experiments. Tap resolution near the leading edge was limited due to the tape. These differences likely were the largest attributers to differences between the calculated force based and the pressure based coefficients.

Lift data from this experiment was plotted in conjunction with the data reported by Somers and Ramsay. Both historic experiments for this data set were conducted at a Reynolds number of 1.0 million. The present experiment was performed with a Reynolds number of 1.2 million.

The lift coefficient at zero angle of attack was calculated to be 0.10 in this experiment. Somers reported a lift coefficient of 0.14 and Ramsay of 0.07. The lift curve slope in the linear region was reported as 0.114 per degree by Somers and 0.118 per degree by Ramsay. The results of this experiment were 0.092, twenty percent lower than those reported in historic data. The present experiment also exhibited a 17 percent higher maximum lift coefficient. This trend would be expected due to the higher Reynolds number.

Both historic data cases exhibited a first stall region near ten degrees before completely stalling near fifteen. The present experiment did not resolve this phenomena due to a limited number of test cases. However, evidence of this stall did appear later in the data, discussed in Section 4.3.

The lift coefficient values were within 3 percent of each other between the load cell and surface pressure based measurements. The surface pressure based value deviated significantly at the zero angle of attack and stall angle of attack. These differences were attributed to the increased degree of nonlinearity in the pressure distribution of these cases. The lift curves were plotted together in Figure 13.

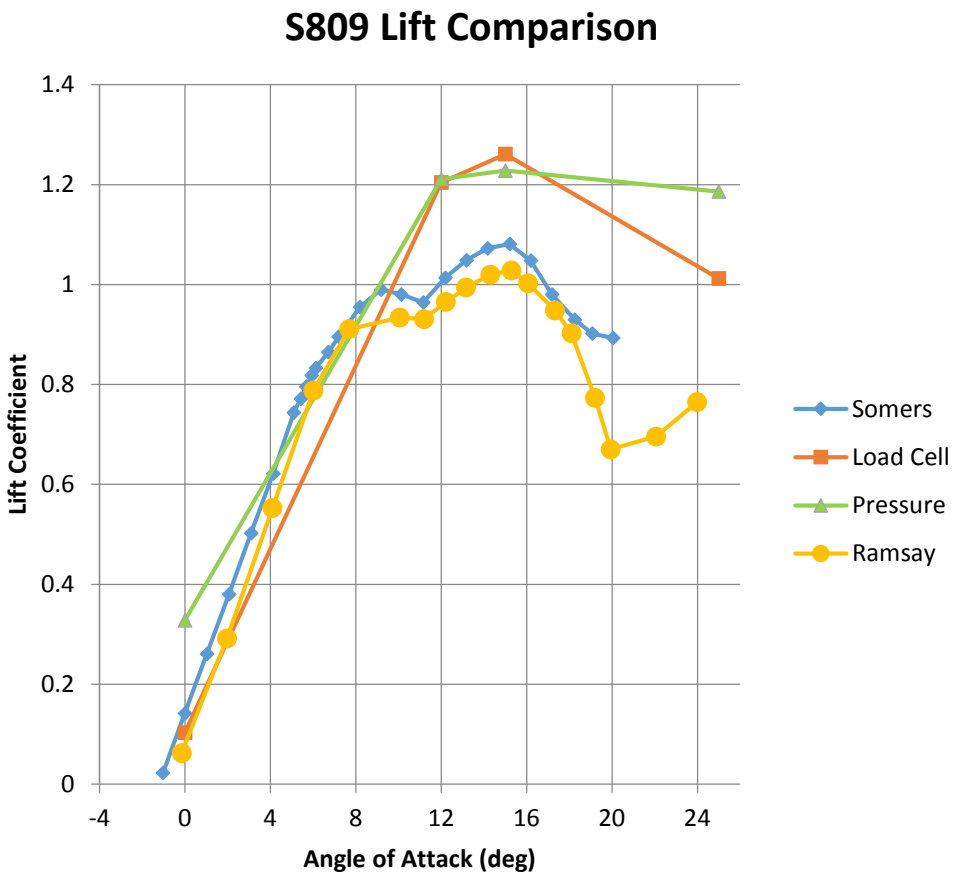

Figure 13: S809 Lift Curves [5] [21]

This analysis of the measurement and post processing techniques for the S809 and comparison to known data was used in order to validate the use of the same procedures in the full scale treatment testing of the tip section, discussed in Section 4.3. The historic source data was included in Appendix A.

The tip section was first investigated to determine the angle of attack at which stall occurred. This was performed by installing yarn tufts across the suction surface of the section. Separation was seen to occur slightly aft of the leading edge. The stall angle was twenty degrees for the baseline and 21.5 degrees with the treatment applied. An image of the tip section with attached tufts and treatment applied is included below as Figure 14. The upstream microphones are also visible in the image.

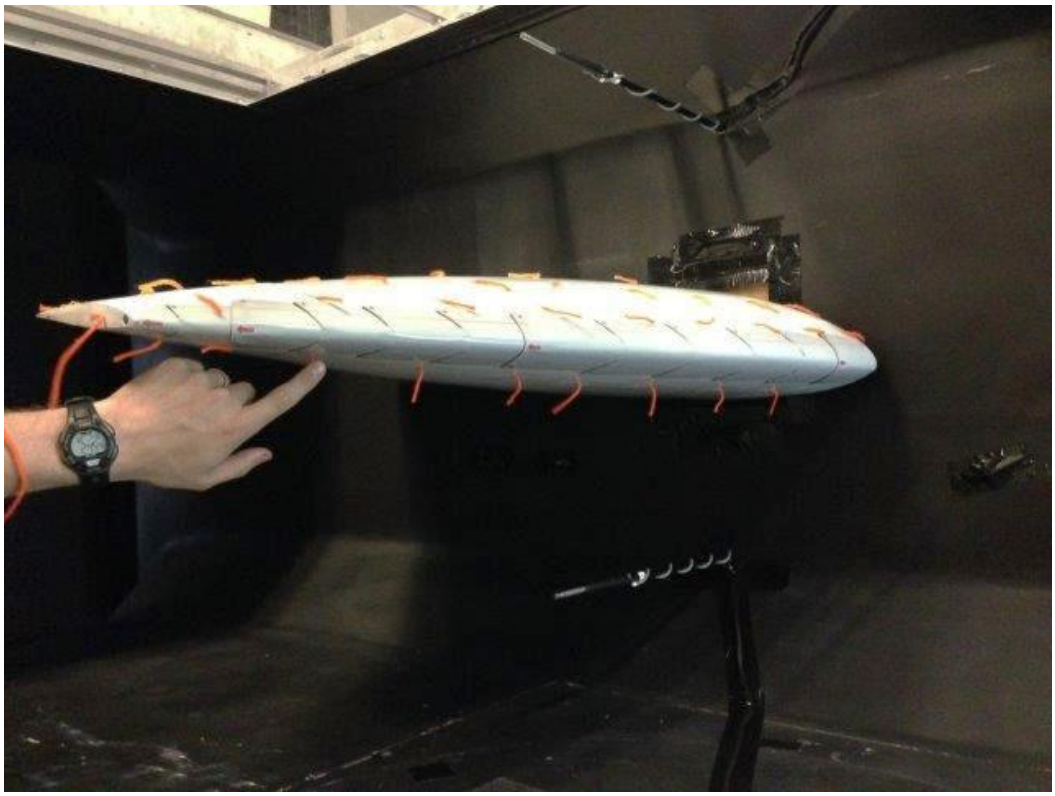

Figure 14: Tip Section with Treatment and Tufts

After determining the stall conditions, tests were performed at angles of attack of 0, 10, 15, 19, 20, 21, and 22 degrees. For angles of attack from 0 to 15 degrees, tests were performed at tunnel speeds of twenty and forty meters per second, corresponding to root based Reynolds numbers of 1.29 and 2.57 million. For angles of attack from 19 to 22, the tests were only performed at twenty meters per second due to the limited capacity of the load cell in cantilevered position with respect to bending moment from the lift force. Load cell measurements were taken for four runs and acoustic measurements were collected on the first run.

The exact planform area and chord distribution of the tip section were not determined due to the proprietary nature of the geometry. Therefore, sectional lift and drag coefficients were calculated per unit area. Similarly, moment was reported in units of cubic meters.

Table 4: Tip Section Baseline Results at Re = 1.29M

Base 20m/s			
AoA	CL*S	CD*S	CM*S*c
0	0.040	0.013	-0.027
10	0.389	0.046	-0.041
15	0.558	0.084	-0.052
19	0.697	0.121	-0.059
20	0.731	0.136	-0.064
21	0.759	0.149	-0.068
22	0.784	0.162	-0.073

Table 5: Tip Section Baseline Results at Re=2.57M

Base 40m/s			
AoA	CL*S	CD*S	CM*S*c
0.00	0.03	0.01	-0.03
10.00	0.37	0.06	-0.04
15.00	0.53	0.11	-0.05

4.3 Treatment Aerodynamic Effects

Data collection taken from the load cells was considered the most quantitatively reliable measurement taken in this study for the determination of aerodynamic performance. Unlike the pressure measurements, the load cells directly measured the forces of interest and thus numerical post-processing was not required to obtain quantitatively meaningful results. Additionally, the data set was not discretized as the pressure measurements and unsteady effects were averaged out across four moderate duration tests whereas the pressure measurements only had a few instantaneous results.

For these reasons, the load cell data is used for most quantitative comparison of aerodynamic performance results. The pressure data allowed for insight into the physical phenomena driving the results of the force data.

In application to the S809 airfoil, the protective tape resulted in significant loss of lift at an angle of attack of zero. Lift was recovered at high angles of attack and finally a significant gain was indicated in the deep stall condition of twenty-five degrees. The measured lift coefficients were plotted in Figure 15 below.

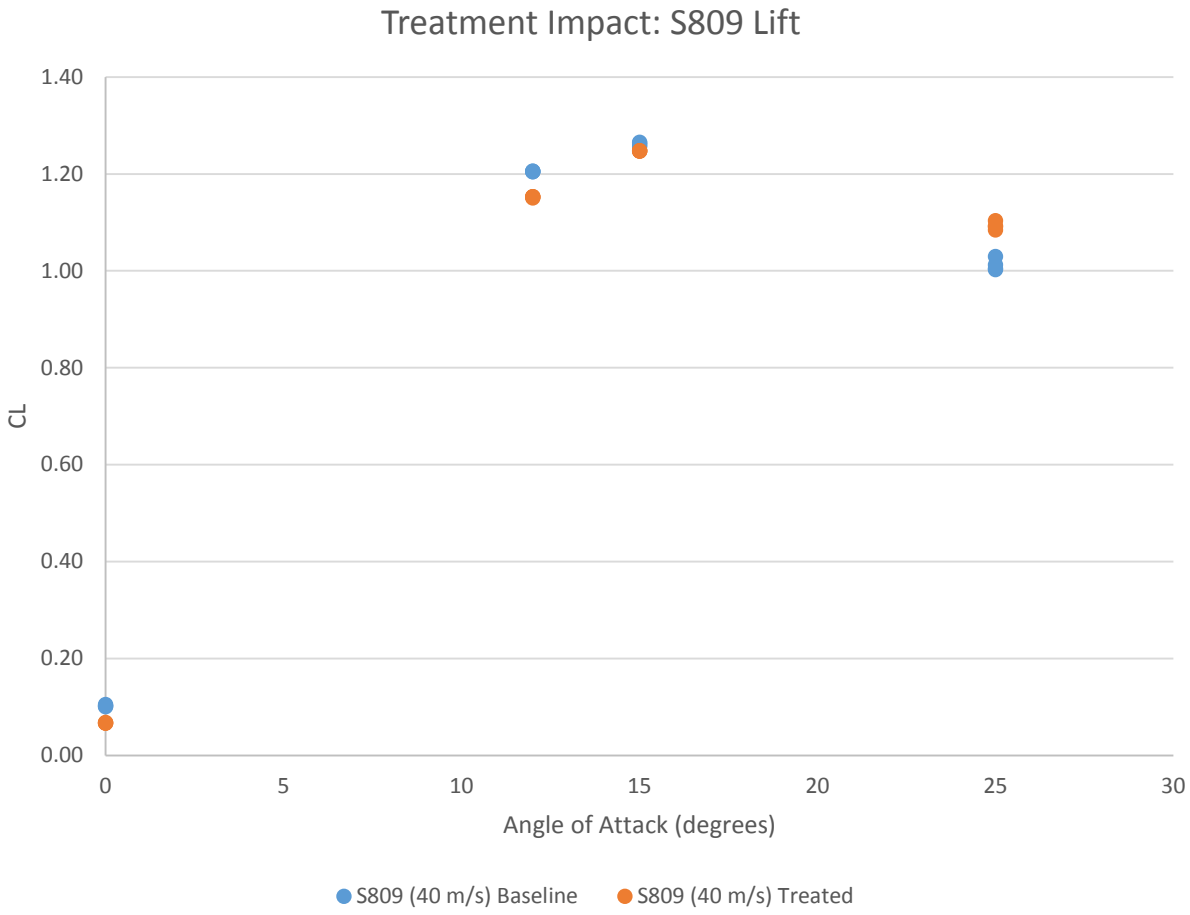

Figure 15: Treatment Impact: S809 Lift

The lift recovered measured in the deep stall condition is attributed to partial reattachment of the flow near the leading edge. This reattachment is due to the sharp rear edge step of the treatment acting as a boundary layer trip, transitioning the flow to turbulence. This transition increases boundary layer momentum and delays separation. This can be seen in pressure distributions shown in Figure 16. The pressure distributions from all three runs are overlaid in the plots. The treatment application results in reattachment for the approximately five percent of the chord in the first two runs, and separation was delayed to approximately ten percent chord in the third run.

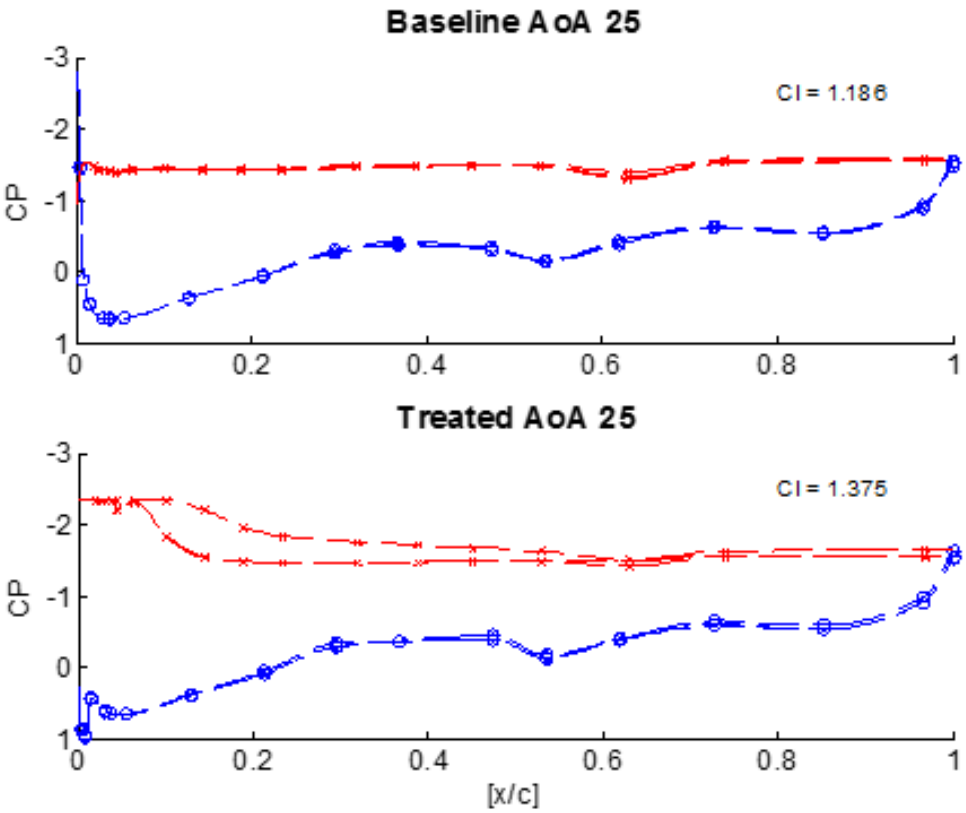

Figure 16: Stall Pressure Distributions

The measured drag coefficients are plotted below in Figure 17. Overall, the treatment had near null effect at low angles of attack and added drag at high angle of attack. The increase in drag is attributed to an increase in momentum thickness occurring near the leading edge due to the step of the tape. Earlier onset of turbulence due to the step may also have contributed to the detected increase in drag.

It was noted that the drag at twelve degrees decreased from the baseline. This occurred in the realm where the first partial stall was noted to occur in the historic data in the previous section. It is anticipated the treatment improved flow attachment at this angle of attack due to the partial stall.

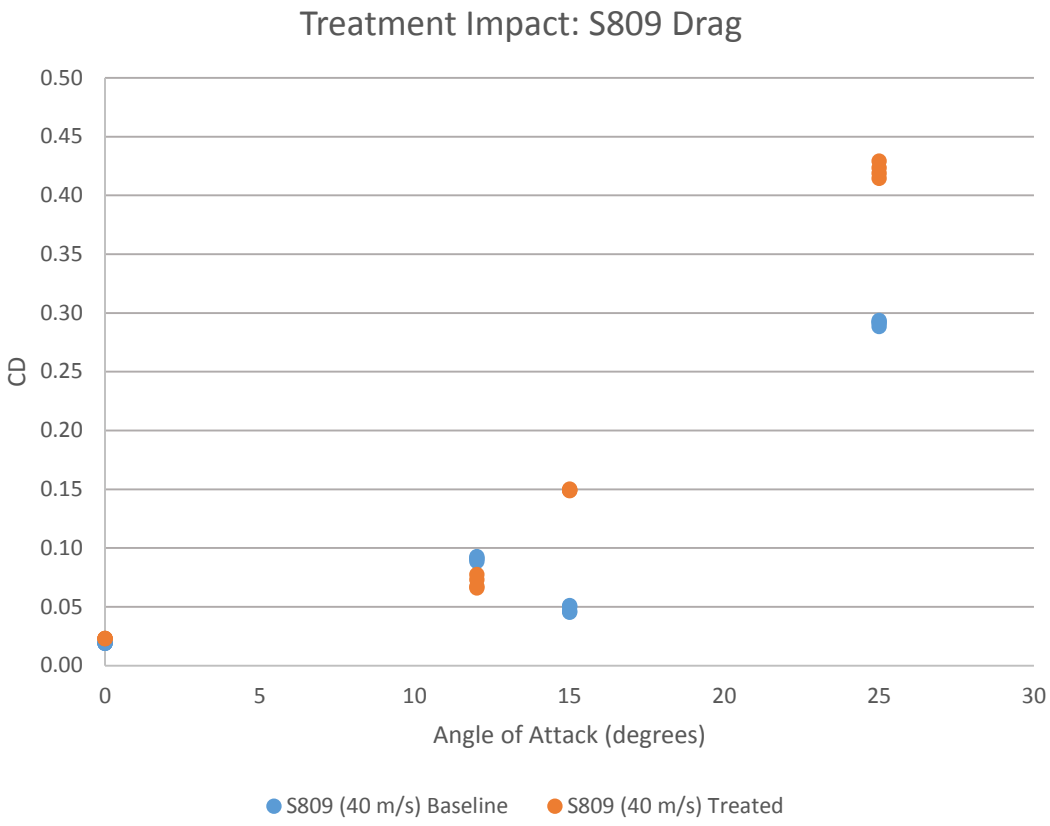

Figure 17: Treatment Impact: S809 Drag

The baseline drag measurement for the fifteen degree angle of attack cases was found to be an abnormality, actually decreasing in value from the previous angle of attack. This was not measured in the pressure wake derived drag coefficient which determined a value of 0.15, a close match with the treated case from the load cell results. The load cell based values for drag in the baseline case were therefore rejected as erroneous. The wake data for this case is plotted below in Figure 18.

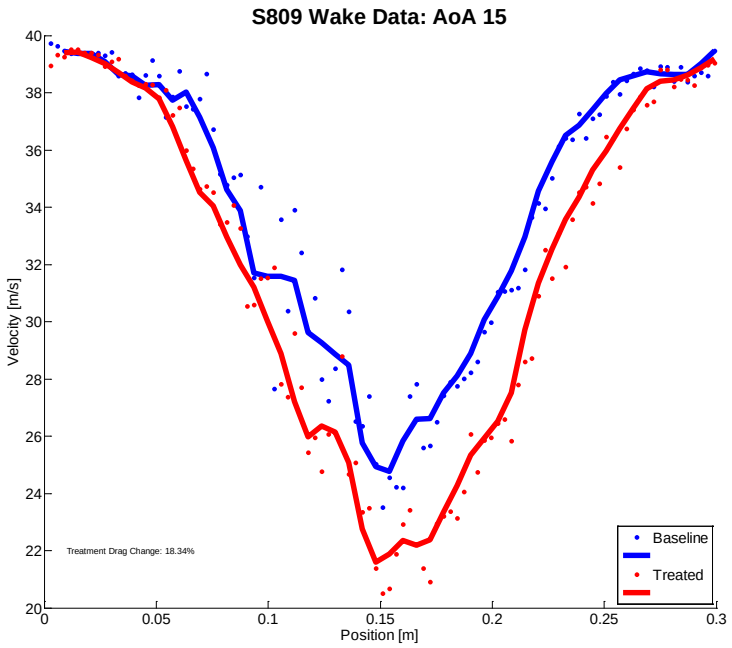

Figure 18: S809 Wake at 15 Degrees

A reduction in moment was measured at the zero angle of attack case, but there was little impact at any other test condition. The moment results were plotted as Figure 19.

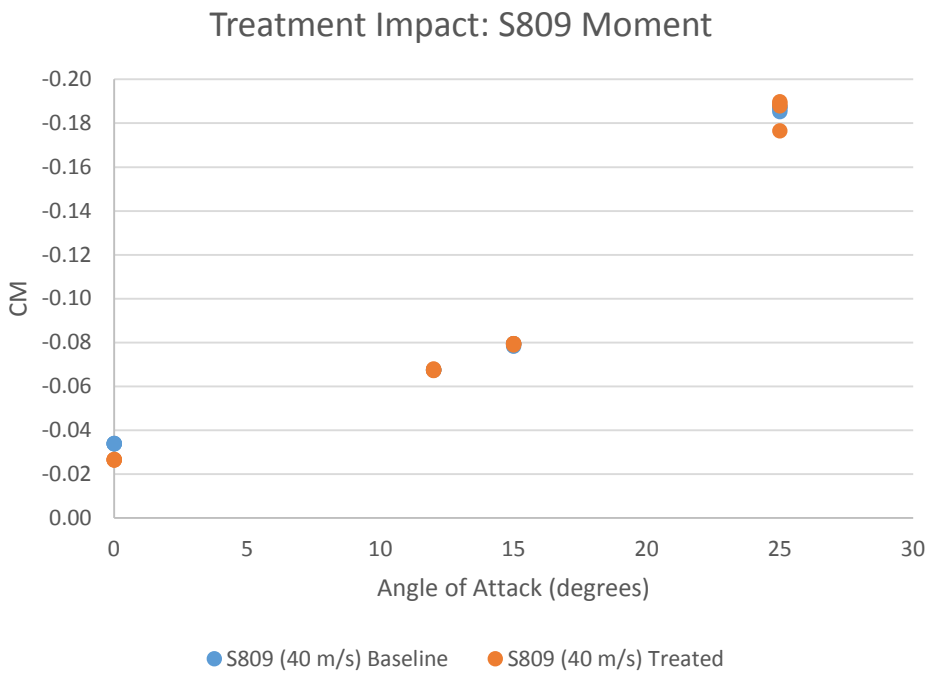

Figure 19: Treatment Impact: S809 Moment

The load cell measurements taken during the S809 testing are summarized below by change in aerodynamic coefficients from the baseline to treated cases in Table 6. Individual test results for each treated case were included in Appendix B and the baseline results were included in Section 4.2.

Table 6: S809 Load Cell Data Comparisons

S809 Load Cell Data Comparisons			
AoA	CL	CD	CM
0.00	-34.6%	21.0%	-21.6%
12.00	-4.4%	-21.8%	0.0%
15.00	-1.1%	209.9%	0.2%
25.00	8.0%	44.6%	-0.4%

The data processed from the wake pressure measurements was used in order to construct a map of the velocity profile behind the airfoil. The wakes for angles of attack of 12 and 25 were included below as Figure 20 and Figure 21 respectively. The wake at 15 degrees was previously included as Figure 18.

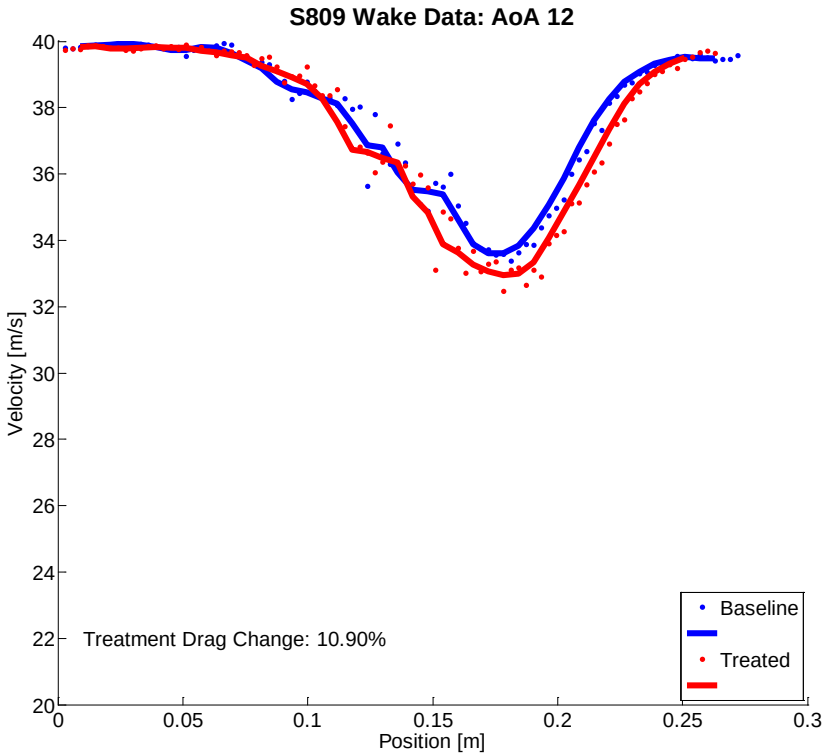

Figure 20: S809 Wake at 12 Degrees

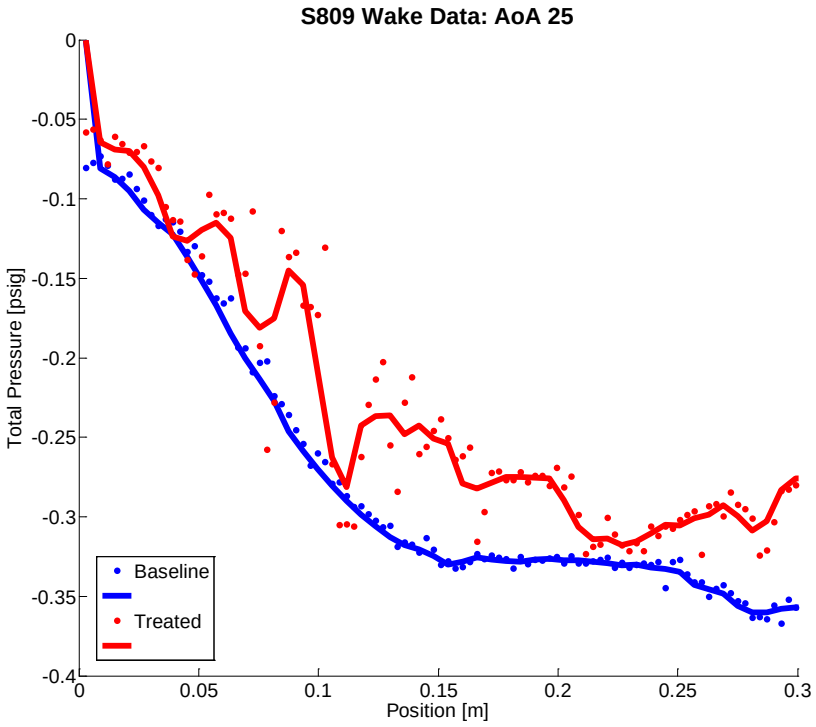

Figure 21: S809 Wake at 25 Degrees

In the case of the airfoil in deep stall conditions, the wake behind the test article extended far beyond the reach of the traverse. This can be seen in the figure as there is no pressure recovery at any point in the wake. For this reason, drag coefficients could not be processed from the momentum deficit when in deep stall conditions.

However, the recorded data did indicate a significant reduction in the averaged momentum deficit for the treated case. This is opposed to the load measurements taken for the same case which indicated an increase in drag due to the treatment. It was noted that the unsteadiness in the treated data set was very high relative to the baseline case where the discrete points aligned very closely with the averaged line. This was attributed to a higher degree of turbulence resulting from the step at the edge of the protective tape and may have led to the data discrepancy between the wake and load cell measurements.

The full scale treatment application to the tip section was performed in a standard configuration, as well as with poor application and backward application. In the first alternative treatment configuration, testing was conducted with the protective coating partially delaminated. In the

second, the protective coating was installed upside down relative to the manufacture design. In the full scale testing, four runs of load cell data were taken for each test case with acoustic measurements being taken on the initial run. The alternative configuration tests were conducted only at an angle of attack of fifteen degrees.

The treatment showed a consistent loss of lift across the operating envelope. Like the S809, the loss of lift was most severe at low angles of attack and was mostly recovered by stall. Deep stall conditions were not tested on the tip section due to wind tunnel blockage constraints, so the post stall lift recovery could not be verified, although the trend is the same. The lift results were plotted in Figure 22.

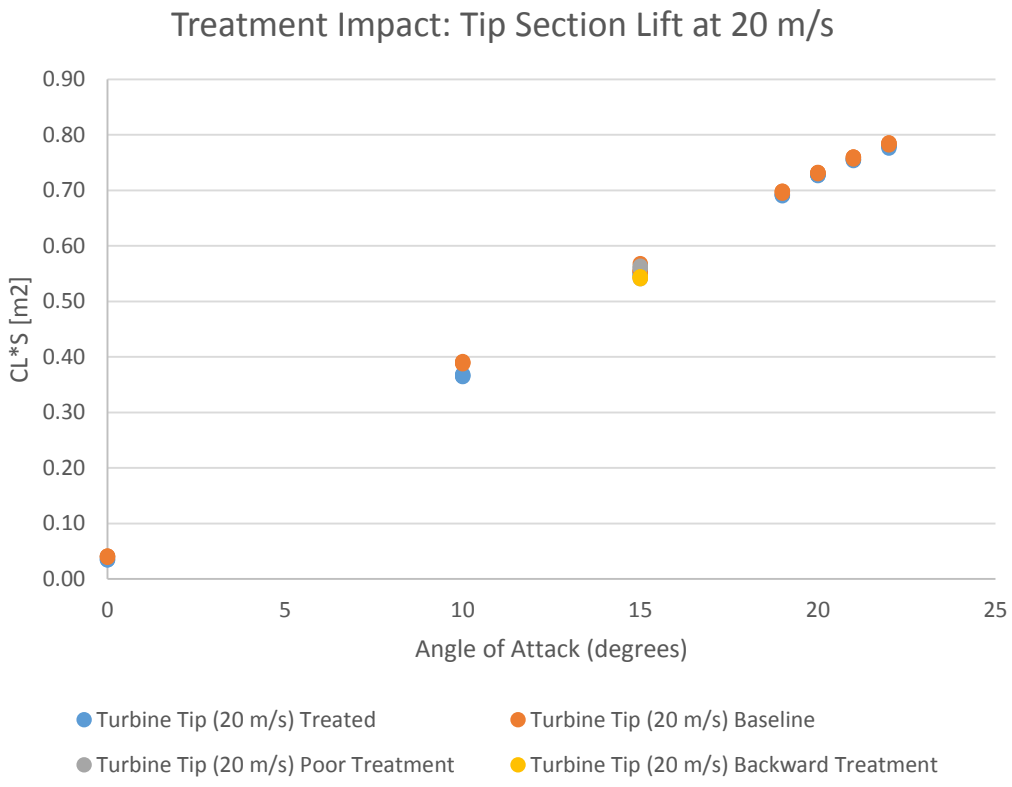

Figure 22: Treatment Impact- Tip Section Lift at Re=1.29M

The drag results indicated a substantial increase at the zero angle of attack condition but near null change at any other test point. An improvement in drag was noted to have occurred in the 10-15 degree region. This improvement is anticipated to be due to the initial partial stall phenomena observed in the S809 airfoil. This range, the treatment improves flow attachment thereby

improving aerodynamic performance. The drag results were plotted below as Figure 23. Moment changes were also small and were plotted in Figure 24.

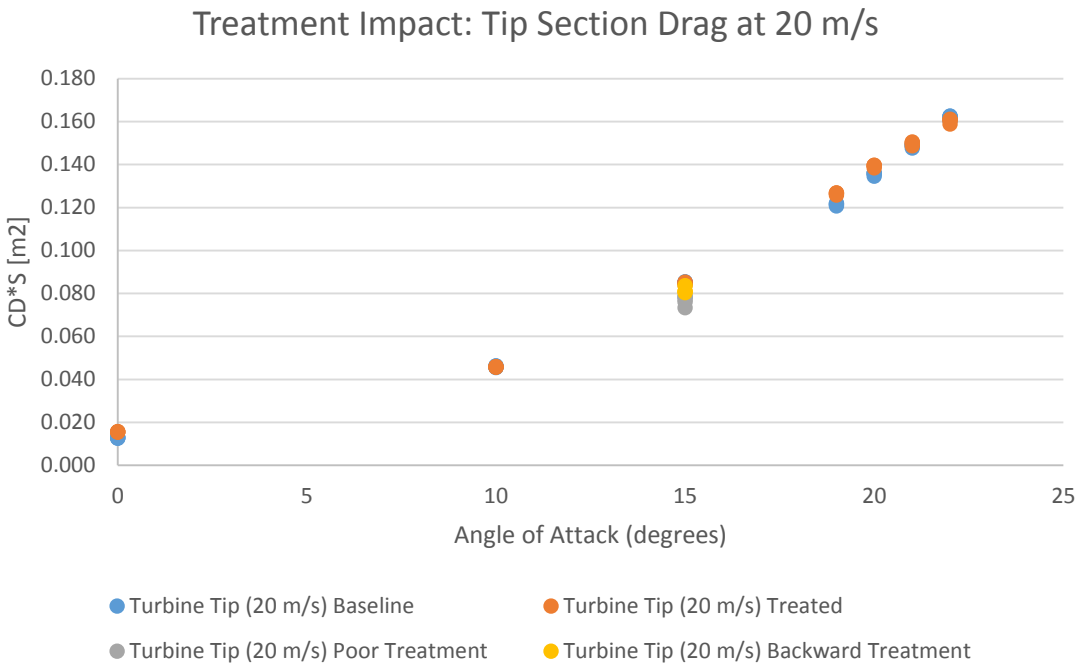

Figure 23: Treatment Impact: Tip Section Drag at Re=1.29M

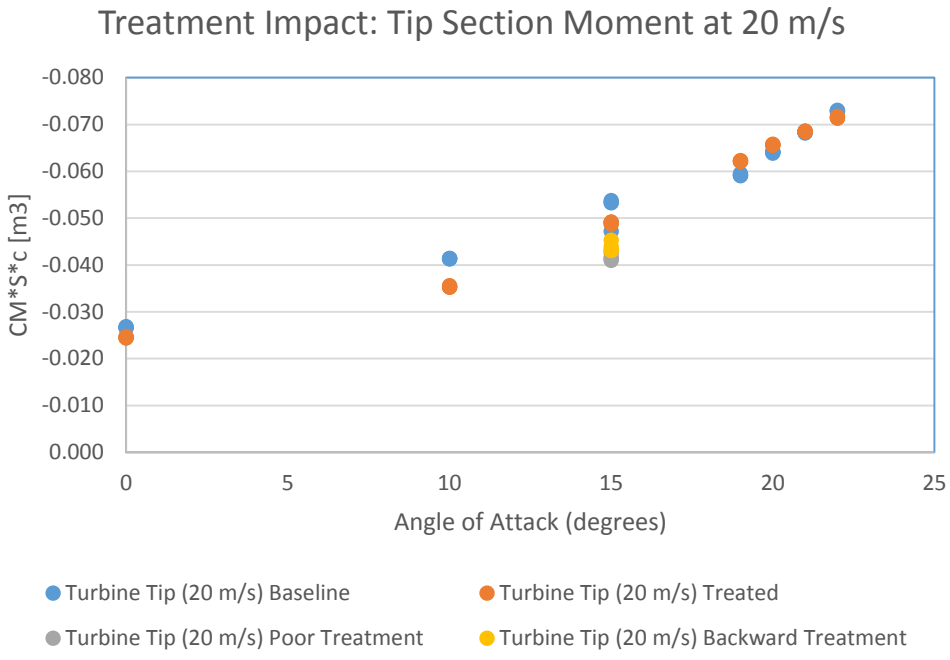

Figure 24: Treatment Impact: Tip Section Moment at Re=1.29M

The load cell results of the tip section testing were summarized below in Table 7 and Table 8 as relative changes to the aerodynamic coefficients from the baseline to treatment cases. The load cell measurements for the treated tip section were reported in Table 9 and Table 10. The determined values for each run were placed in Appendix B. Overall; the loss of aerodynamic efficiency for the treated tip section was on the order of one percent or less.

Table 7: Tip Summary at Re=1.29M

AoA	CL	CD	CM
0	-10.4%	21.9%	-8.1%
10	-6.0%	-0.2%	-14.5%
15	-1.5%	1.5%	-5.5%
19	-0.8%	4.1%	5.0%
20	-0.5%	2.7%	2.5%
21	-0.5%	0.7%	0.3%
22	-0.7%	-1.0%	-1.9%

Table 8: Tip Summary at Re=2.57M

AoA	CL	CD	CM
0	-5.14%	17.46%	-6.41%
10	-4.80%	-2.51%	-11.66%
15	-2.41%	2.91%	1.01%

Table 9: Tip Section Treated at Re=1.29M

AoA	CL	CD	CM
0	0.036	0.016	-0.025
10	0.366	0.046	-0.035
15	0.549	0.085	-0.049
19	0.691	0.126	-0.062
20	0.727	0.139	-0.066
21	0.755	0.150	-0.069
22	0.779	0.160	-0.072

Table 10: Tip Section Treated at Re=2.57M

AoA	CL	CD	CM
0	0.03	0.02	-0.02
10	0.35	0.06	-0.04
15	0.51	0.12	-0.05

The plots of load cell data in the above plots for the tip section were all for testing at a tunnel speed of twenty meters per second. Plots from test results at forty meters per second were included in Appendix A: Additional Figures.

Qualitative testing was performed in order to evaluate the adhesion strength of the protective tape product. The tip section was installed in a downstream orientation such that airflow moved backward over the blade. In the condition the model was tested for thirty minutes at a velocity of forty meters per second. No delamination of the coating was found in visual inspection following the test. Following inspection, the coating was intentionally partially delaminated from the leading edge. The model was then tested, still in the downstream orientation, for ten minutes at forty meters per second. No increase in delamination was detected by inspection following the test.

The standard deviation in each data set was included in the tables below. For the S809 measurements, the uncertainty within 95 percent confidence is at worst 0.007, 0.003, and 0.003 for the lift, drag, and moment coefficients respectively. For the tip section, there is uncertainty of 0.005, 0.002, and 0.002 for the lift, drag, and moment quantities respectively.

Table 11: S809 Measurement Deviation

Angle		C_L	C_D	C_M		C_L	C_D	C_M
0	Baseline	0.0017	0.0001	0.0001	Treated	0.0007	0.0001	0.0001
12		0.0005	0.0015	0.0001		0.0115	0.0045	0.0003
15		0.0034	0.0024	0.0005		0.0125	0.0005	0.0003
25		0.0106	0.0018	0.0009		0.0109	0.0055	0.0054
Mean		0.0041	0.0015	0.0004		0.0089	0.0027	0.0015
Max		0.0106	0.0024	0.0009		0.0125	0.0055	0.0054

Table 12: Tip Section Deviation at Re=1.29M

Angle		CL*S	CD*S	CM*S*c		CL*S	CD*S	CM*S*c
0	Baseline	0.0009	0.0002	0.0001	Treated	0.0021	0.0001	0.0001
10		0.0014	0.0003	0.0001		0.0018	0.0001	0.0001
15		0.0059	0.0030	0.0027		0.0025	0.0006	0.0002
19		0.0014	0.0005	0.0002		0.0088	0.0004	0.0001
20		0.0010	0.0006	0.0001		0.0006	0.0005	0.0001
21		0.0014	0.0006	0.0001		0.0009	0.0006	0.0001
22		0.0016	0.0009	0.0001		0.0016	0.0009	0.0001
Mean		0.0019	0.0009	0.0005		0.0015	0.0005	0.0001
Max		0.0059	0.0030	0.0027		0.0088	0.0009	0.0002

Table 13: Tip Section Deviation at Re=2.57M

Angle		CL*S	CD*S	CM*S*c		CL*S	CD*S	CM*S*c
0	Baseline	0.0006	0.0001	0.0001	Treated	0.0011	0.0001	0.0001
10		0.0005	0.0005	0.0001		0.0008	0.0003	0.0001
15		0.0078	0.0022	0.0029		0.0006	0.0003	0.0002
Mean		0.0030	0.0009	0.0010		0.0009	0.0002	0.0001
Max		0.0078	0.0022	0.0027		0.0011	0.0003	0.0002

4.4 Treatment Acoustic Effects

The power spectral density was plotted for each of the acoustic measurements taken during the testing. The facility used for testing was not a quiet tunnel, therefore the acoustic measurements were largely dominated by the noise of tunnel operation.

In the plots, the power spectral density for each microphone were overlaid with a ten decibel offset to aid clarity. A sample case was included below as Figure 25. All power spectral density plots were included in Appendix A.

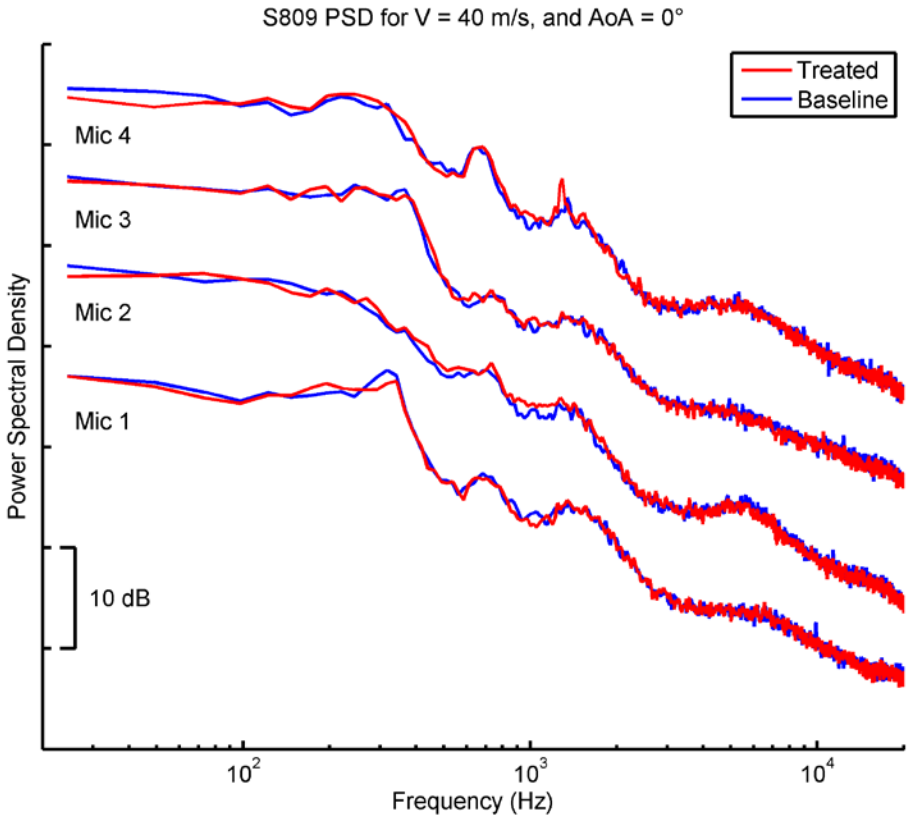

Figure 25: Sample Power Spectral Density

The primary motivation to acoustic testing was to determine if the treatment excited any acoustic frequency such that 'whining' could be heard in the surrounding vicinity of a wind turbine using the leading edge tape product. There were no distinct frequency excitations detected in any of the test results.

In addition to the spectral analysis, the overall sound pressure level, expressed in decibels, was calculated from the microphone data at each test condition. The percent difference between the baseline and treated sound pressure levels were presented in Table 14. No significant deviation in acoustic levels was detected in any case.

Table 14: Percent Change in Overall Sound Pressure Levels

Article	Type	V(m/s)	AoA(°)	Mic1	Mic2	Mic3	Mic4
S809	Treated	40	0	-0.083	-0.178	-0.280	-0.053
S809	Treated	40	12	0.138	0.045	0.023	-0.030
S809	Treated	40	15	0.347	0.091	0.149	0.140
S809	Treated	40	25	-0.415	-0.575	-0.007	-0.634
Tip	Treated	20	0	0.239	0.475	0.111	0.212
Tip	Treated	20	10	0.544	0.379	0.022	-0.228
Tip	Treated	20	15	0.658	0.500	0.083	0.009
Tip	Treated	20	19	1.005	1.373	0.141	-0.331
Tip	Treated	20	20	1.055	0.687	-0.230	-0.627
Tip	Treated	20	21	0.586	1.199	0.066	-0.272
Tip	Treated	20	22	2.446	1.497	0.369	-0.222
Tip	Treated	40	0	-0.438	-0.250	-0.275	-0.234
Tip	Treated	40	10	0.179	0.160	-0.103	-0.094
Tip	Treated	40	15	-0.127	0.057	-0.118	-0.114
Tip	Uplifted	20	15	-1.346	0.055	-0.997	-1.071
Tip	Uplifted	40	15	-0.098	-0.473	0.184	-0.066
Tip	Mis-Applied	20	15	-0.508	-0.090	-1.088	-0.765
Tip	Mis-Applied	40	15	-0.027	0.156	-0.383	-0.004

5. Conclusions

Two articles were tested in order to primarily determine the aerodynamic impact of applying a leading edge protective tape, and secondarily to investigate the acoustic effects. The test articles used were a S809 airfoil and a full scale commercial turbine tip section. A scaled mock-up of a protective treatment was applied to the S809 in testing and a commercial treatment product was applied to the turbine tip.

Measurements were taken via 6-axis load cells in order to directly obtain the forces of lift and drag, as well as the pitching moment. For the S809 airfoil, pressure measurements were also taken from surface pressure taps and a wake survey. These measure measurements gave a degree of redundancy for confirmation of the measurements, as well as provided insight into the physical mechanisms affecting the flow field. However, the discrete nature of the pressure measurements and lack of time resolved data left a significant degree of uncertainty in these

measurements. The uncertainty of the load cell measurements was quantified in Section 4.3. The low uncertainty in load cell based calculations made these measurements the focus for analysis.

Testing was first performed on the S809 airfoil and baseline results were compared to historical data available in literature. The measurement methods and post-processing techniques were validated in Section 4.2 via comparison to the trends published in literature.

Both airfoils exhibited similar trends in regard to the effect of the leading edge treatment. At low angles of attack, lift generation was impeded by the presence of the protective tape. This was caused by a loss of suction near the step at the end of the protective tape. At higher angles of attack, this issue became less prevalent and the tape had little bearing across most of the operational envelope. At high angles of attack, the step caused by the presence of the tape aided in flow attachment and preserved lift where it would have otherwise been lost due to stall.

Drag on the test articles increased. This was attributed to the step behind the leading edge tape where a small recirculation zone likely formed. This would increase momentum thickness on the suction surface and by extension the drag. For the S809 airfoil, drag rise of 10-20% was detected due to the treatment. For the tip section, a twenty percent increase in drag was measured at the zero angle of attack case but, like lift, the detrimental impact became far less significant at higher angles of attack.

In the regular operating envelope of the airfoil, the leading edge tape application had little impact on lift generation. The exception to this was at the zero angle of attack condition, where a significant loss of lift was detected for both the S809 and the tip section.

The pressure distribution data from Figure 11 illustrated that the distributions were nearly identical in both cases for the S809 at zero angle of attack except near the leading edge. In this region, a small area of lift was lost that was formerly present in the baseline case. A sharp gradient was detected immediately behind the tape in the treated case, indicating a potential pressure loss caused by the step.

The treatment had the anticipated effect in stall conditions on the S809. The boundary layer was tripped which retained attached flow at higher angles of attack. This effect was documented in Figure 16. The baseline case demonstrated fully separated flow by the pressure contour across

the suction surface being constant. However, in the treated case, the low pressure region near the leading edge remains, indicating that the flow remained attached farther downstream.

This effect is caused by the backward facing step at the end of the leading edge tape. While the step does result in an increase in momentum thickness and contribute higher drag, it also energizes the boundary layer by the addition of turbulence which helps to maintain attached flow and ultimately reduce drag in conditions were the airfoil would otherwise stall. In these conditions, the addition of the tape retains lift, resulting in a gain compared to the baseline conditions.

Acoustic measurements were collected from four locations for each test condition. Two measurements were taken from the suction side of the test articles and two from the pressure side, with one on each side being near the quarter-chord position and the others measuring from a downstream position. Power spectral densities and overall sound pressure levels were calculated from the collected data. No substantial acoustic changes were detected as a result of the protective tape application.

References

[1] American Wind Energy Association, "4th Quarter 2014 Public Market Report," 2015.

[2] U.S. Energy Information Administration, "Total Electric Power Industry Summary Statistics," 2013. [Online]. Available: http://www.eia.gov/electricity/annual/html/epa_01_01.html. [Accessed March 2015].

[3] The World Wind Energy Association, "2014 Half Year Report," 2014.

[4] K. Gharali and D. A. Johnson, "Numerical Modeling of an S809 Airfoil under Dynamic Stall, Erosion, and High Reduced Frequencies," *Applied Energy,* vol. 93, pp. 45-52, 2011.

[5] D. Somers, "Design and Experimental Results for the S809 Airfoil," National Renewable Energy Laboratory, Golden, Colorado, 1997.

[6] K. Wood, "Blade Repair: Closing the Maintenance Gap," *Composites Technology,* 2011.

[7] L. Rempel, "Rotor Blade Leading Edge Erosion," *Wind Systems Magazine,* 2012.

[8] D. Quarton, "Wind Energy Technology and the Research Challenge," in *Wind Energy Centre for Doctoral Training Seminar: FutureWind*, Glasgow, UK, 2013.

[9] M. Keegan, D. Nash and M. M. Stack, "On Erosion Issues Associated with the Leading Edge of Wind Turbine Blades," *Journal of Physics D: Applied Physics,* vol. 46, 2013.

[10] F. Sayer, F. Burkner, B. Buchholz, M. Stobel, A. van Wingerde, H. Bushmann and H. Seifert, "Influence of a Wind Turbine Service Life on the Mechanical Properties of the Material and Blade," *Wind Energy,* vol. 16, pp. 163-174, 2013.

[11] A. Sareen, S. A. Chinmay and M. S. Selig, "Effects of Leading Edge Erosion on Wind Turbine Blade Performance," *Wind Energy,* vol. 17, pp. 1531-1542, 2013.

[12] N. Gaudern, "A Practical Study of the Aerodynamic Impact of Wind Turbine Blade Leading Edge Erosion," *Journal of Physics: Conference Series*, 2014.

[13] S. Kim, J. Kim, J. Park and J. Choi, "Measurement in the Wake of an Airfoil with Regular Roughness on the Upper Surface Near the Leading edge," *Institution of Mechanical Engineeers*, vol. 220, 2006.

[14] G. Corten and H. Veldkamp, "Insects Cause Double Stall," in *European Wind Energy Conference*, 2001.

[15] N. Dalili, A. Edrisy and R. Carriveau, "A Review of surface Engineering Issues Critical to Wind Turbine Performance," *Renewable and Sustainable Energy Reviews*, vol. 13, pp. 428-438, 2009.

[16] M. D. Haang, "Advances in Leading Edge Protection of Wind Turbine Blades," in *EWEA*, Vienna, Austria, 2013.

[17] W. D. Weigel, "Advanced Rotor Blade Erosion Protection System," Kaman Aerospace Corporation, 1996.

[18] P. Giguere and M. S. Selig, "Aerodynamic Effects of Leading-edge Tape on Aerofoils at Low Reynolds Numbers," *Wind Energy*, vol. 2, pp. 125-136, 1999.

[19] S. A. Chinmay, "Turbine Blade Erosion and the use of Wind Protection Tape," University of Illinois, 2012.

[20] S. Powell, "3M Wind Blade Protection Coating W4600," 3M Industrial Marketing Presentation, 2011.

[21] R. Ramsay, M. Hoffman and G. Gregorek, "Effects of Grit Roughness and Pitch Oscillations on the S809 Airfoil," National Renewable Energy Laboratory, Golden, 1999.

[22] ATI Industrial Automation, "Six-Axis Force/Torque Transducer," Apex, 2014.

Appendix A: Additional Figures

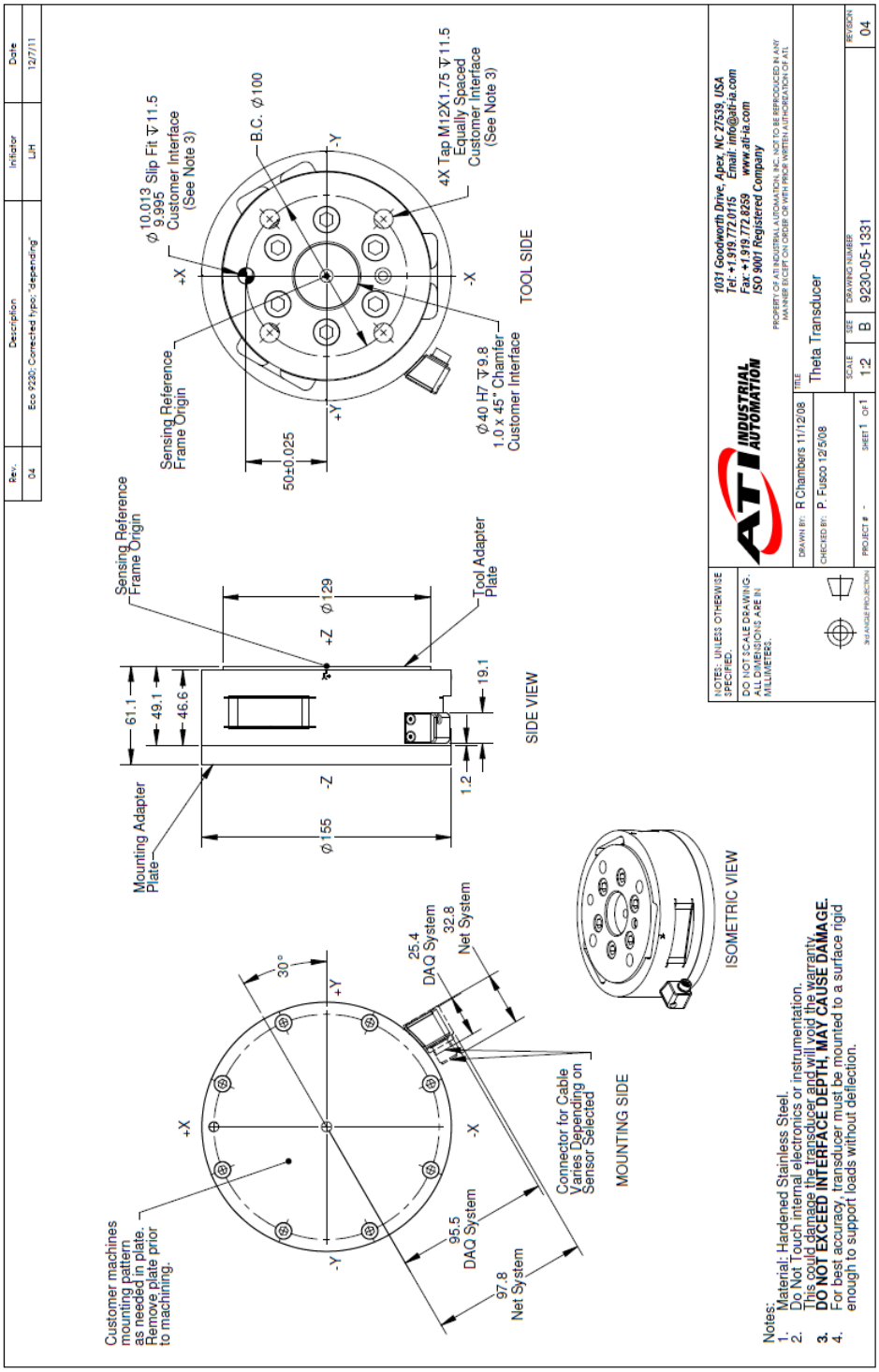

ATI Theta Load Cell Dimensions

S809 Historic Lift Data [5]

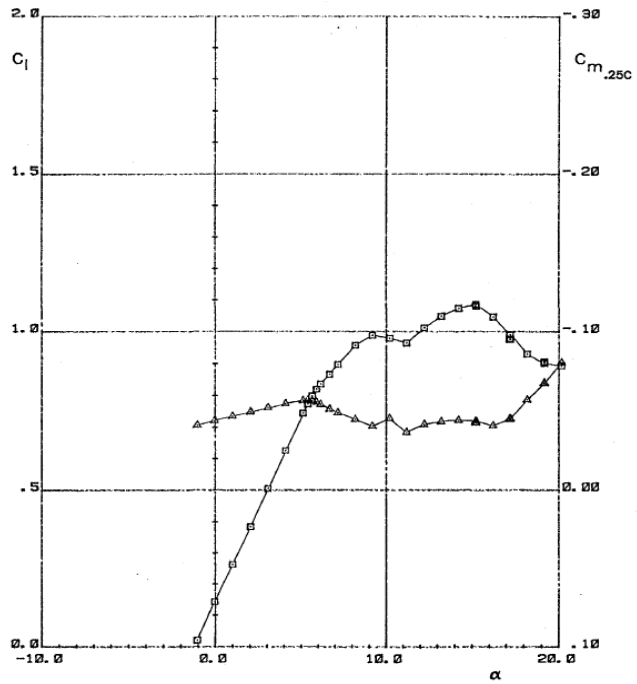

S809 Historic Pressure Distributions [5]

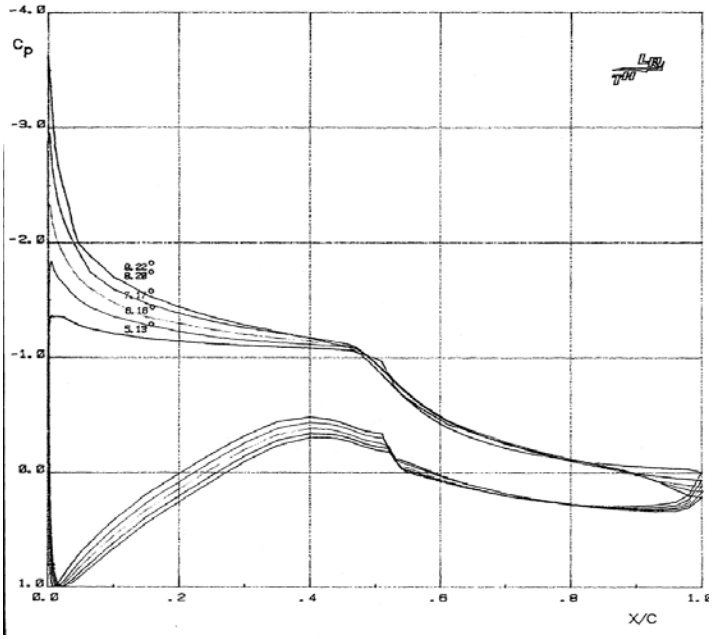

S809 Historic Lift Curve [21]

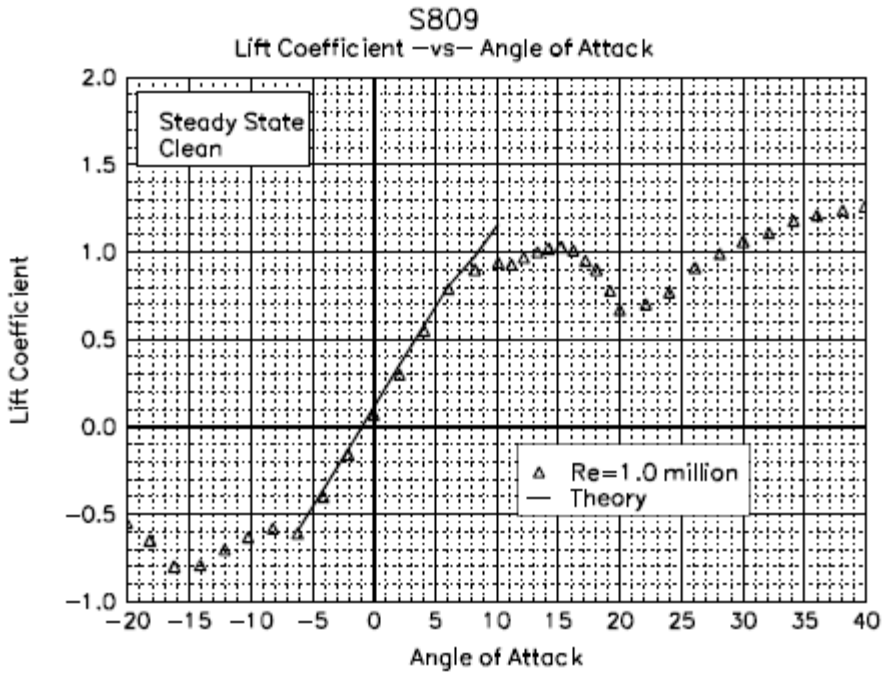

S809 Historic Pressure Distributions [21]

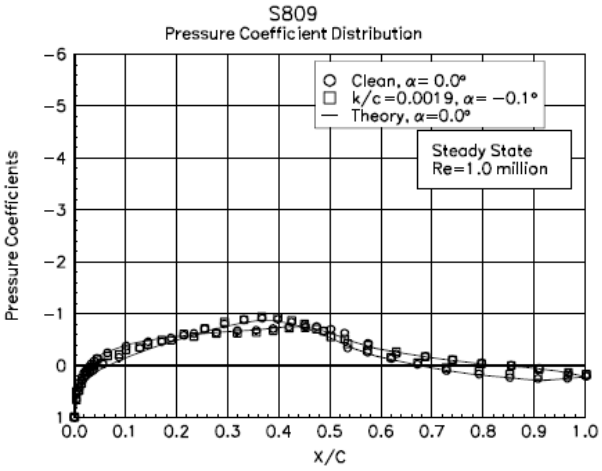

Figure 10. Comparison with theory, C_p vs x/c, α=0.0°.

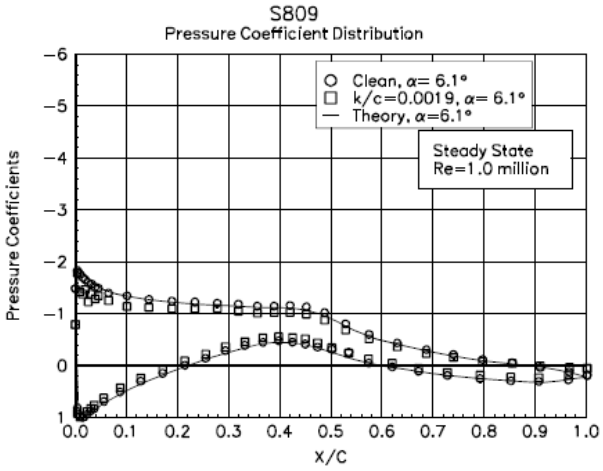

Figure 11. Comparison with theory, C_p vs x/c, α=6.1°.

S809 Surface Pressure Distributions

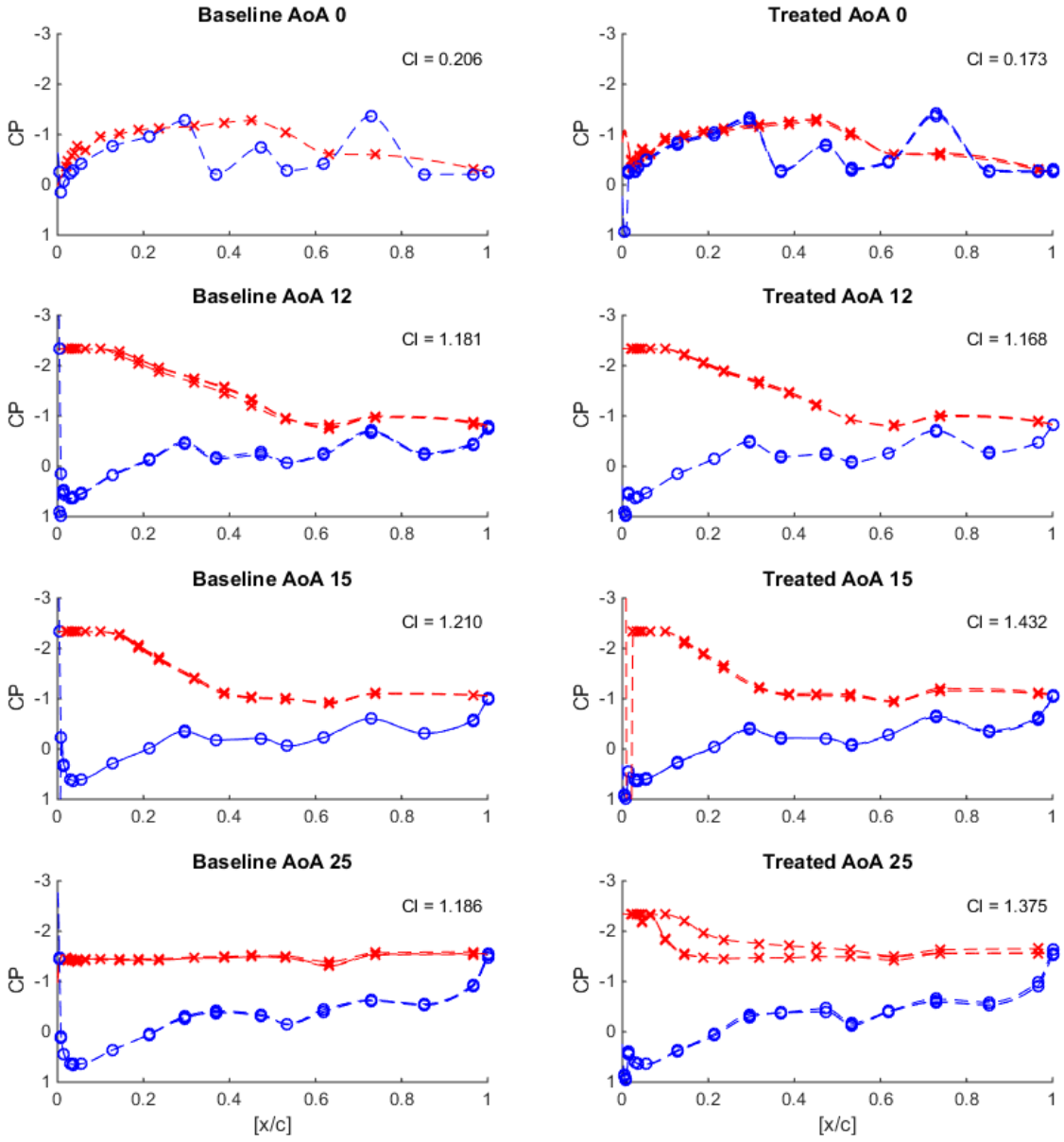

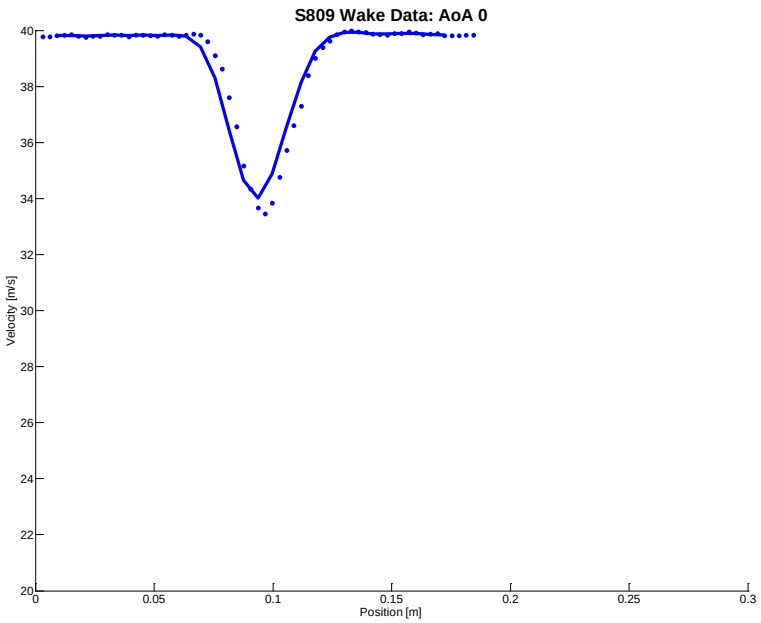
S809 Wake Data: AoA 0
Velocity [m/s]
Position [m]
40
38
36
34
32
30
28
26
24
22
20
0
0.05
0.1
0.15
0.2
0.25
0.3

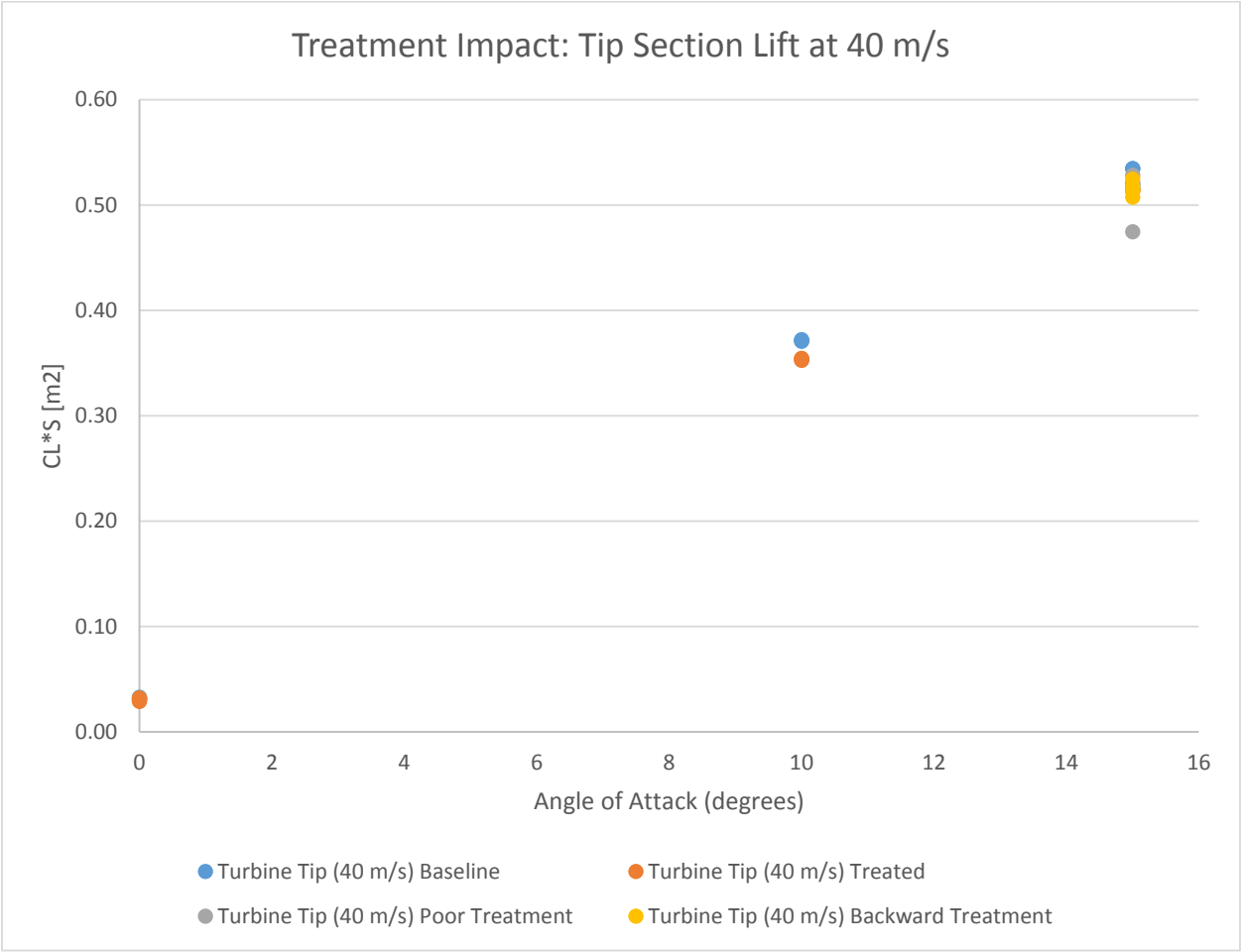
Treatment Impact: Tip Section Lift at 40 m/s
CL*S [m2]
0.60
0.50
0.40
0.30
0.20
0.10
0.00
0
2
4
6
8
10
12
14
16
Angle of Attack (degrees)
Turbine Tip (40 m/s) Baseline
Turbine Tip (40 m/s) Treated
Turbine Tip (40 m/s) Poor Treatment
Turbine Tip (40 m/s) Backward Treatment

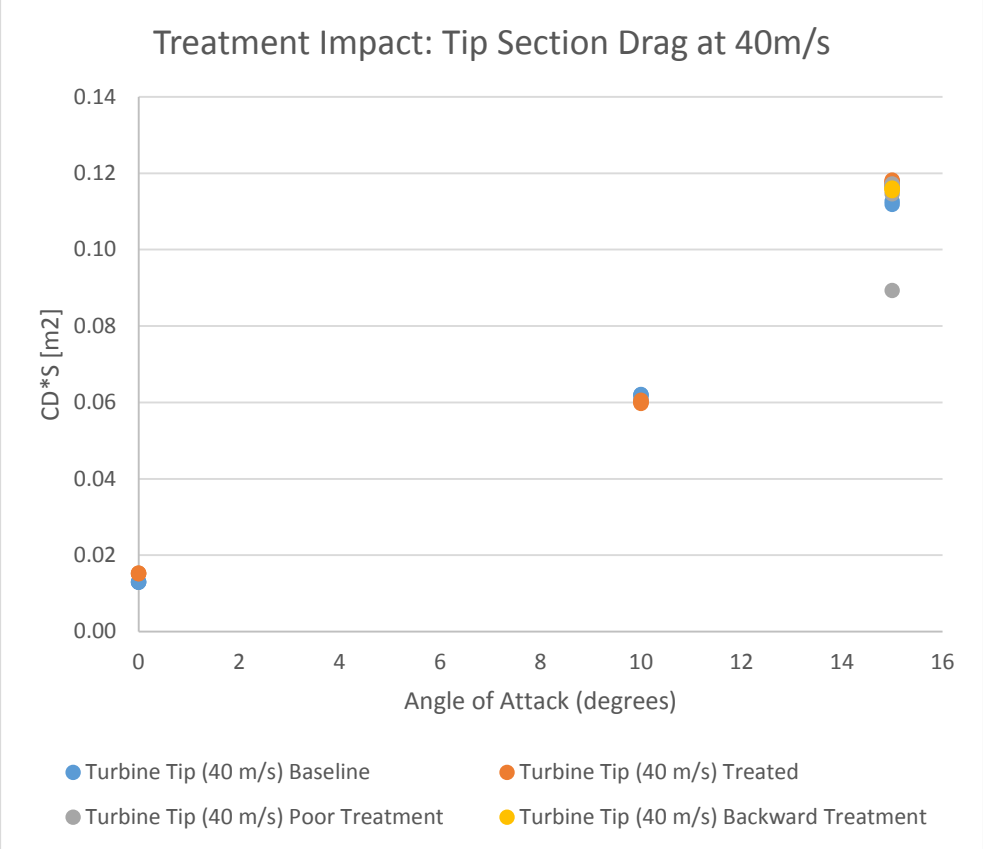
Treatment Impact: Tip Section Drag at 40m/s
CD*S [m2]
0.14
0.12
0.10
0.08
0.06
0.04
0.02
0.00
0
2
4
6
8
10
12
14
16
Angle of Attack (degrees)
Turbine Tip (40 m/s) Baseline
Turbine Tip (40 m/s) Treated
Turbine Tip (40 m/s) Poor Treatment
Turbine Tip (40 m/s) Backward Treatment

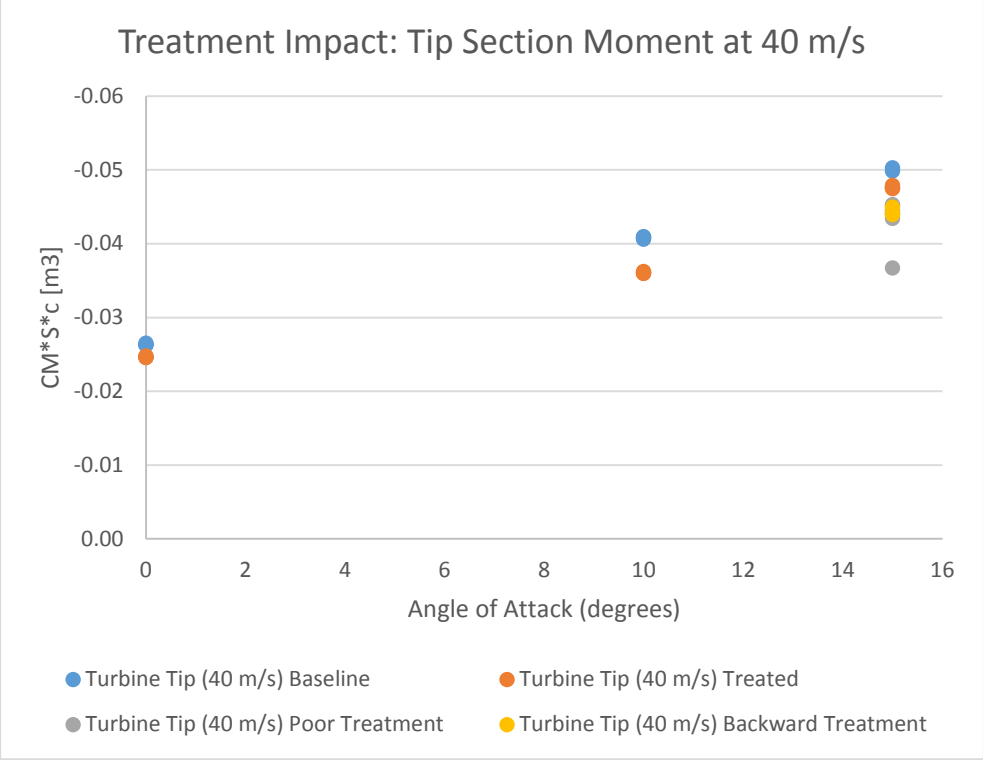
Treatment Impact: Tip Section Moment at 40 m/s
CM*S*c [m3]
-0.06
-0.05
-0.04
-0.03
-0.02
-0.01
0.00
0
2
4
6
8
10
12
14
16
Angle of Attack (degrees)
Turbine Tip (40 m/s) Baseline
Turbine Tip (40 m/s) Treated
Turbine Tip (40 m/s) Poor Treatment
Turbine Tip (40 m/s) Backward Treatment

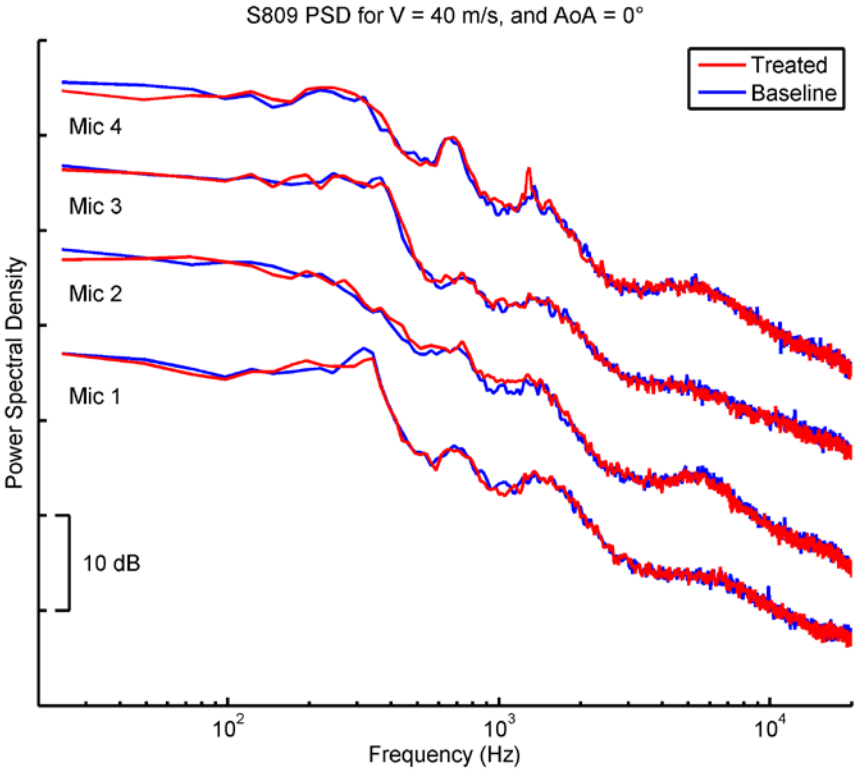
S809 PSD for V = 40 m/s, and AoA = 0°
Treated
Baseline
Mic 4
Mic 3
Mic 2
Mic 1
10 dB
Power Spectral Density
10^2
10^3
10^4
Frequency (Hz)

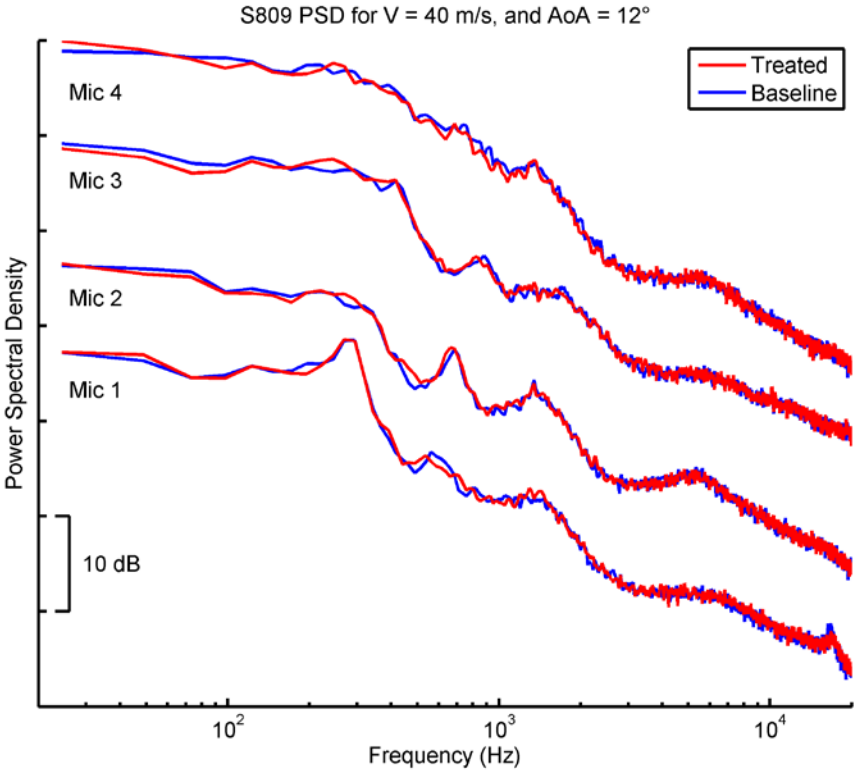
S809 PSD for V = 40 m/s, and AoA = 12°
Treated
Baseline
Mic 4
Mic 3
Mic 2
Mic 1
10 dB
Power Spectral Density
10^2
10^3
10^4
Frequency (Hz)

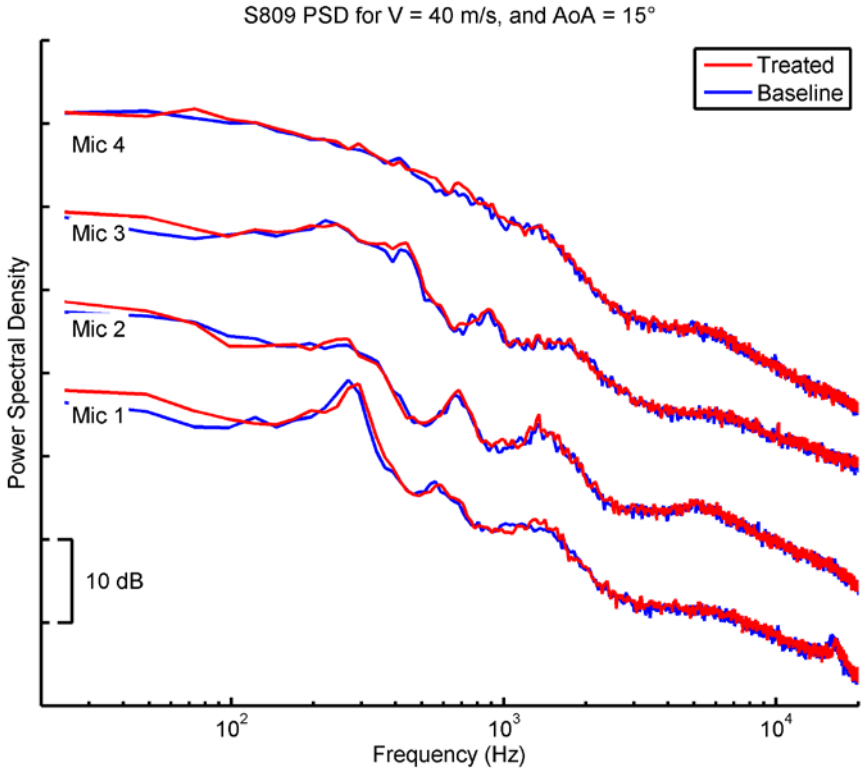
S809 PSD for V = 40 m/s, and AoA = 15°
Treated
Baseline
Mic 4
Mic 3
Mic 2
Mic 1
10 dB
Power Spectral Density
10^2
10^3
10^4
Frequency (Hz)

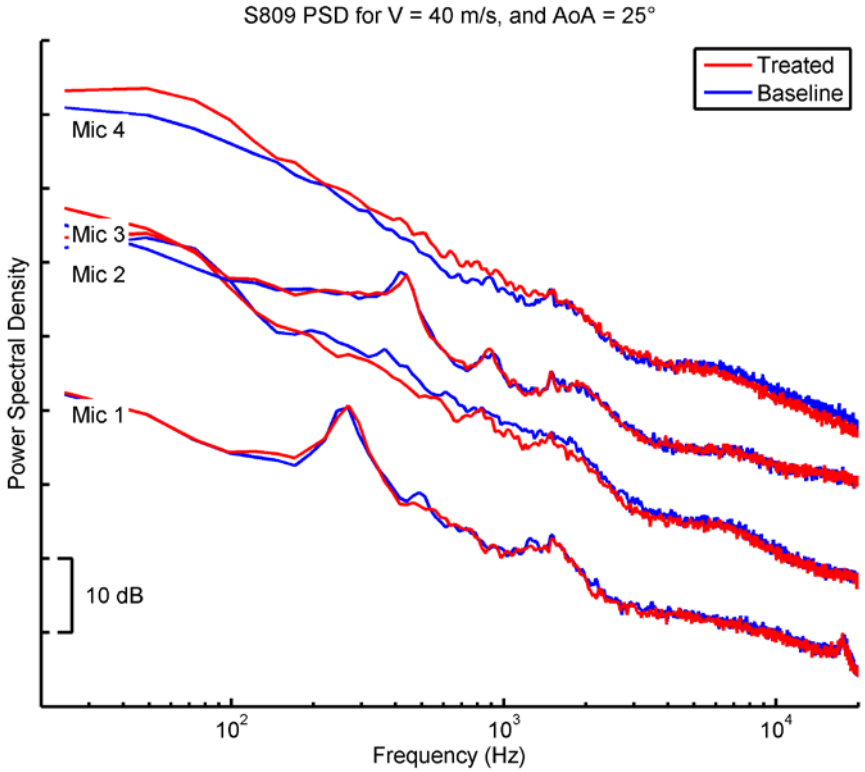
S809 PSD for V = 40 m/s, and AoA = 25°
Treated
Baseline
Mic 4
Mic 3
Mic 2
Mic 1
10 dB
Power Spectral Density
10^2
10^3
10^4
Frequency (Hz)

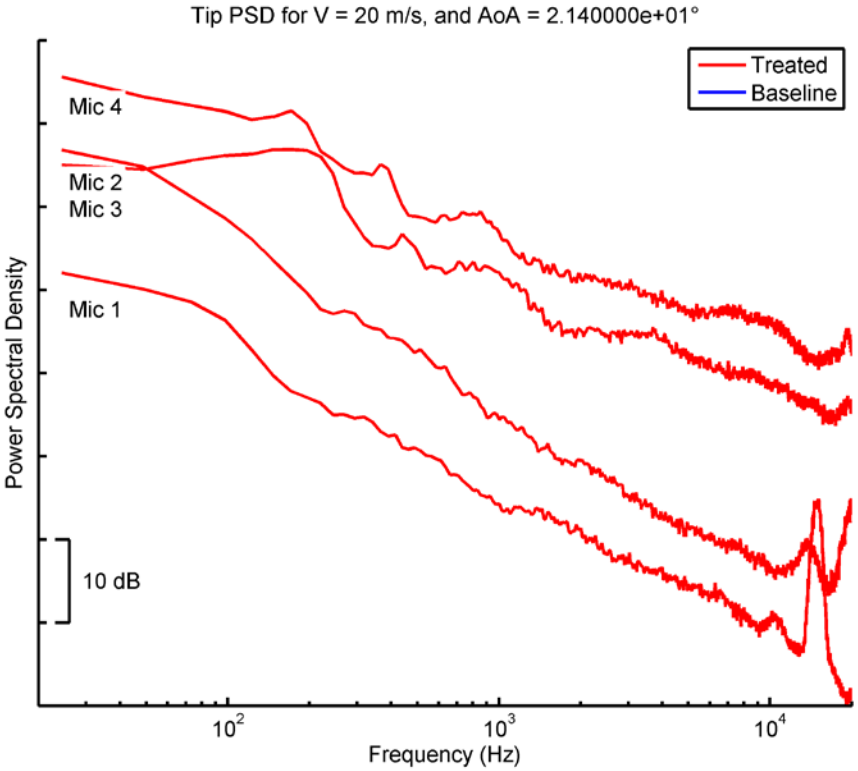
Tip PSD for V = 20 m/s, and AoA = 2.140000e+01°
Treated
Baseline
Mic 4
Mic 2
Mic 3
Mic 1
10 dB
Power Spectral Density
10^2
10^3
10^4
Frequency (Hz)

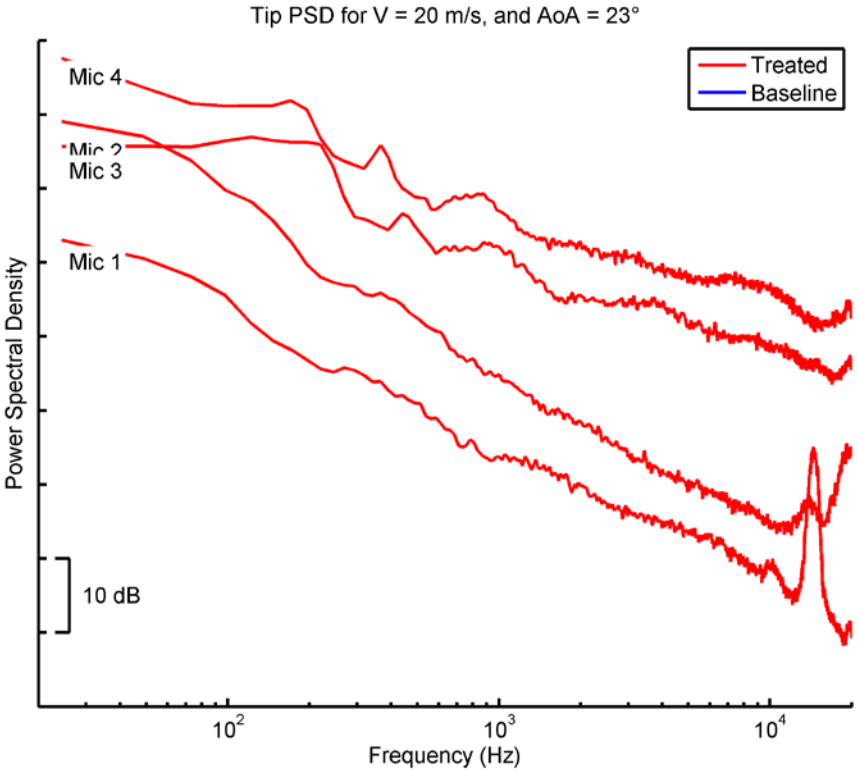
Tip PSD for V = 20 m/s, and AoA = 23°
Treated
Baseline
Mic 4
Mic 3
Mic 1
10 dB
Power Spectral Density
10^2
10^3
10^4
Frequency (Hz)

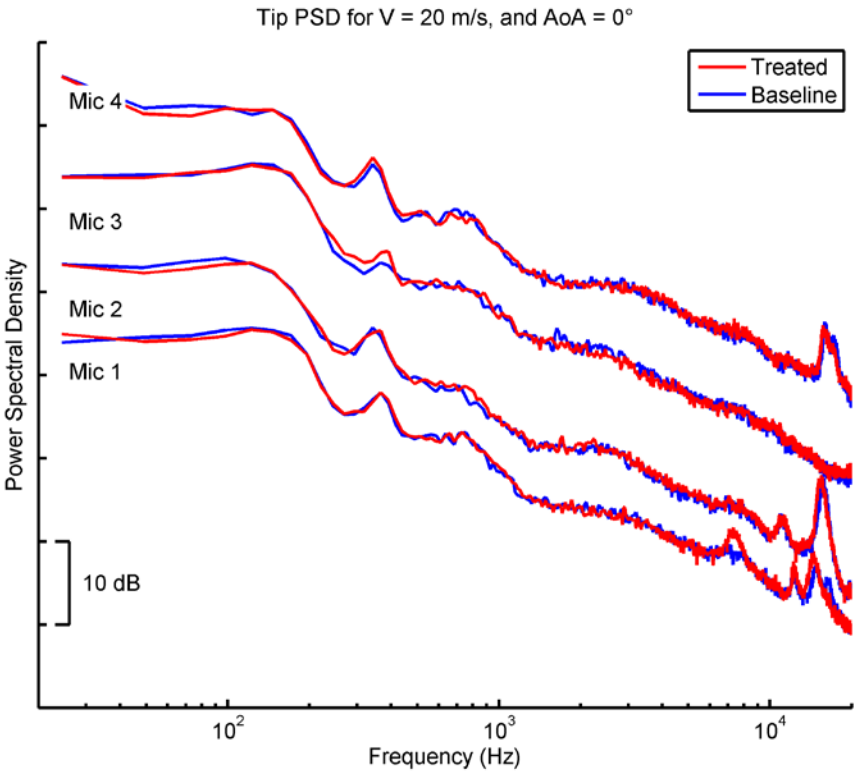
Tip PSD for V = 20 m/s, and AoA = 0°
Treated
Baseline
Mic 4
Mic 3
Mic 2
Mic 1
10 dB
Power Spectral Density
10^2
10^3
10^4
Frequency (Hz)

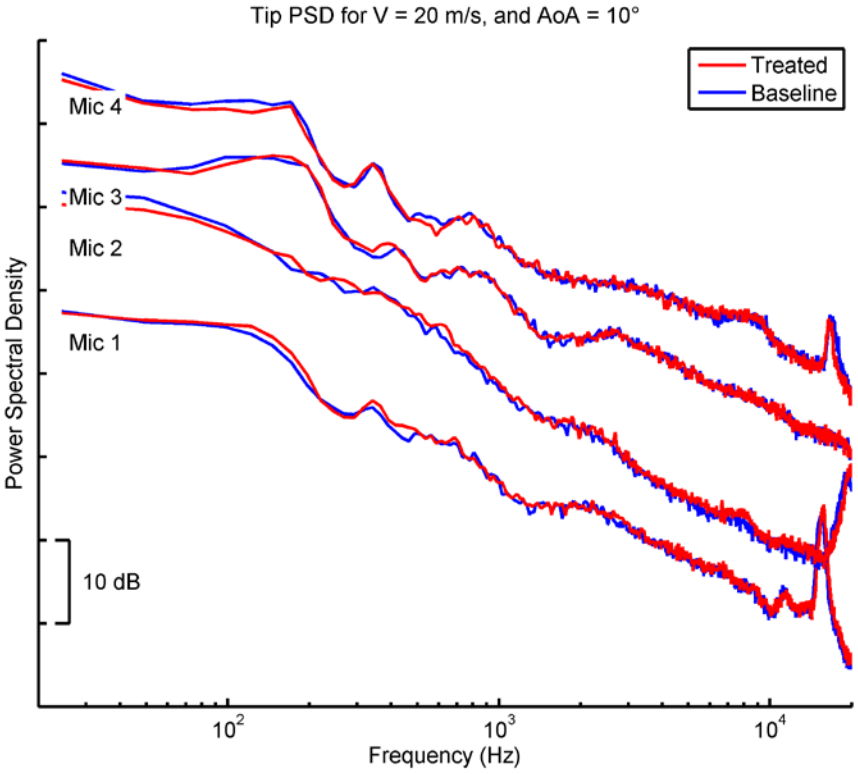
Tip PSD for V = 20 m/s, and AoA = 10°
Treated
Baseline
Mic 4
Mic 3
Mic 2
Mic 1
10 dB
Power Spectral Density
10^2
10^3
10^4
Frequency (Hz)

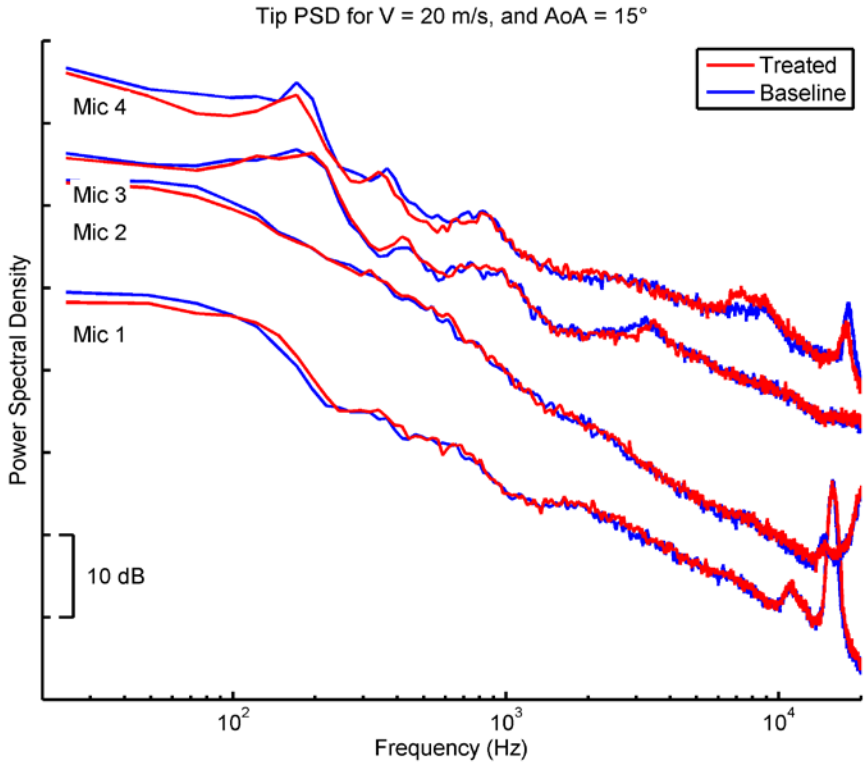
Tip PSD for V = 20 m/s, and AoA = 15°
Treated
Baseline
Mic 4
Mic 3
Mic 2
Mic 1
Power Spectral Density
10 dB
10^2
10^3
10^4
Frequency (Hz)

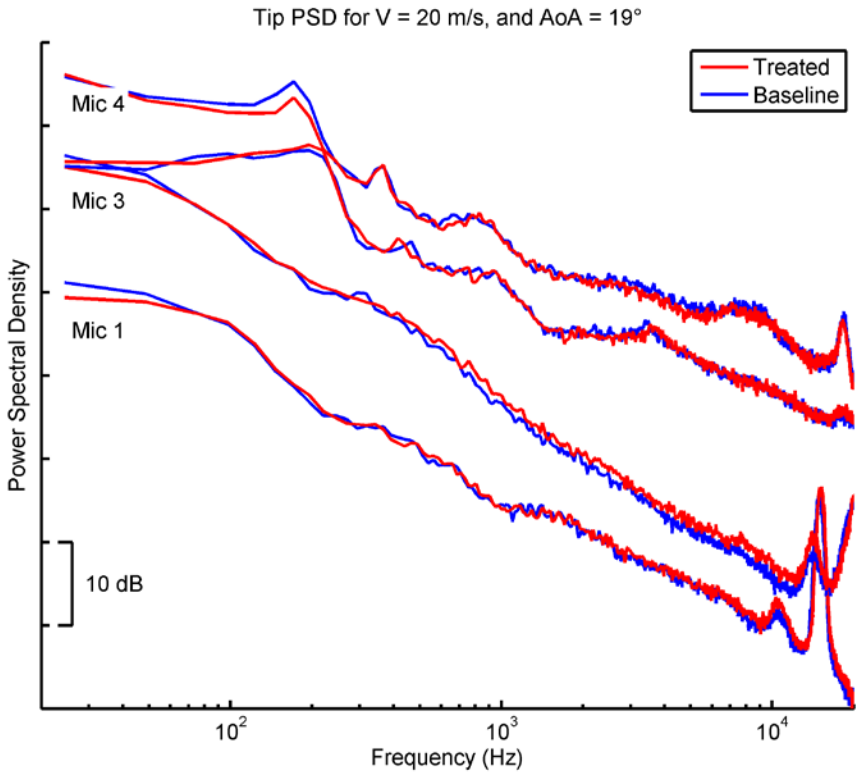
Tip PSD for V = 20 m/s, and AoA = 19°
Treated
Baseline
Mic 4
Mic 3
Mic 1
Power Spectral Density
10 dB
10^2
10^3
10^4
Frequency (Hz)

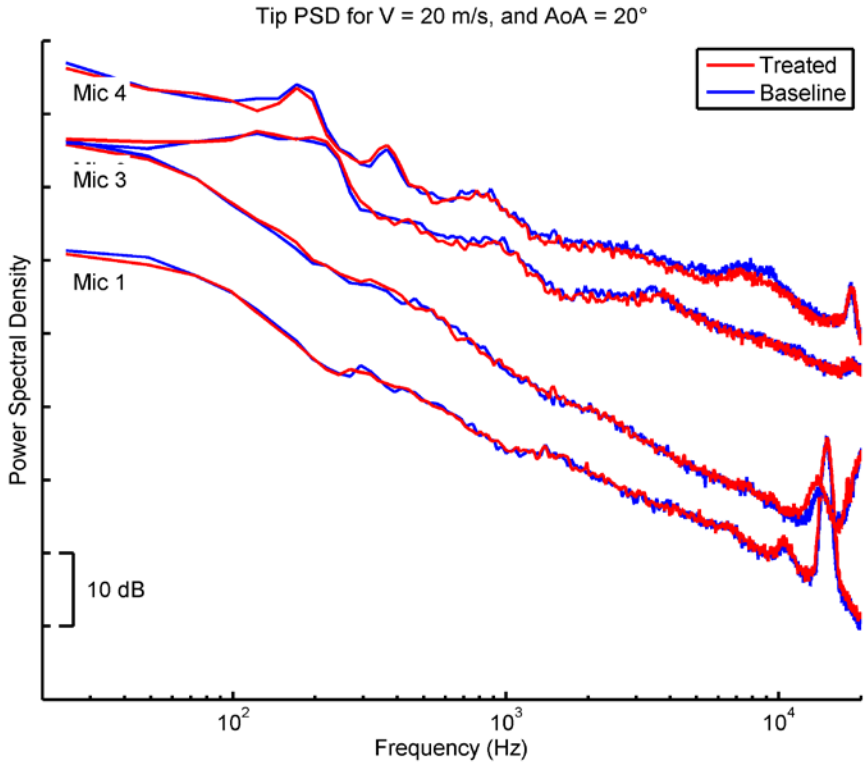
Tip PSD for V = 20 m/s, and AoA = 20°
Treated
Baseline
Mic 4
Mic 3
Mic 1
Power Spectral Density
10 dB
10^2
10^3
10^4
Frequency (Hz)

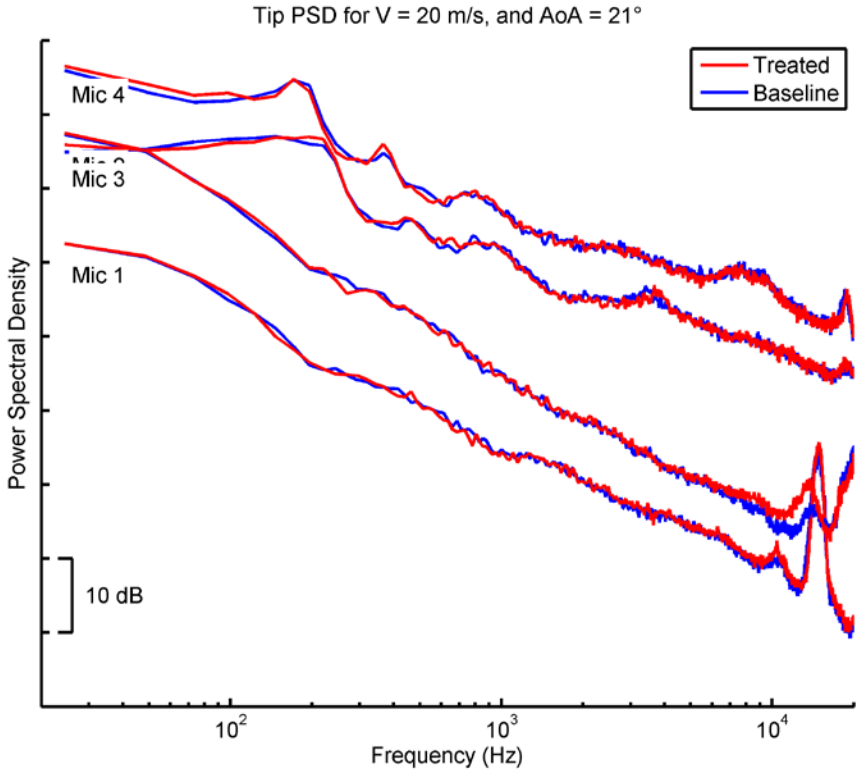
Tip PSD for V = 20 m/s, and AoA = 21°
Treated
Baseline
Mic 4
Mic 3
Mic 1
Power Spectral Density
10 dB
10^2
10^3
10^4
Frequency (Hz)

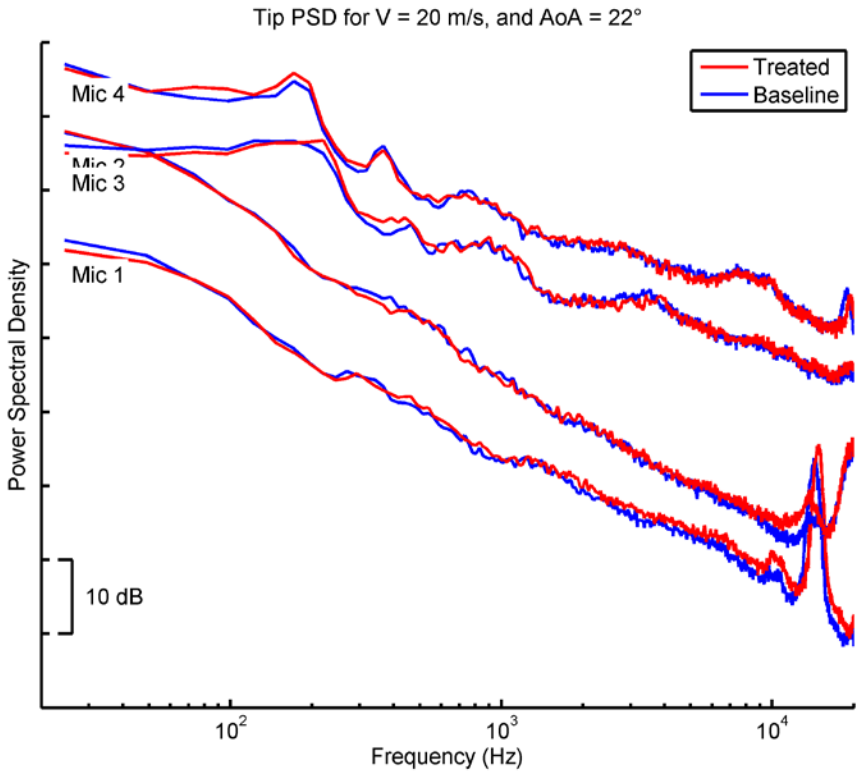
Tip PSD for V = 20 m/s, and AoA = 22°
Treated
Baseline
Mic 4
Mic 3
Mic 1
10 dB
Power Spectral Density
10^2
10^3
10^4
Frequency (Hz)

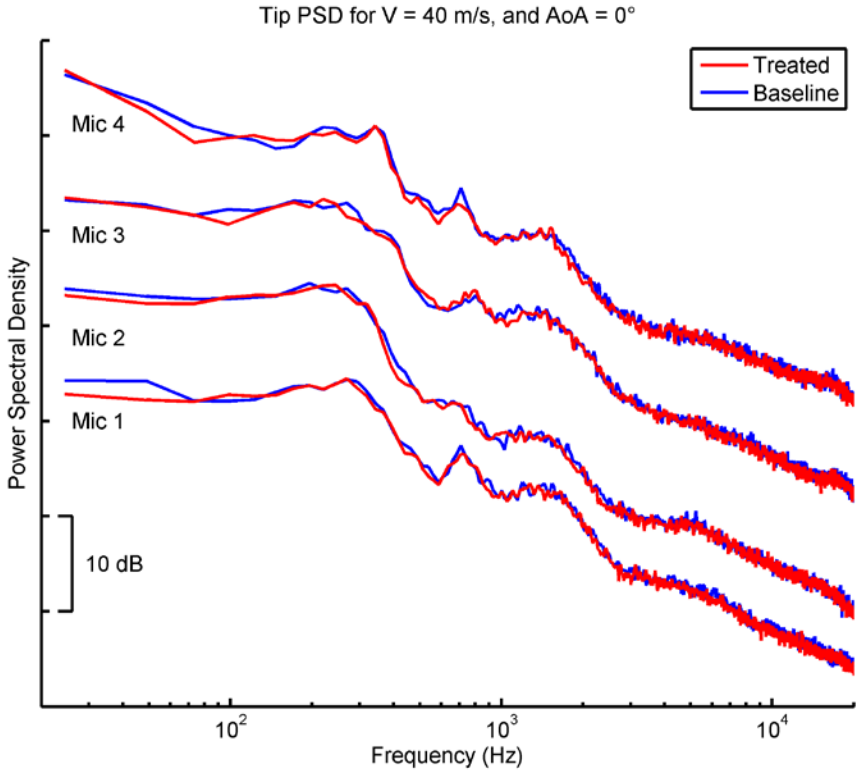
Tip PSD for V = 40 m/s, and AoA = 0°
Treated
Baseline
Mic 4
Mic 3
Mic 2
Mic 1
10 dB
Power Spectral Density
10^2
10^3
10^4
Frequency (Hz)

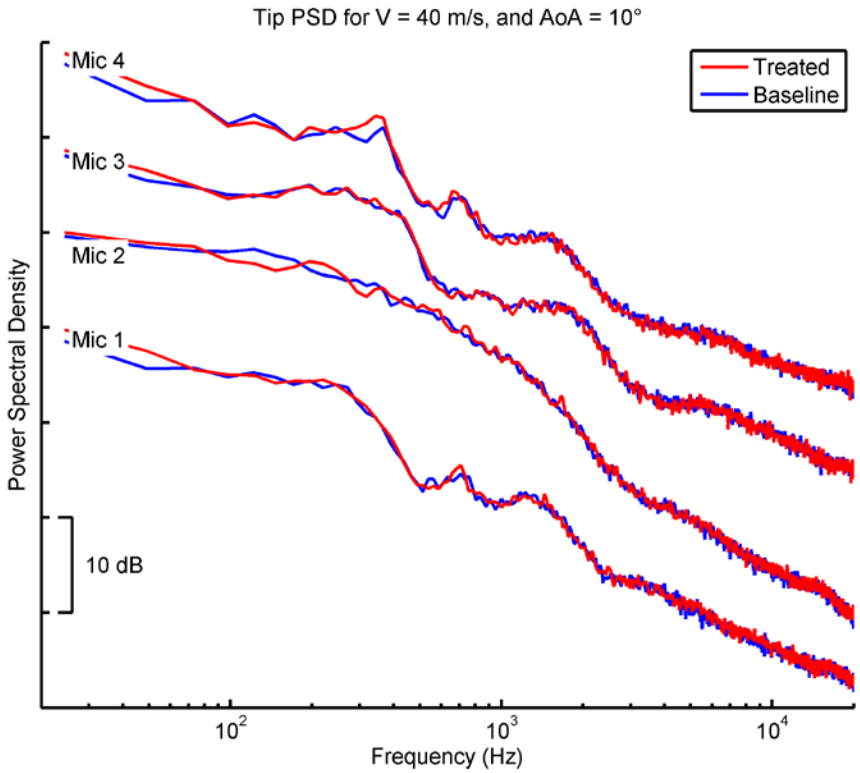
Tip PSD for V = 40 m/s, and AoA = 10°
Treated
Baseline
Mic 4
Mic 3
Mic 2
Mic 1
10 dB
Power Spectral Density
10^2
10^3
10^4
Frequency (Hz)

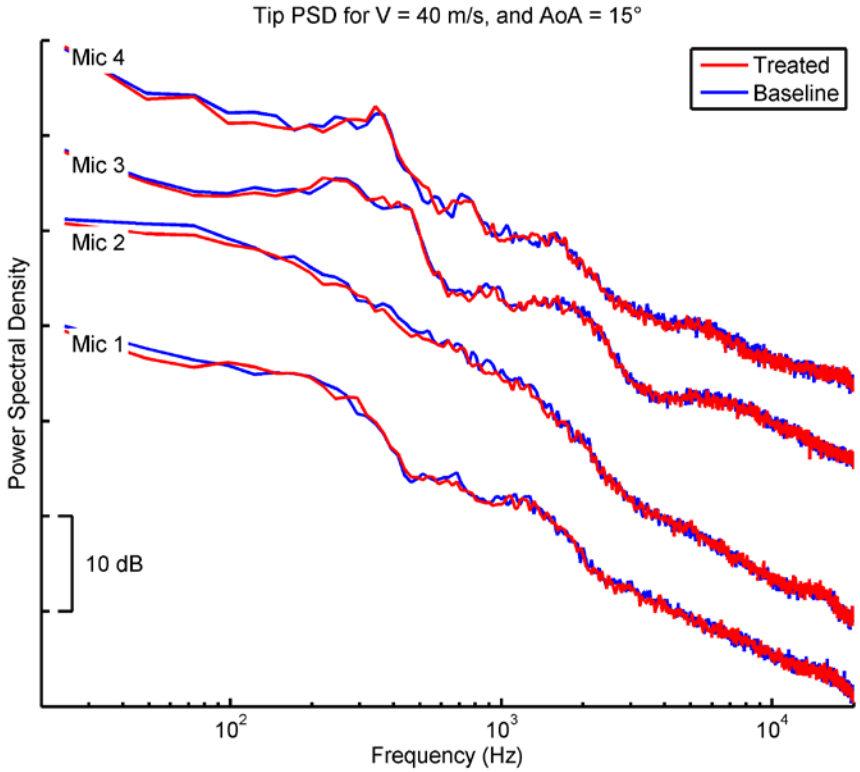
Tip PSD for V = 40 m/s, and AoA = 15°
Treated
Baseline
Mic 4
Mic 3
Mic 2
Mic 1
10 dB
Power Spectral Density
10^2
10^3
10^4
Frequency (Hz)

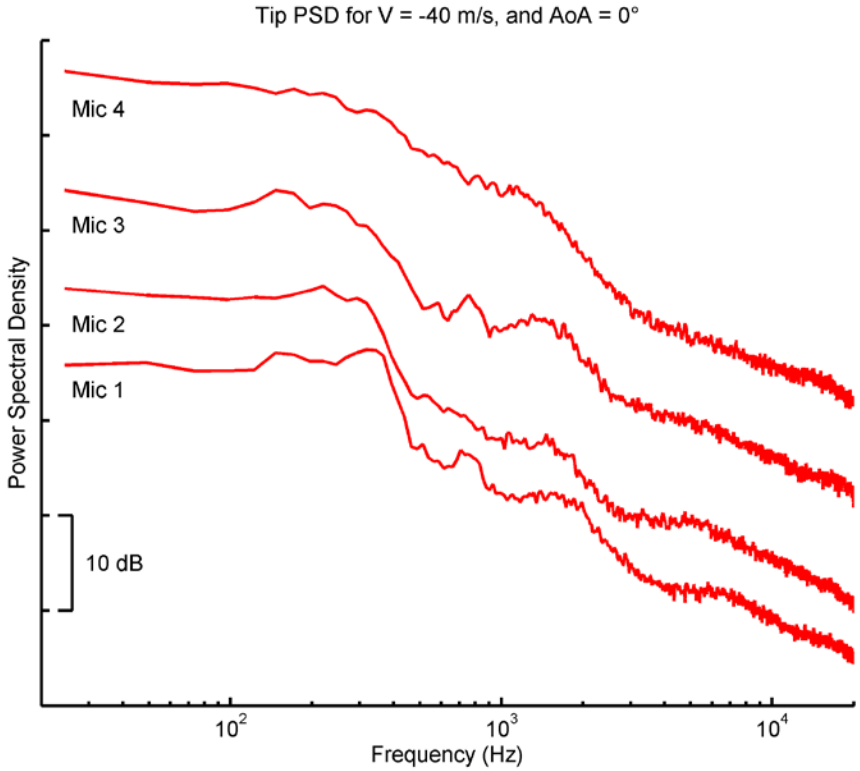
Tip PSD for V = -40 m/s, and AoA = 0°
Mic 4
Mic 3
Mic 2
Mic 1
10 dB
Power Spectral Density
10^2
10^3
10^4
Frequency (Hz)

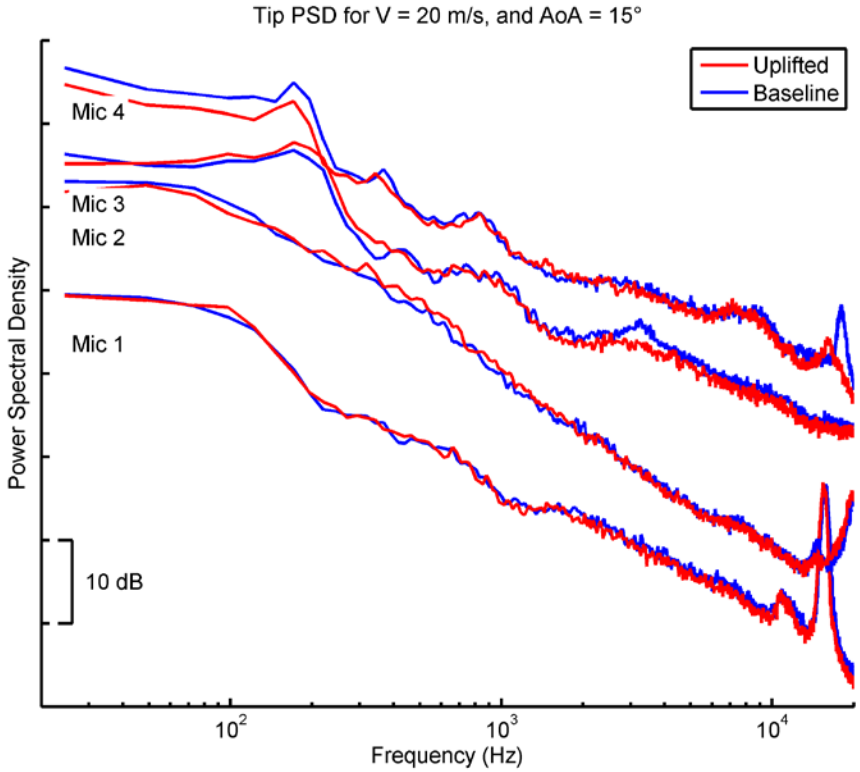
Tip PSD for V = 20 m/s, and AoA = 15°
Uplifted
Baseline
Mic 4
Mic 3
Mic 2
Mic 1
10 dB
Power Spectral Density
10^2
10^3
10^4
Frequency (Hz)

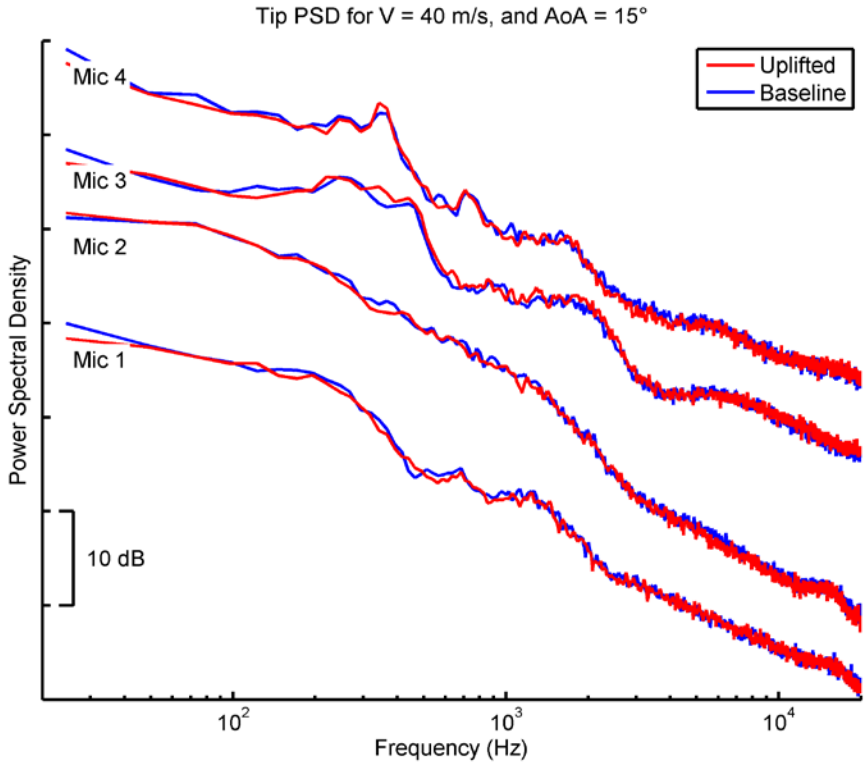
Tip PSD for V = 40 m/s, and AoA = 15°
Uplifted
Baseline
Mic 4
Mic 3
Mic 2
Mic 1
10 dB
Power Spectral Density
10^2
10^3
10^4
Frequency (Hz)

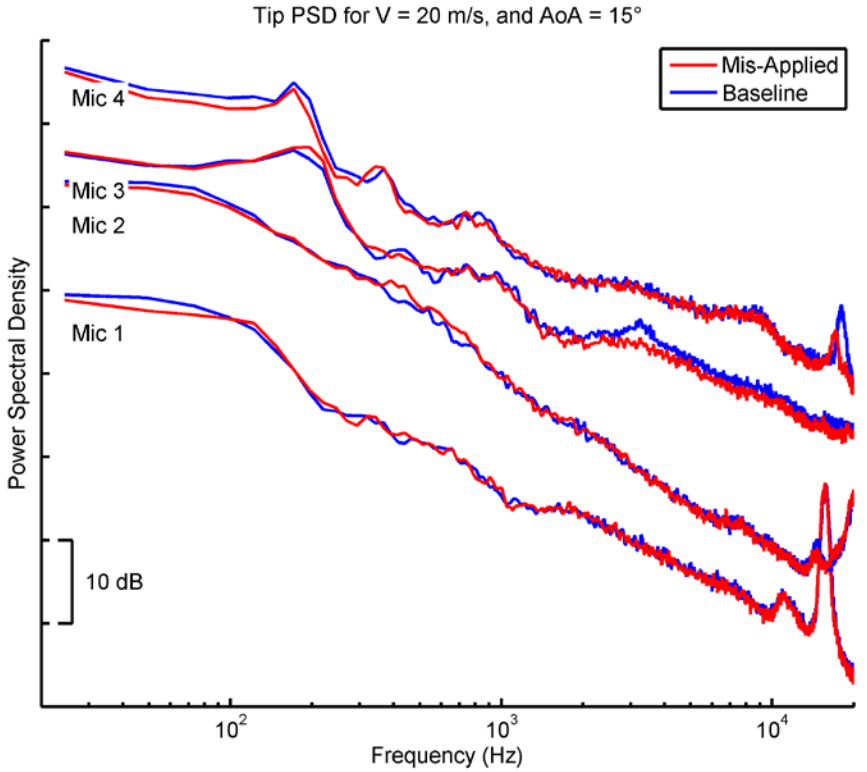
Tip PSD for V = 20 m/s, and AoA = 15°
Mis-Applied
Baseline
Mic 4
Mic 3
Mic 2
Mic 1
10 dB
Power Spectral Density
10^2
10^3
10^4
Frequency (Hz)

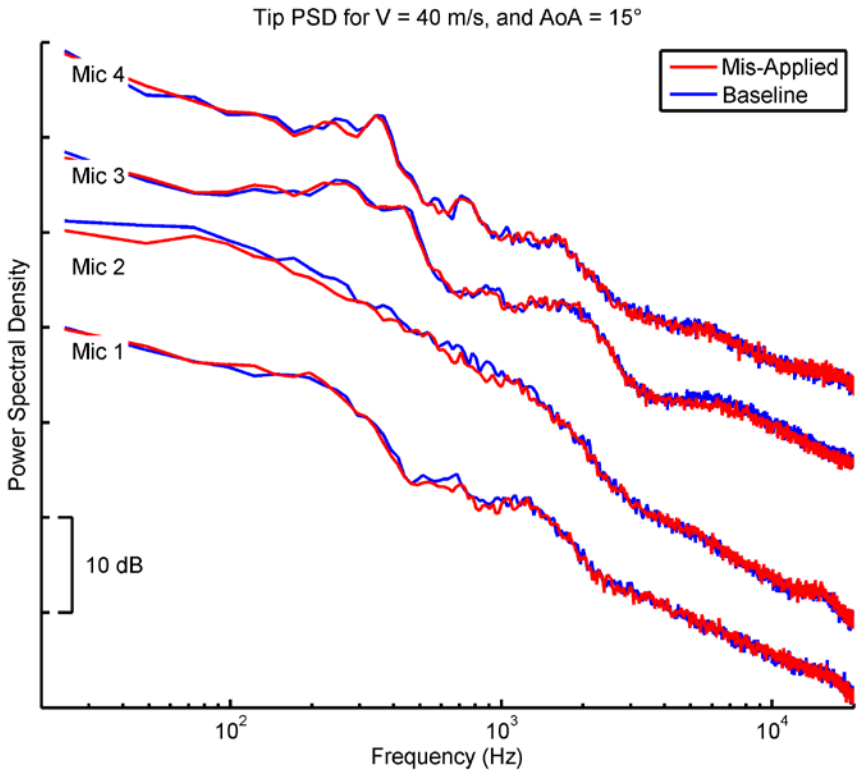
Tip PSD for V = 40 m/s, and AoA = 15°
Mis-Applied
Baseline
Mic 4
Mic 3
Mic 2
Mic 1
10 dB
Power Spectral Density
10^2
10^3
10^4
Frequency (Hz)

Appendix B: Additional Tables

S809 Baseline Load Cell Results

Run	AoA	C_L	C_D	C_M
1	0°	0.101	0.019	-0.034
2	0°	0.103	0.019	-0.034
3	0°	0.105	0.019	-0.034
4	0°	0.102	0.019	-0.034
5	12°	1.205	0.093	-0.068
6	12°	1.205	0.091	-0.068
7	12°	1.204	0.091	-0.068
8	12°	1.205	0.089	-0.068
9	15°	1.264	0.051	-0.080
10	15°	1.260	0.050	-0.079
11	15°	1.265	0.045	-0.079
12	15°	1.256	0.046	0.078
13	25°	1.005	0.289	-0.187
14	25°	1.012	0.291	-0.186
15	25°	1.002	0.294	-0.188
16	25°	1.003	0.292	0.185

Turbine Tip (20 m/s) Baseline				
Run	AoA	CL*S	CD*S	CM*S*c
1	0	0.041	0.013	-0.027
2	0	0.041	0.012	-0.027
3	0	0.040	0.013	-0.027
4	0	0.039	0.013	-0.027
5	10	0.391	0.045	-0.041
6	10	0.390	0.046	-0.041
7	10	0.389	0.046	-0.041
8	10	0.388	0.046	-0.041
9	15	0.556	0.085	-0.054
10	15	0.554	0.085	-0.053
11	15	0.553	0.085	-0.053
12	15	0.568	0.078	-0.047
13	19	0.695	0.121	-0.060
14	19	0.698	0.122	-0.059
15	19	0.698	0.122	-0.059
16	19	0.698	0.121	-0.059
17	20	0.730	0.135	-0.064
18	20	0.732	0.136	-0.064
19	20	0.732	0.136	-0.064
20	20	0.732	0.136	-0.064
21	21	0.756	0.148	-0.069
22	21	0.760	0.149	-0.068
23	21	0.760	0.149	-0.068
24	21	0.759	0.149	-0.068
25	22	0.781	0.160	-0.073
26	22	0.785	0.162	-0.073
27	22	0.785	0.162	-0.073
28	22	0.784	0.162	-0.073

Turbine Tip (40 m/s) Baseline				
Run	AoA	CL*S	CD*S	CM*S*c
1	0	0.03	0.01	-0.03
2	0	0.03	0.01	-0.03
3	0	0.03	0.01	-0.03
4	0	0.03	0.01	-0.03
5	10	0.37	0.06	-0.04
6	10	0.37	0.06	-0.04
7	10	0.37	0.06	-0.04
8	10	0.37	0.06	-0.04
9	15	0.52	0.12	-0.05
10	15	0.52	0.12	-0.05
11	15	0.53	0.11	-0.04
12	15	0.53	0.11	-0.04

S809 Treated Results

Run	AoA	C_L	C_D	C_M
1	0°	0.068	0.023	-0.028
2	0°	0.067	0.023	-0.028
3	0°	0.067	0.023	-0.027
4	0°	0.067	0.023	-0.027
5	12°	1.153	0.077	-0.068
6	12°	1.153	0.073	-0.068
7	12°	1.152	0.068	-0.067
8	12°	1.151	0.066	-0.067
9	15°	1.247	0.150	-0.080
10	15°	1.248	0.149	-0.080
11	15°	1.247	0.149	-0.080
12	15°	1.247	0.149	-0.080
13	25°	1.103	0.429	-0.190
14	25°	1.084	0.415	-0.177
15	25°	1.092	0.424	-0.190
16	25°	1.092	0.419	-0.190

Turbine Tip (20 m/s) Treated				
Run	AoA	CL	CD	CM
1	0	0.04	0.02	-0.02
2	0	0.04	0.02	-0.02
3	0	0.03	0.02	-0.02
4	0	0.03	0.02	-0.02
5	10	0.37	0.05	-0.04
6	10	0.37	0.05	-0.04
7	10	0.37	0.05	-0.04
8	10	0.36	0.05	-0.04
9	15	0.55	0.08	-0.05
10	15	0.55	0.08	-0.05
11	15	0.55	0.08	-0.05
12	15	0.55	0.09	-0.05
13	19	0.69	0.13	-0.06
14	19	0.69	0.13	-0.06
15	19	0.69	0.13	-0.06
16	19	0.69	0.13	-0.06
17	20	0.73	0.14	-0.07
18	20	0.73	0.14	-0.07
19	20	0.73	0.14	-0.07
20	20	0.73	0.14	-0.07
21	21	0.75	0.15	-0.07
22	21	0.75	0.15	-0.07
23	21	0.76	0.15	-0.07
24	21	0.76	0.15	-0.07
25	22	0.78	0.16	-0.07
26	22	0.78	0.16	-0.07
27	22	0.78	0.16	-0.07
28	22	0.78	0.16	-0.07

Turbine Tip (40 m/s) Treated				
Run	AoA	CL	CD	CM
1	0	0.03	0.02	-0.02
2	0	0.03	0.02	-0.02
3	0	0.03	0.02	-0.02
4	0	0.03	0.02	-0.02
5	10	0.35	0.06	-0.04
6	10	0.35	0.06	-0.04
7	10	0.35	0.06	-0.04
8	10	0.35	0.06	-0.04
9	15	0.51	0.12	-0.05
10	15	0.52	0.12	-0.05
11	15	0.51	0.12	-0.05
12	15	0.51	0.12	-0.05

Appendix C: Load Cell Data

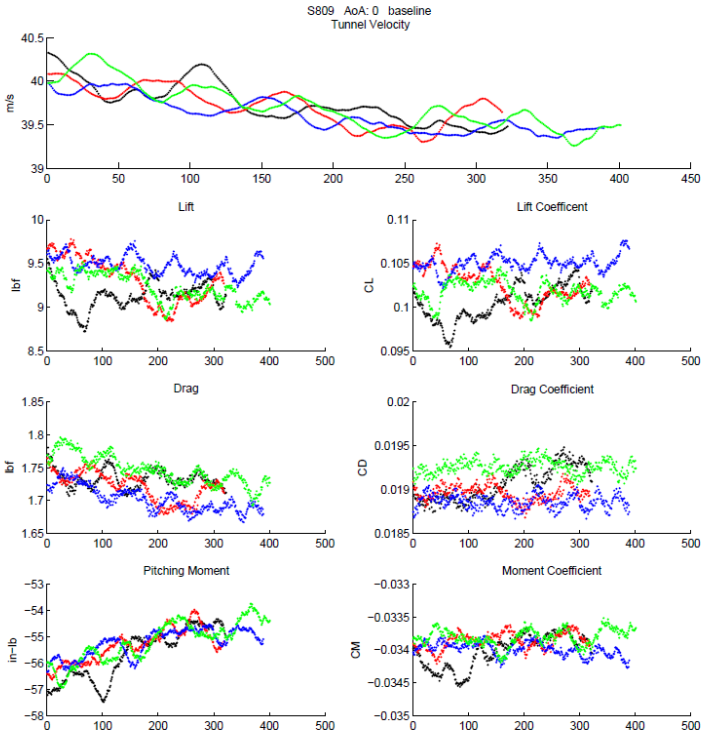
S809 AoA: 0 baseline
Tunnel Velocity
m/s
Lift
lbf
Lift Coefficent
CL
Drag
lbf
Drag Coefficient
CD
Pitching Moment
in-lb
Moment Coefficient
CM

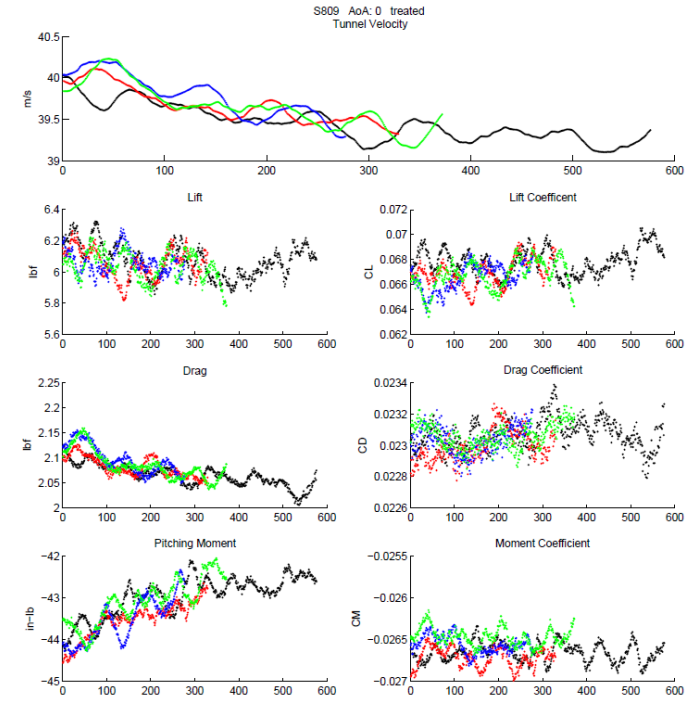
S809 AoA: 0 treated
Tunnel Velocity
m/s
Lift
lbf
Lift Coefficent
CL
Drag
lbf
Drag Coefficient
CD
Pitching Moment
in-lb
Moment Coefficient
CM

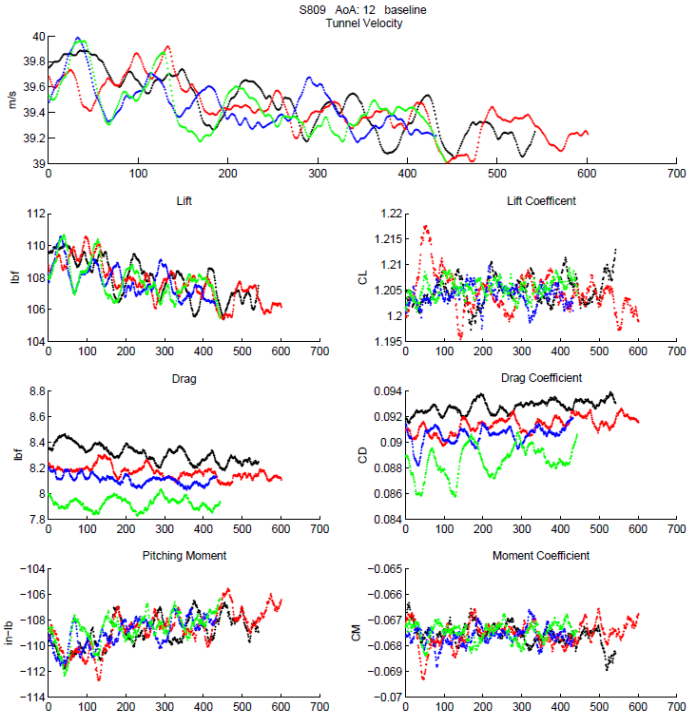
S809 AoA: 12 baseline
Tunnel Velocity
m/s
Lift
lbf
Lift Coefficent
CL
Drag
lbf
Drag Coefficient
CD
Pitching Moment
in−lb
Moment Coefficient
CM

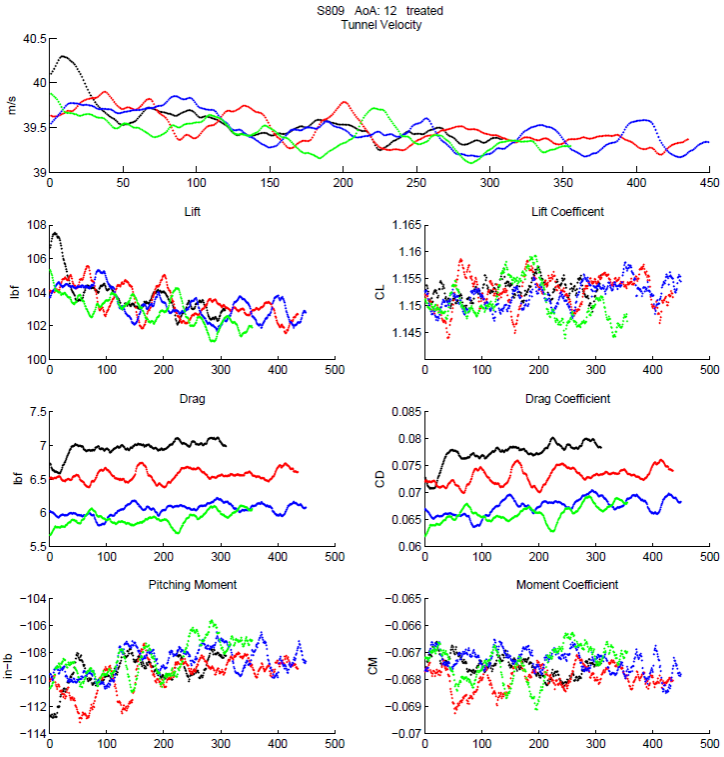
S809 AoA: 12 treated
Tunnel Velocity
m/s
Lift
lbf
Lift Coefficent
CL
Drag
lbf
Drag Coefficient
CD
Pitching Moment
in−lb
Moment Coefficient
CM

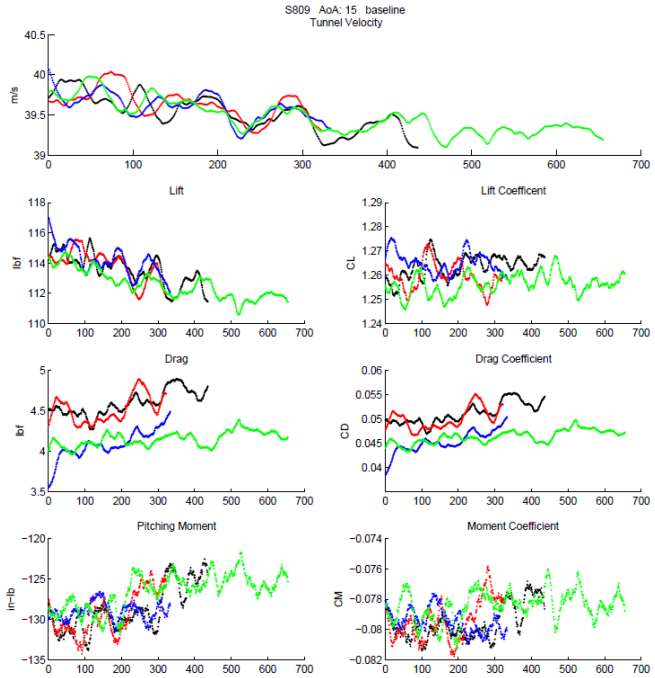
S809 AoA: 15 baseline
Tunnel Velocity
m/s
Lift
lbf
Lift Coefficent
CL
Drag
lbf
Drag Coefficient
CD
Pitching Moment
in−lb
Moment Coefficient
CM

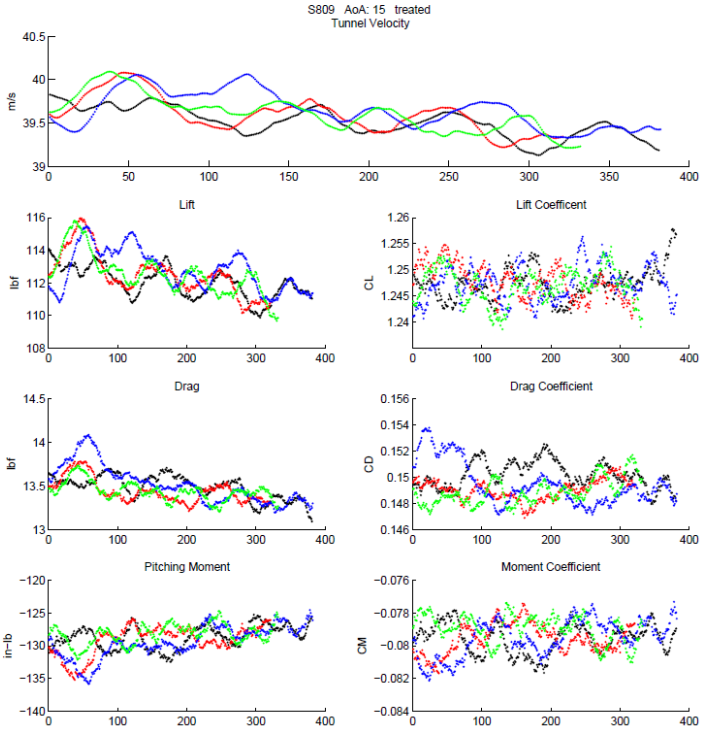
S809 AoA: 15 treated
Tunnel Velocity
m/s
Lift
lbf
Lift Coefficent
CL
Drag
lbf
Drag Coefficient
CD
Pitching Moment
in−lb
Moment Coefficient
CM

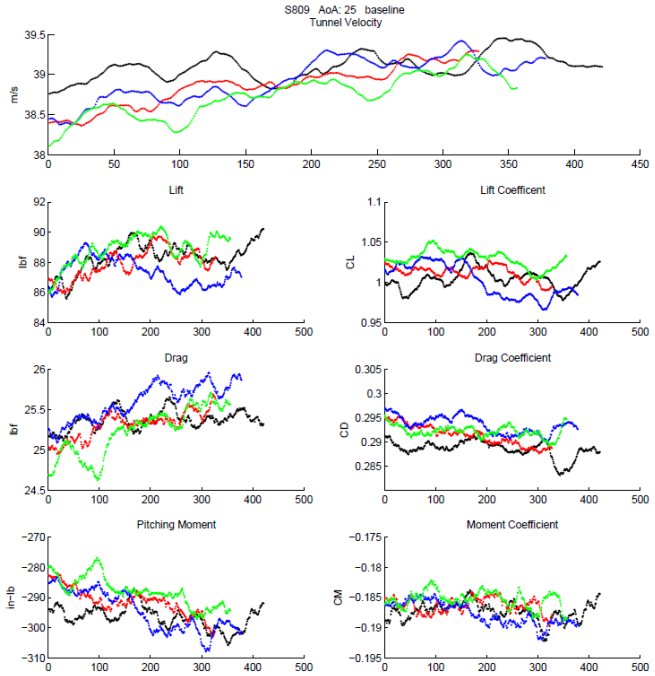
S809 AoA: 25 baseline
Tunnel Velocity
m/s
Lift
lbf
Lift Coefficent
CL
Drag
lbf
Drag Coefficient
CD
Pitching Moment
in-lb
Moment Coefficient
CM

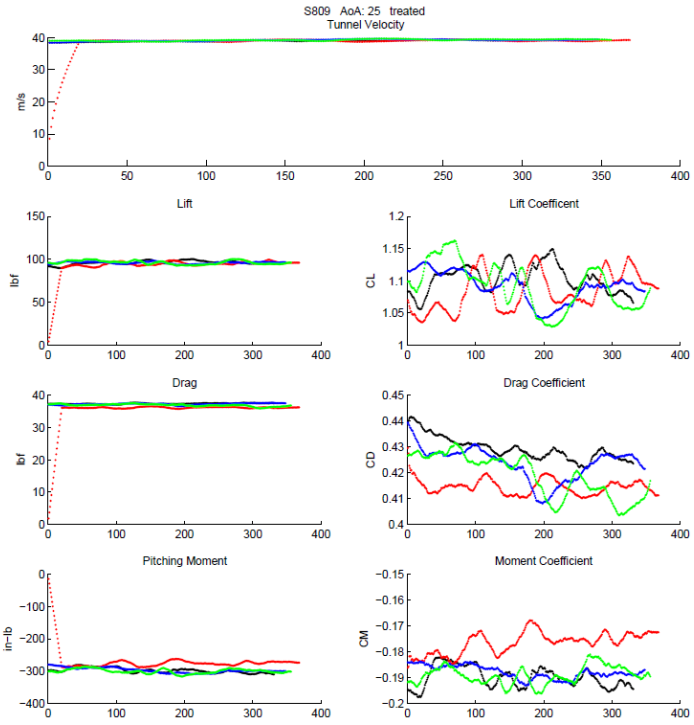
S809 AoA: 25 treated
Tunnel Velocity
m/s
Lift
lbf
Lift Coefficent
CL
Drag
lbf
Drag Coefficient
CD
Pitching Moment
in-lb
Moment Coefficient
CM

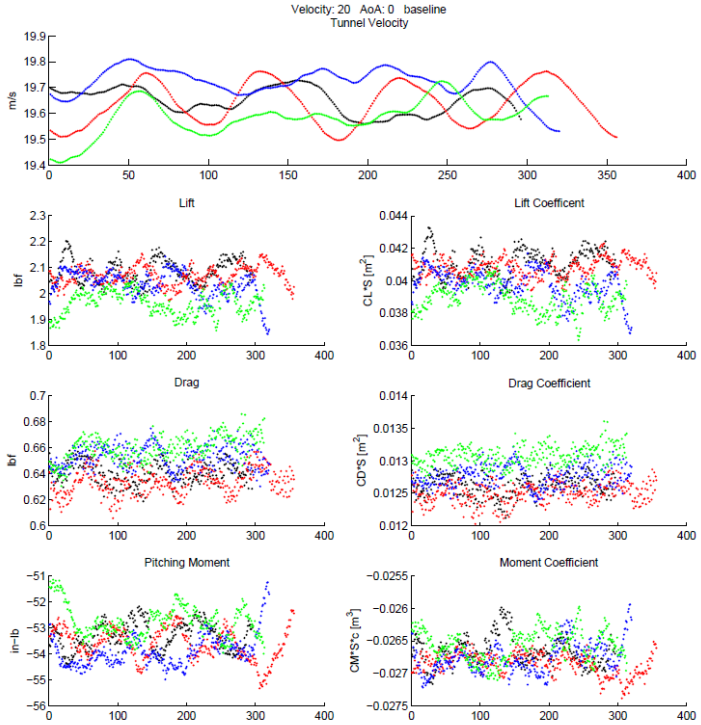
Velocity: 20 AoA: 0 baseline
Tunnel Velocity
m/s
Lift
lbf
Lift Coefficent
CL*S [m^2]
Drag
lbf
Drag Coefficient
CD*S [m^2]
Pitching Moment
in-lb
Moment Coefficient
CM*S*c [m^3]

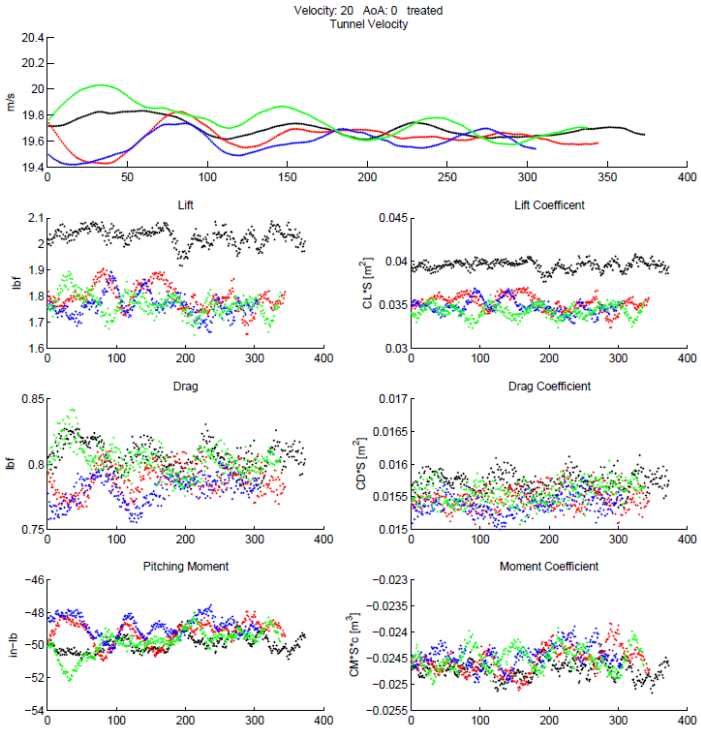
Velocity: 20 AoA: 0 treated
Tunnel Velocity
m/s
Lift
lbf
Lift Coefficent
CL*S [m^2]
Drag
lbf
Drag Coefficient
CD*S [m^2]
Pitching Moment
in-lb
Moment Coefficient
CM*S*c [m^3]

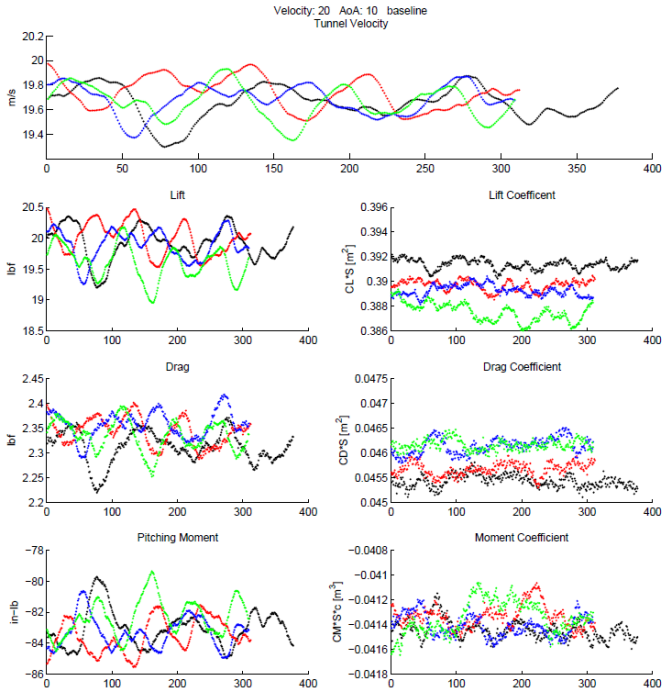
Velocity: 20 AoA: 10 baseline
Tunnel Velocity
m/s
Lift
lbf
Lift Coefficent
CL*S [m^2]
Drag
lbf
Drag Coefficient
CD*S [m^2]
Pitching Moment
in-lb
Moment Coefficient
CM*S*c [m^3]

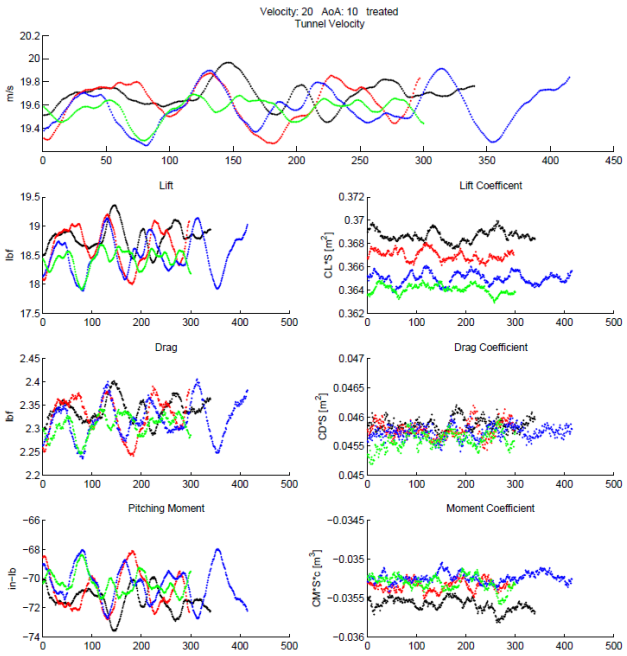
Velocity: 20 AoA: 10 treated
Tunnel Velocity
m/s
Lift
lbf
Lift Coefficent
CL*S [m^2]
Drag
lbf
Drag Coefficient
CD*S [m^2]
Pitching Moment
in-lb
Moment Coefficient
CM*S*c [m^3]

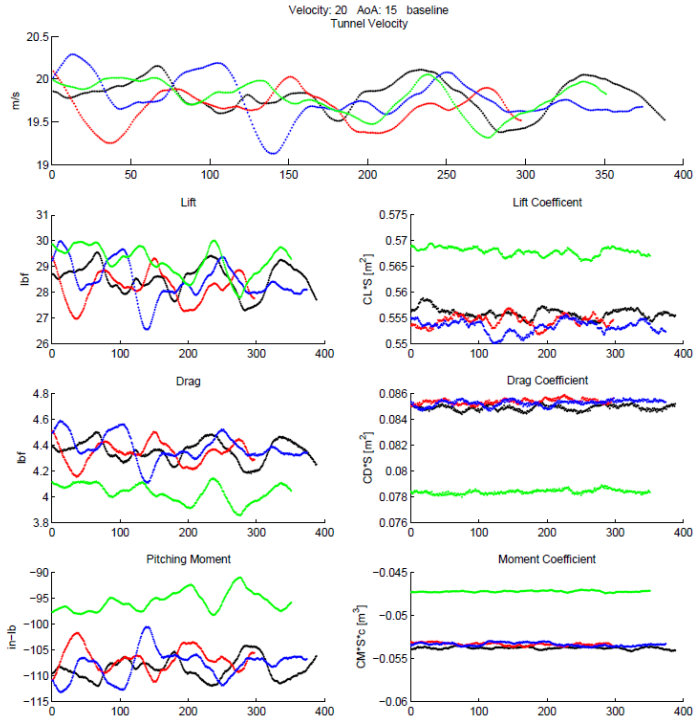
Velocity: 20 AoA: 15 baseline
Tunnel Velocity
m/s
Lift
lbf
Lift Coefficent
CL*S [m^2]
Drag
lbf
Drag Coefficient
CD*S [m^2]
Pitching Moment
in-lb
Moment Coefficient
CM*S*c [m^3]

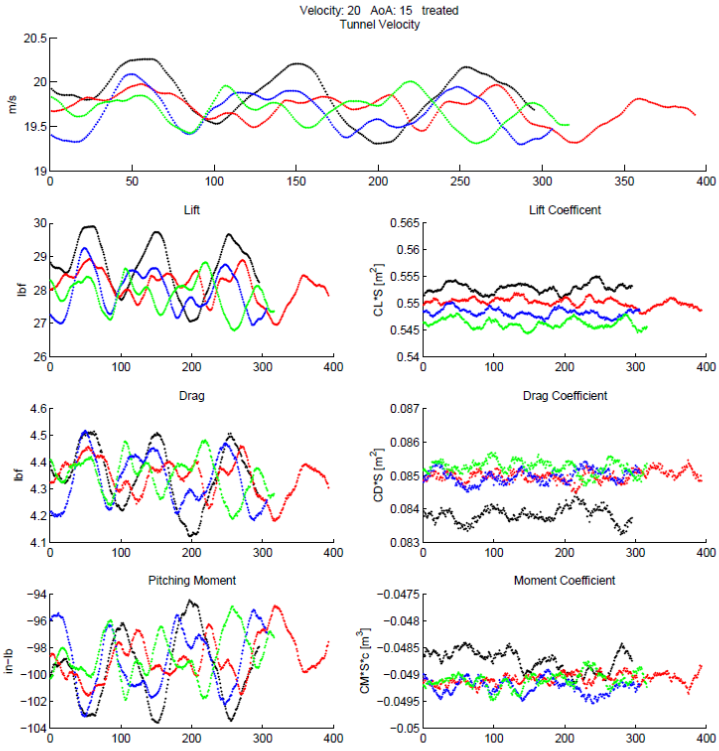
Velocity: 20 AoA: 15 treated
Tunnel Velocity
m/s
Lift
lbf
Lift Coefficent
CL*S [m^2]
Drag
lbf
Drag Coefficient
CD*S [m^2]
Pitching Moment
in-lb
Moment Coefficient
CM*S*c [m^3]

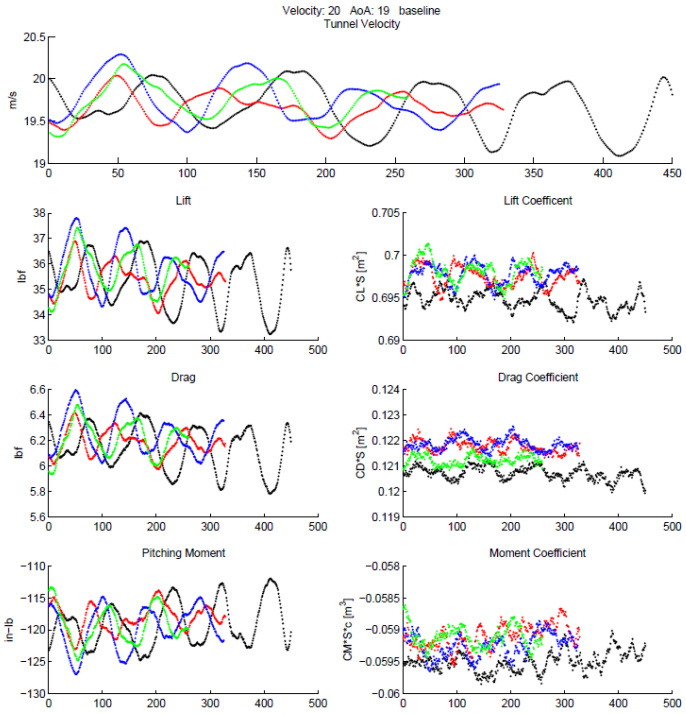
Velocity: 20 AoA: 19 baseline
Tunnel Velocity
m/s
Lift
lbf
Lift Coefficent
CL*S [m²]
Drag
lbf
Drag Coefficient
CD*S [m²]
Pitching Moment
in−lb
Moment Coefficient
CM*S*c [m³]

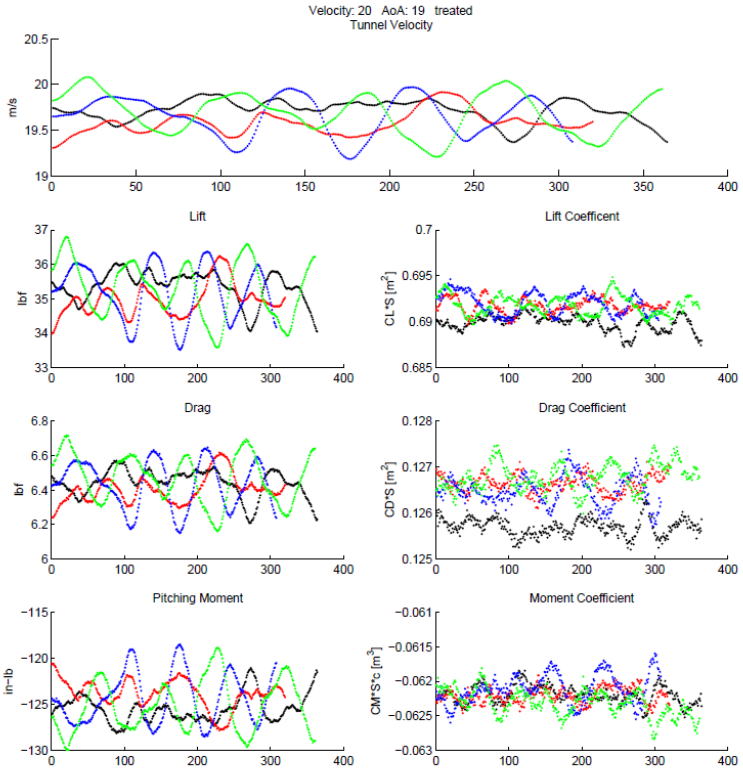
Velocity: 20 AoA: 19 treated
Tunnel Velocity
m/s
Lift
lbf
Lift Coefficent
CL*S [m²]
Drag
lbf
Drag Coefficient
CD*S [m²]
Pitching Moment
in−lb
Moment Coefficient
CM*S*c [m³]

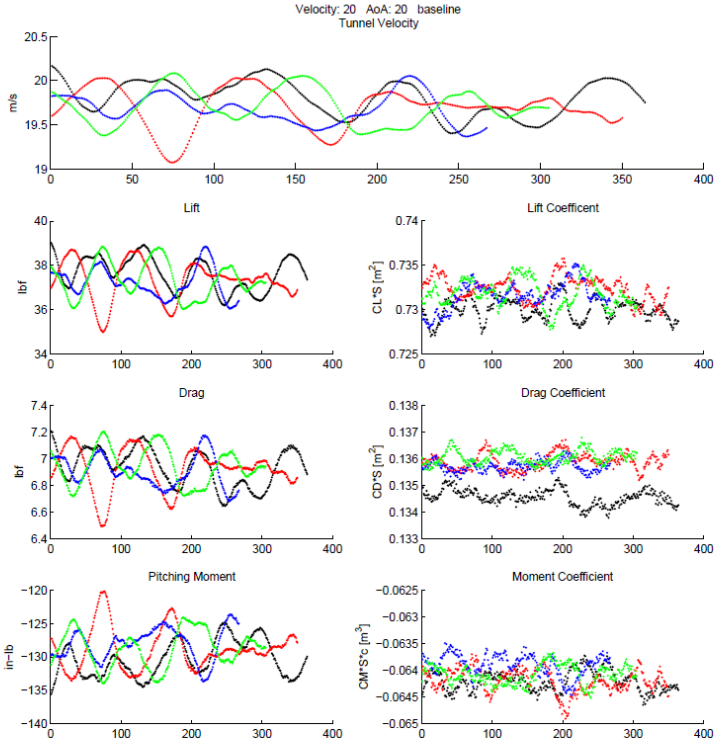
Velocity: 20 AoA: 20 baseline
Tunnel Velocity
m/s
Lift
lbf
Lift Coefficent
CL*S [m²]
Drag
lbf
Drag Coefficient
CD*S [m²]
Pitching Moment
in−lb
Moment Coefficient
CM*S*c [m³]

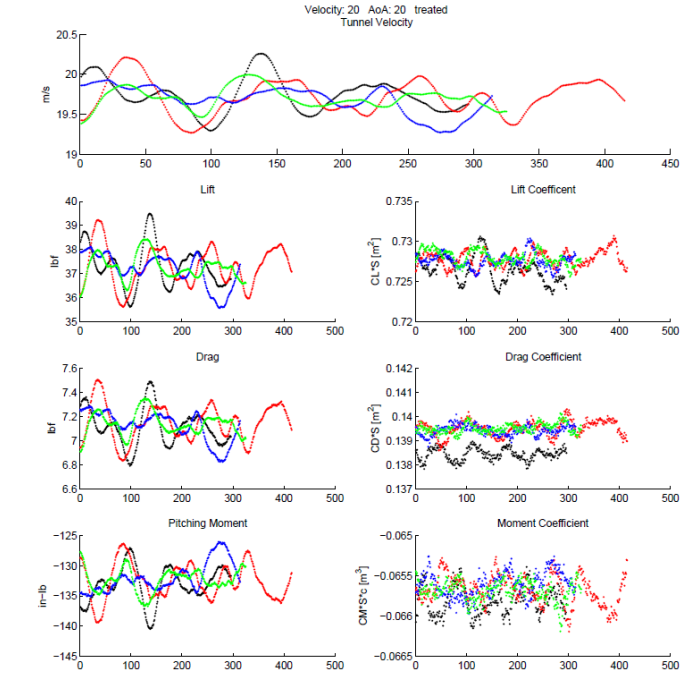
Velocity: 20 AoA: 20 treated
Tunnel Velocity
m/s
Lift
lbf
Lift Coefficent
CL*S [m²]
Drag
lbf
Drag Coefficient
CD*S [m²]
Pitching Moment
in−lb
Moment Coefficient
CM*S*c [m³]

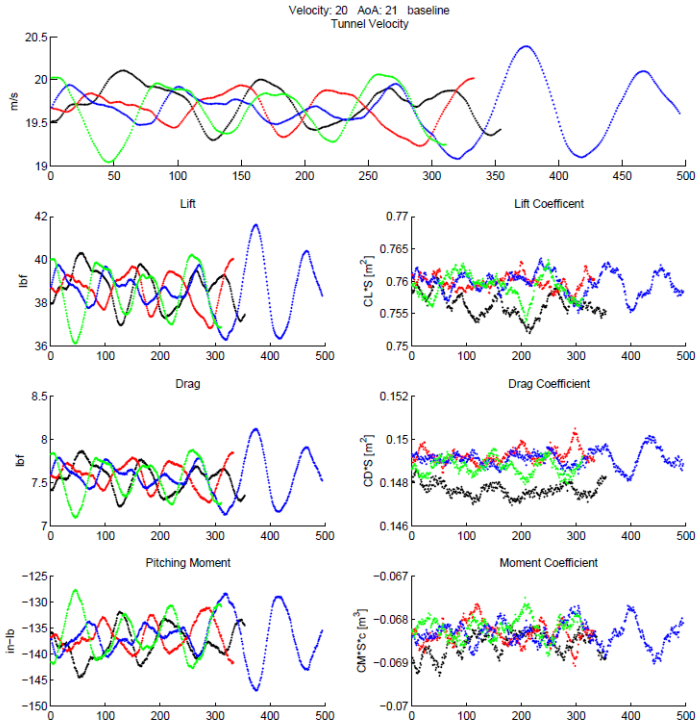
Velocity: 20 AoA: 21 baseline
Tunnel Velocity
m/s
Lift
lbf
Lift Coefficent
CL*S [m^2]
Drag
lbf
Drag Coefficient
CD*S [m^2]
Pitching Moment
in−lb
Moment Coefficient
CM*S*c [m^3]

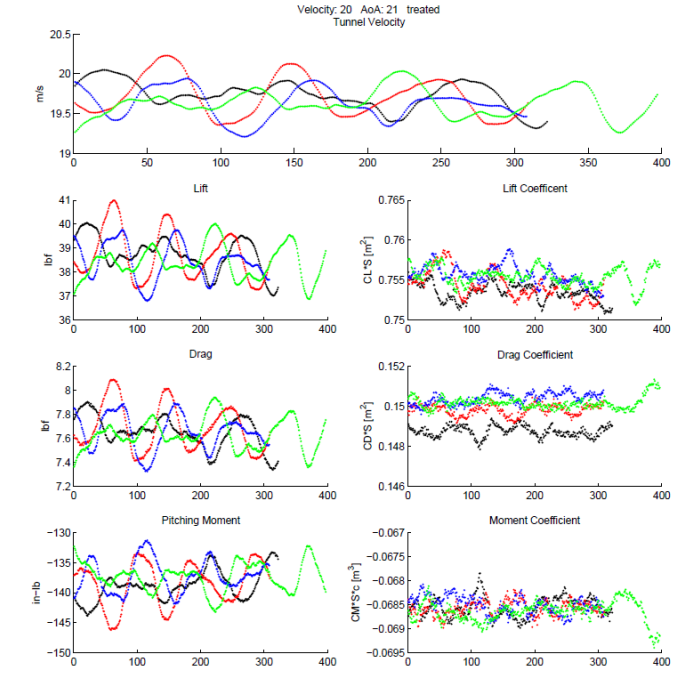
Velocity: 20 AoA: 21 treated
Tunnel Velocity
m/s
Lift
lbf
Lift Coefficent
CL*S [m^2]
Drag
lbf
Drag Coefficient
CD*S [m^2]
Pitching Moment
in−lb
Moment Coefficient
CM*S*c [m^3]

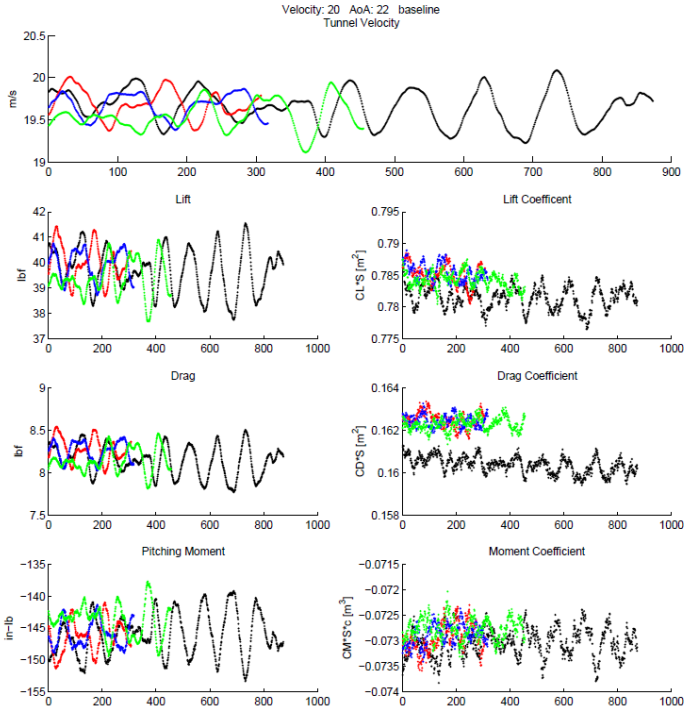
Velocity: 20 AoA: 22 baseline
Tunnel Velocity
m/s
Lift
lbf
Lift Coefficent
CL*S [m^2]
Drag
lbf
Drag Coefficient
CD*S [m^2]
Pitching Moment
in−lb
Moment Coefficient
CM*S*c [m^3]

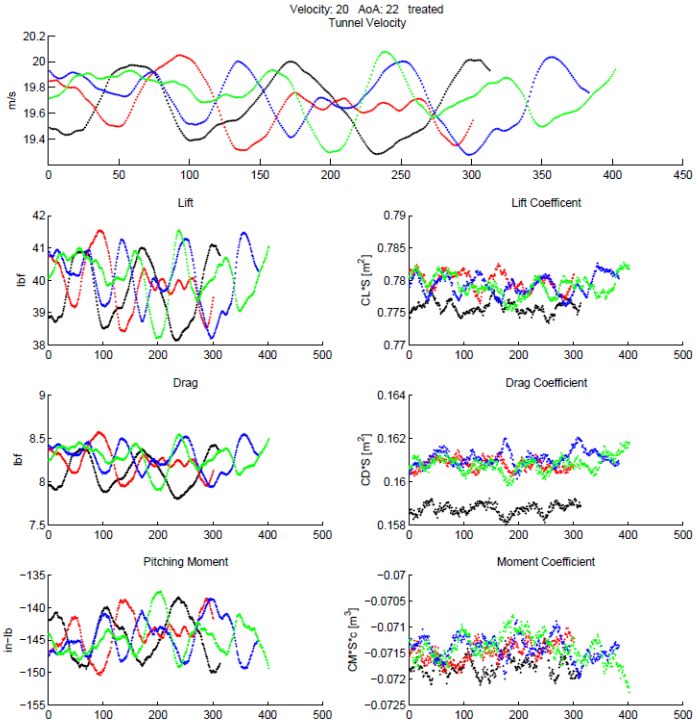
Velocity: 20 AoA: 22 treated
Tunnel Velocity
m/s
Lift
lbf
Lift Coefficent
CL*S [m^2]
Drag
lbf
Drag Coefficient
CD*S [m^2]
Pitching Moment
in−lb
Moment Coefficient
CM*S*c [m^3]

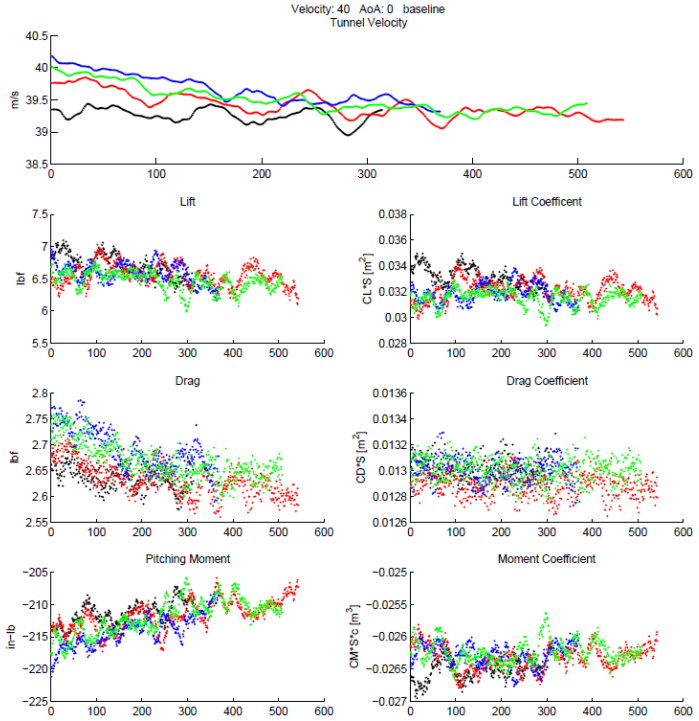
Velocity: 40 AoA: 0 baseline
Tunnel Velocity
m/s
Lift
lbf
Lift Coefficent
CL*S [m^2]
Drag
lbf
Drag Coefficient
CD*S [m^2]
Pitching Moment
in-lb
Moment Coefficient
CM*S*c [m^3]

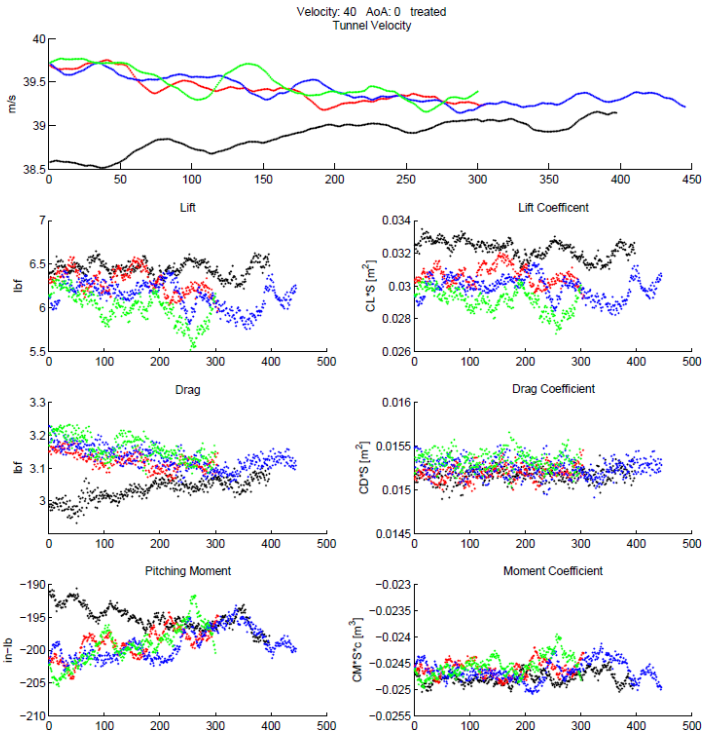
Velocity: 40 AoA: 0 treated
Tunnel Velocity
m/s
Lift
lbf
Lift Coefficent
CL*S [m^2]
Drag
lbf
Drag Coefficient
CD*S [m^2]
Pitching Moment
in-lb
Moment Coefficient
CM*S*c [m^3]

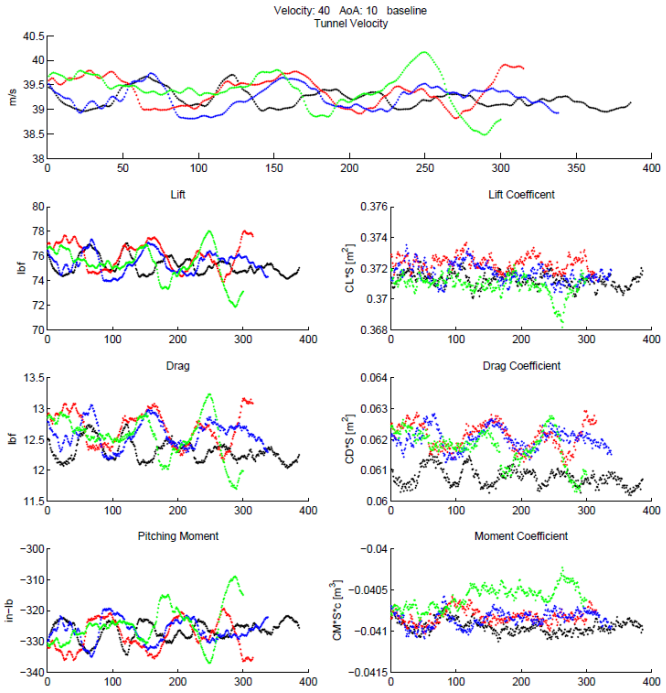
Velocity: 40 AoA: 10 baseline
Tunnel Velocity
m/s
Lift
lbf
Lift Coefficent
CL*S [m^2]
Drag
lbf
Drag Coefficient
CD*S [m^2]
Pitching Moment
in-lb
Moment Coefficient
CM*S*c [m^3]

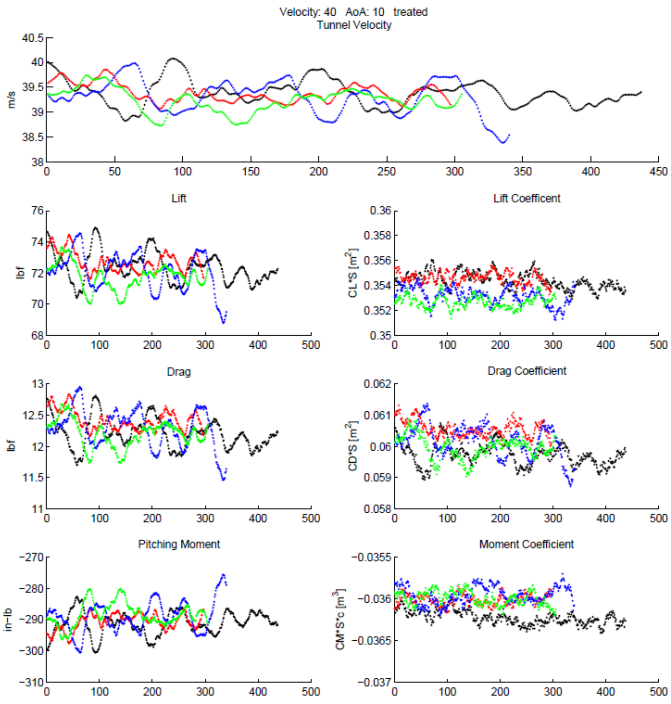
Velocity: 40 AoA: 10 treated
Tunnel Velocity
m/s
Lift
lbf
Lift Coefficent
CL*S [m^2]
Drag
lbf
Drag Coefficient
CD*S [m^2]
Pitching Moment
in-lb
Moment Coefficient
CM*S*c [m^3]

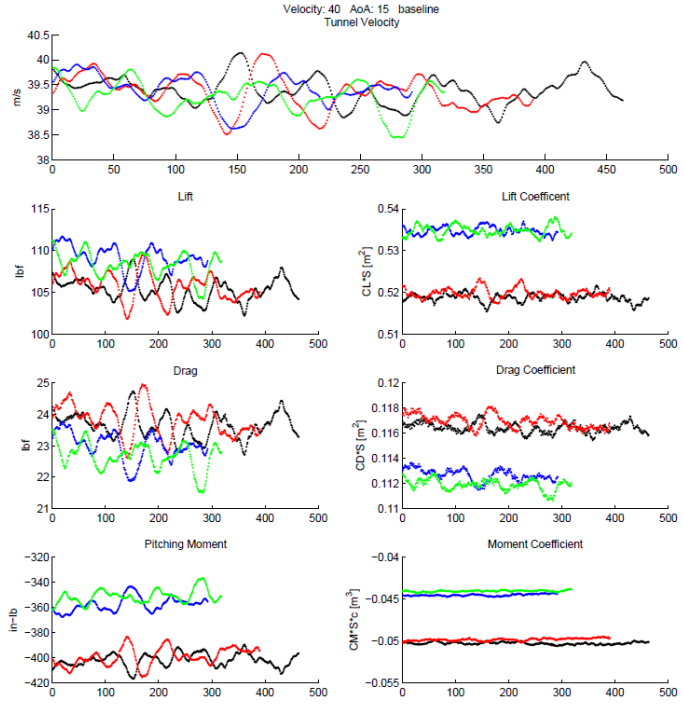
Velocity: 40 AoA: 15 baseline
Tunnel Velocity
m/s
Lift
lbf
Lift Coefficent
CL*S [m²]
Drag
lbf
Drag Coefficient
CD*S [m²]
Pitching Moment
in−lb
Moment Coefficient
CM*S*c [m³]

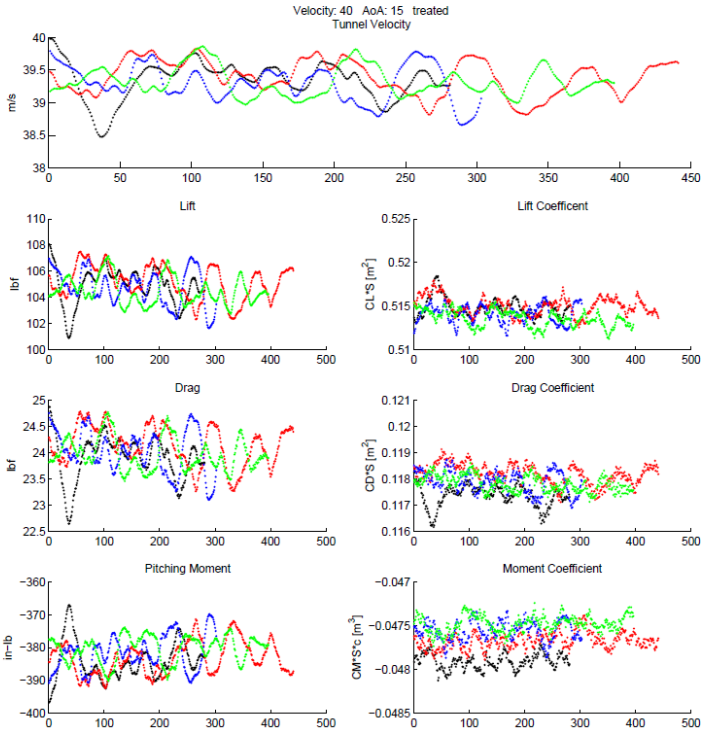
Velocity: 40 AoA: 15 treated
Tunnel Velocity
m/s
Lift
lbf
Lift Coefficent
CL*S [m²]
Drag
lbf
Drag Coefficient
CD*S [m²]
Pitching Moment
in−lb
Moment Coefficient
CM*S*c [m³]

Poor Treatment

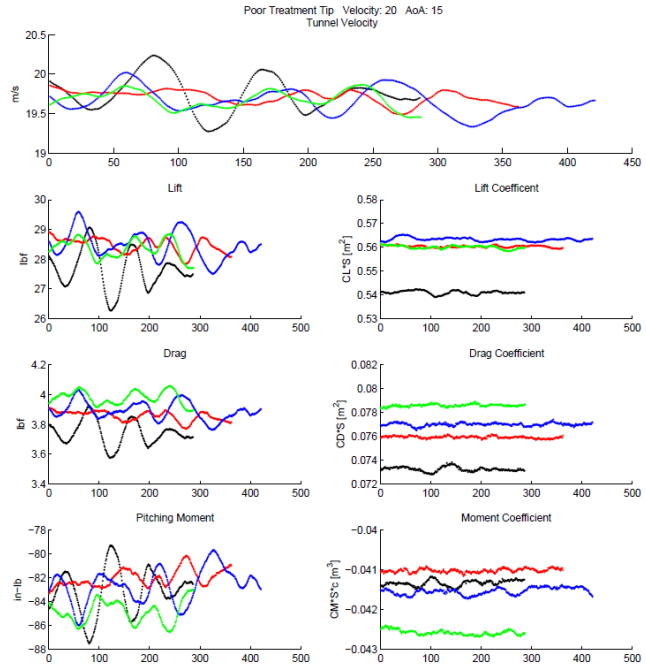

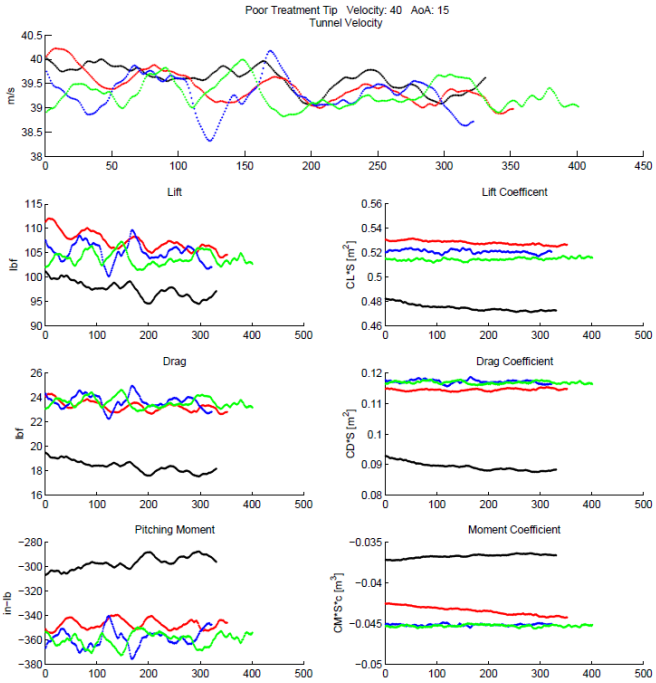

Backwards Treatment